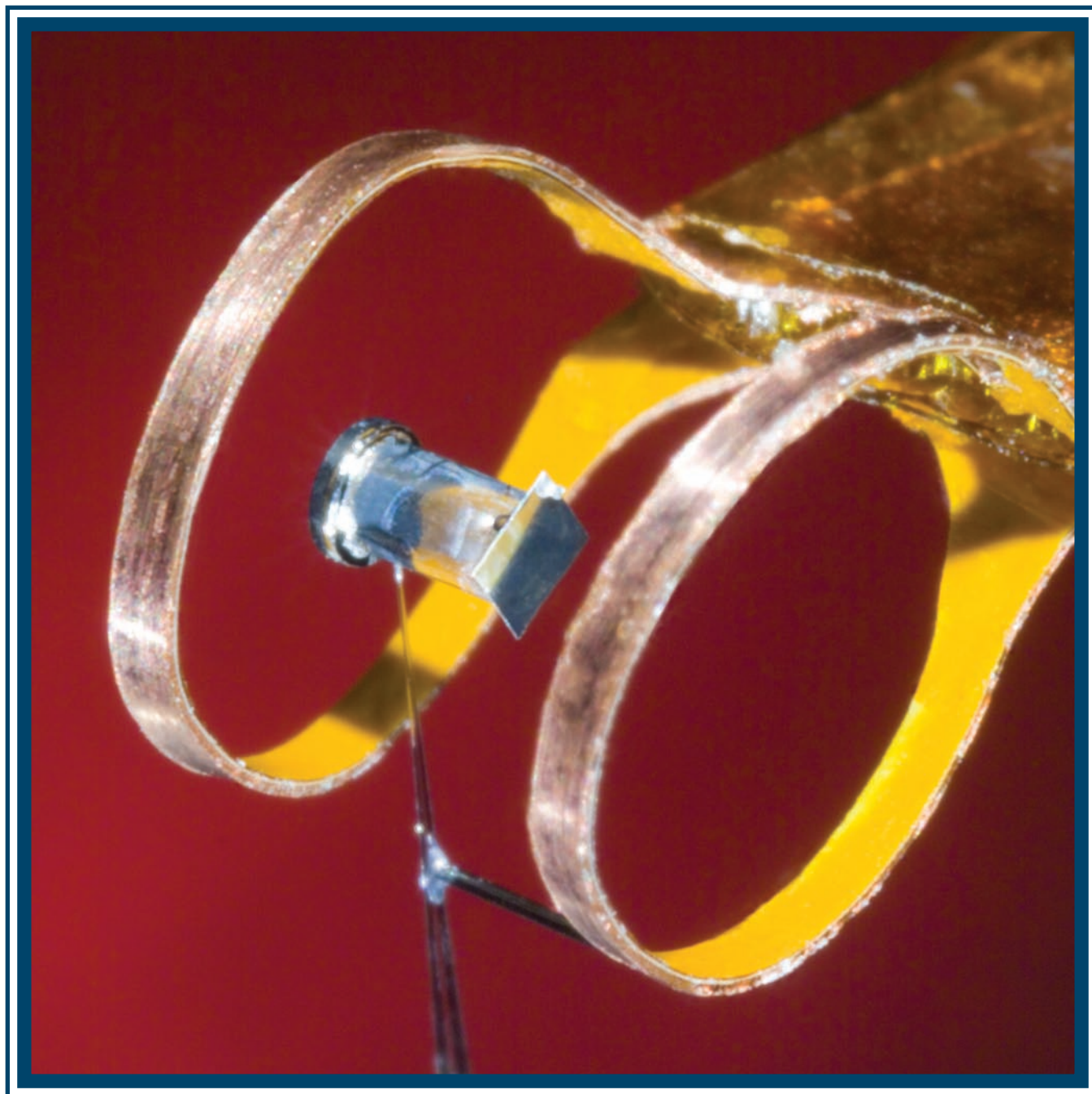


# LLE Review

## Quarterly Report



## About the Cover:

A Helmholtz-type, single-turn coil (shown on the cover) provides the seed field in which the laser target is immersed during laser-driven, magnetic-flux-compression experiments on OMEGA. In these experiments, 40 OMEGA beams compress an 860- $\mu\text{m}$ -diam, cylindrical CH shell (in the center of this photo) filled with  $\text{D}_2$  gas. It is expected that in the process, the seed magnetic field will be trapped and amplified by the highly conductive converging plasma. The dimensions of the coil are optimized for the beam irradiation geometry of the experiment. Magnetic-flux compression with lasers is expected to facilitate implosions where megagauss fields will—by inhibiting the electron thermal transport—reduce the thermal losses out of the hot spot. This can provide for implosions with higher gain (or lower-ignition-energy requirements) than what is possible with conventional ICF. The generation of super-strong magnetic fields can also be used in a variety of nonfusion experiments such as laboratory astrophysics, material science, etc.



The top photo on the left shows the magneto-inertial fusion energy delivery system (MIFEDS) that is being tested in the diagnostic TIM (ten-inch manipulator) facility. MIFEDS, a 10-T magnetic-pulse generator, is the main piece of enabling technology for laser-driven, magnetic-flux-compression experiments. Two members of the magneto-inertial fusion (MIF) team—postdoctoral researcher Orlin Gotchev (left) and graduate student Neo Jang (both with the Department of Mechanical Engineering and LLE)—are preparing the device (inset) for upcoming experiments on OMEGA. The other TIM facility members include Professor Riccardo Betti (MIF project leader) and Dr. James Knauer (LLE senior scientist).

This report was prepared as an account of work conducted by the Laboratory for Laser Energetics and sponsored by New York State Energy Research and Development Authority, the University of Rochester, the U.S. Department of Energy, and other agencies. Neither the above named sponsors, nor any of their employees, makes any warranty, expressed or implied, or assumes any legal liability or responsibility for the accuracy, completeness, or usefulness of any information, apparatus, product, or process disclosed, or represents that its use would not infringe privately owned rights. Reference herein to any specific commercial product, process, or service by trade name, mark, manufacturer, or otherwise, does not necessarily con-

stitute or imply its endorsement, recommendation, or favoring by the United States Government or any agency thereof or any other sponsor. Results reported in the LLE Review should not be taken as necessarily final results as they represent active research. The views and opinions of authors expressed herein do not necessarily state or reflect those of any of the above sponsoring entities.

The work described in this volume includes current research at the Laboratory for Laser Energetics, which is supported by New York State Energy Research and Development Authority, the University of Rochester, the U.S. Department of Energy Office of Inertial Confinement Fusion under Cooperative Agreement No. DE-FC03-92SF19460, and other agencies.

For questions or comments, contact Igor Igumenshchev, Editor, Laboratory for Laser Energetics, 250 East River Road, Rochester, NY 14623-1299, (585) 275-4792.

Worldwide-Web Home Page: <http://www.lle.rochester.edu/>

Printed in the United States of America

Available from

National Technical Information Services

U.S. Department of Commerce

5285 Port Royal Road

Springfield, VA 22161

Price codes: Printed Copy A04

Microfiche A01

# LLE Review

## Quarterly Report



### Contents

In Brief .....	iii
Laser-Driven Magnetic Flux Compression for Magneto-Inertial Fusion.....	65
Gain Curves and Hydrodynamic Simulations of Ignition and Burn for Direct-Drive Fast-Ignition Fusion Targets.....	74
Femtosecond Optical Generation and Detection of Coherent Acoustic Phonons in GaN Single Crystals.....	88
Subsurface Damage and Microstructure Development in Precision Microground Hard Ceramics Using MRF Spots.....	98
Spectral Filtering in a Diode-Pumped Nd:YLF Regenerative Amplifier Using a Volume Bragg Grating .....	115
Impact of Transverse Spatial-Hole Burning on Beam Quality in Large-Mode-Area Yb-Doped Fibers .....	120
Time-Dependent Nuclear Measurements of Mix in Inertial Confinement Fusion .....	130
Publications and Conference Presentations	



## In Brief

This volume of the LLE Review, covering the period January–March 2007, features “Laser-Driven Magnetic Flux Compression for Magneto-Inertial Fusion,” by O. V. Gotchev, N. W. Jang, J. P. Knauer, M. D. Barbero, and R. Betti (LLE and the Fusion Science Center for Extreme States of Matter and Fast Ignition Physics); and C. K. Li and R. D. Petrasso (Plasma Science and Fusion Center, MIT). In this article (p. 65), the authors report on an experiment to explore the magneto-inertial fusion (MIF) approach to inertial confinement fusion. In MIF, a magnetized target would be directly irradiated by a laser to compress a preseeded magnetic flux to levels sufficient to inhibit thermal transport out of the hot spot. This approach could eventually lead to ignition of massive shells, imploded at low velocity. Higher gain than that possible with conventional ICF could be reached. In this initial OMEGA experiment, a compact magnetic pulse system is used to generate a  $>0.15$ -MG seed magnetic field in a cylindrical target that is compressed by 40 OMEGA beams. A proton deflectometry technique is being developed to probe the magnetic field using 14.7-MeV protons generated by an independently targeted (with the 20 remaining beams) capsule filled with  $D^3He$  gas.

Additional highlights of research presented in this issue include the following:

- A. A. Solodov, R. Betti, J. A. Delettrez, and C. Zhou (LLE and the Fusion Science Center for Extreme States of Matter and Fast Ignition Physics) present results of hydrodynamic simulations of high-gain, fast-ignition targets, including one-dimensional simulations of the implosion and two-dimensional simulations of ignition by a collimated electron beam and burn propagation (p. 74). These simulations are used to generate gain curves for fast-ignition, direct-drive inertial confinement fusion. It is found that realistic fast-ignition targets can be ignited by monoenergetic collimated electron beams with a radius of  $20\ \mu\text{m}$ , duration of 10 ps, and energy of 15 kJ. Simulations using ponderomotive temperature scaling for fast electrons and Gaussian laser pulses predict a minimum laser energy for ignition of 235 kJ (106 kJ) for the energy conversion efficiency from the laser to fast electrons of 0.3 (0.5) and a wavelength of  $1.054\ \mu\text{m}$ .
- S. Wu (Department of Physics and LLE); P. Geiser, J. Jun, and J. Karpinski (Solid State Laboratory, ETH, Zurich, Switzerland); and R. Sobolewski (Department of Electrical and Computer Engineering and LLE) report on experimental and theoretical studies of the time-resolved generation and detection of coherent acoustic phonons (CAP's) in very high quality bulk GaN single crystals (p. 88). These studies are performed using a femtosecond, two-color, all-optical pump/probe technique.
- S. N. Shafirir, J. C. Lambropoulos, and S. D. Jacobs (Department of Mechanical Engineering, Materials Program and LLE) demonstrate the use of spots taken with magnetorheological finishing (MRF) for estimating subsurface damage depth from deterministic microgrinding for three hard ceramics: aluminum oxynitride ( $Al_{23}O_{27}N_5/ALON$ ), polycrystalline alumina ( $Al_2O_3/PCA$ ), and chemical vapor-deposited (CVD) silicon carbide ( $Si_4C/SiC$ ) (p. 98).
- A. V. Okishev, C. Dorrer, and J. D. Zuegel (LLE); V. I. Smirnov (OptiGrate); and L. B. Glebov (College of Optics and Photonics/CREOLE, University of Central Florida) report on the demonstration of instrument-limited suppression of out-of-band amplified spontaneous emission (ASE) in a Nd:YLF diode-pumped regenerative amplifier (DPRA) using a volume Bragg grating (VBG) as a spectrally

selective reflective element (p. 115). A VBG with 99.4% diffraction efficiency and 230-pm-FWHM reflection bandwidth produced a 43-pm FWHM output spectral width in an unseeded DPRA compared to 150-pm FWHM in the same DPRA with no VBG.

- Z. Jiang and J. R. Marciante discuss beam-quality factor measurements for an amplified emission source based on ytterbium-doped, large-mode-area (LMA), multimode fiber (p. 120). The measurements indicate that the beam-quality factor decreases until the gain becomes saturated. A model using spatially resolved gain and transverse-mode decomposition of the optical field shows that transverse spatial-hole burning (TSHB) is responsible for the observed behavior.
- J. R. Rygg, J. A. Frenje, C. K. Li, F. H. Séguin, and R. D. Petrasso (Plasma Science and Fusion Center, MIT); and V. Yu. Glebov, D. D. Meyerhofer, T. C. Sangster, and C. Stoeckl (LLE) present the first time-dependent nuclear measurements of turbulent mix in inertial confinement fusion. Implosions of spherical deuterated-plastic shells filled with pure He gas require atomic scale mixing of the shell and gas for the D-<sup>3</sup>He nuclear reaction to proceed (p. 130). The time necessary for Rayleigh–Taylor growth to induce mix delays the peak nuclear production time, compared to equivalent capsules filled with a D-<sup>3</sup>He mixture, by 75±30 ps, equal to half the nuclear burn duration. These observations indicate the likelihood of atomic mix at the tips of core-penetrating RT spikes.

Igor Igumenshchev  
*Editor*

# Laser-Driven Magnetic Flux Compression for Magneto-Inertial Fusion

## Introduction

Direct-drive inertial confinement fusion (ICF) has seen formidable progress in recent years.<sup>1,2</sup> The energy coupling and hydrodynamics of the implosion continue to be the dominant factors in the path to successful conversion of the incident laser energy  $E_L$  into thermonuclear burn energy  $E_{\text{TN}}$  (Ref. 3). For direct-drive implosions, the energy gain  $G = E_{\text{TN}}/E_L$  depends strongly on the implosion velocity  $V_i$  and on the coupling efficiency  $\eta_c = \eta_{\text{abs}}\eta_h$ . The dominant part of this product is the hydrodynamic efficiency  $\eta_h$ , the ratio of the kinetic energy of the implosion to the incident laser energy  $E_L$  (a few percent), while the absorption efficiency  $\eta_{\text{abs}}$  is of the order of 60% to 80% depending on the laser wavelength. It can be shown<sup>4</sup> that the gain of an ignited target scales as  $G \sim \eta_h V_i^{-2}$ , while  $\eta_h$  is approximated well with  $\eta_h \sim V_i^{-0.75} I_L^{-0.25}$ , where  $I_L$  is the laser intensity. Thus, the thermonuclear gain is roughly inversely proportional to the implosion velocity. On the other hand, successful ignition of the assembled central hot spot (the necessary condition for any gain in ICF) in conventional ICF requires that the hot spot reaches a certain temperature  $T_{\text{hs}}$  (of the order of 5-keV ion temperature), which requires high implosion velocities. This is confirmed by the scaling relations of Ref. 4, which show that  $T_{\text{hs}} \sim V_i^{1.4}$ . Too slow a compression will not compensate thermal losses and the hot spot will not reach the required temperature, although the areal density of the fuel may attain high values. These restrictions on  $V_i$  set limits on both the minimum energy for ignition and the maximum gain in conventional ICF.

In what is called a magneto-inertial fusion (MIF) implosion, an additional thermal insulation of the fuel forming the hot spot is provided by a strong magnetic field in a typical direct-drive ICF target.<sup>5</sup> The hot spot can reach ignition temperatures due to the reduced electron thermal conductivity, and then, when the nuclear burn develops, the alpha particles will also be confined to the burn region, delivering the energy needed to support the burn wave. Considering a hot spot with a characteristic radius  $R_h = 40 \mu\text{m}$ , a density of  $\sim 10 \text{ g/cc}$ , and a temperature of 5 keV, an electron-cyclotron frequency  $\omega_{\text{ce}}$  exceeding the collision frequency  $\nu_e$  is required for magnetic insulation; i.e.,  $\omega_{\text{ce}}\tau_e > 1$ ,

where  $\tau_e = 1/\nu_e$  is the collision time. This corresponds to  $B > 10 \text{ MG}$  due to the high densities (small collision times) in the hot spot. The condition for alpha-particle confinement  $r_\alpha/R_h < 1$  (where  $r_\alpha$  is the gyroradius) requires  $B > 95 \text{ MG}$  for the 3.5-MeV fusion alphas in a burning DT plasma. Such strong magnetic fields are very difficult to create externally. The largest macroscopic magnetic fields have so far been generated only by magnetic-flux compression in metallic liners driven by chemical detonation.<sup>6,7</sup> The measured upper limit that we are aware of is of the order of 10 MG (Ref. 8). Flux compression with an ICF-scale laser like OMEGA<sup>9</sup> is a possible way to obtain even stronger fields. The idea is to perform an ICF implosion in which there is a preimposed macroscopic magnetic field, amplified with the compression of the target plasma. Flux compression with a plasma “liner” was discussed by Liberman and Velikovich in Refs. 10 and 11 more than 20 years ago. In Ref. 11 the authors consider a magnetic field that is “frozen” in plasma compressed by a thin cylindrical wall. They show effective compression of the field with low field diffusion losses. Z pinches and laser ablation are mentioned as possible drivers for the hydrodynamic compression of the plasma.

The basic concept of flux compression can be described with the following simple formulas. In cylindrical geometry, neglecting the diffusion of the magnetic field, the conservation of the magnetic flux  $\Phi$  will yield an increase proportional to the reduction of the encircled area:

$$B_{\text{max}} = B_0 \left( \frac{r_0}{r_{\text{min}}} \right)^2 \frac{\Phi}{\Phi_0} = B_0 \left( \frac{r_0}{r_{\text{min}}} \right)^2. \quad (1)$$

In the general case of nonzero flux diffusion out of the confining volume, the flux compression equation is obtained from Eq. (1) by differentiation:

$$\frac{1}{B} \frac{dB}{dt} = \frac{1}{\Phi} \frac{d\Phi}{dt} - \frac{2}{r(t)} \frac{dr(t)}{dt}. \quad (2)$$

This can be expressed in terms of the implosion velocity  $V_i = -dr(t)/dt$  and the speed of resistive field diffusion  $V_f = \eta/\mu_0\delta$ ,

where  $\eta$  is the plasma resistivity,  $\mu_0$  is the permeability of vacuum, and  $\delta$  is a characteristic scale length of the conductor (plasma) shell in question. The ratio  $\text{Re}_m V_i/V_f$  is the magnetic Reynolds number, the dimensionless metric that determines the effectiveness of the flux compression scheme. It is the ratio of the convective to the dissipative term in the magnetic flux equation and as such determines the magnetohydrodynamic (MHD) regime (from ideal MHD at  $\text{Re}_m \gg 1$  to strictly resistive MHD at  $\text{Re}_m < 1$ ). The speed  $V_f$  can be obtained from the time scale<sup>12</sup> of an assumed exponential flux decay through the conductive region interface (with scale length  $\delta$ ), given by the ratio of shell inductance  $\mu_0 \pi r^2$  to resistance  $\delta/(2\pi r \eta)$  (per unit axial length):

$$\tau = -\left(\frac{d \ln \Phi}{dt}\right)^{-1} = \frac{\mu_0 r \delta}{2\eta} = \frac{r}{2V_f}.$$

Expressing (2) in terms of  $\text{Re}_m$  yields

$$\frac{1}{B} \frac{dB}{dt} = -\frac{2V_f}{r(t)} + \frac{2V_i}{r(t)} = -\frac{1}{r(t)} \frac{dr}{dt} \left(1 - \frac{1}{\text{Re}_m}\right) \quad (3)$$

and shows that the field will increase only if  $V_i$  is much larger than  $V_f$ , i.e.,  $\text{Re}_m \gg 1$ . Thus, when the diffusion of flux into the plasma shell due to its finite resistivity is considered, Eq. (1) is modified to

$$B_{\max} = B_0 \left(\frac{r_0}{r_{\min}}\right)^2 \left(1 - \frac{1}{\langle \text{Re}_m \rangle}\right), \quad (4)$$

which follows from Eq. (3) for the simple case of  $\text{Re}_m$  constant in time (or equal to an appropriately chosen average value  $\langle \text{Re}_m \rangle$ ).

The OMEGA laser<sup>9</sup> is an ideal test bed for magnetic-flux-compression experiments in plasmas [Fig. 110.1(a)]. Typical implosion velocities  $V_i$  in excess of  $10^7$  cm/s, coupled with the high conductivity of the hot plasma containing the field, should keep the magnetic Reynolds number large and provide for effective compression of the seed magnetic flux. The seeding of a magnetic field in the target can be accomplished with a coil system driven by a device such as the one shown in Fig. 110.1(b) and described later in this text. In contrast to compression with metallic liners, an ICF-scale, cylindrical-ablator shell (usually plastic) driven by a laser does not by itself trap the enclosed magnetic flux, but delivers kinetic energy to the plasma that contains the field. This is the gas fill that is ionized by the initial hydrodynamic shock to a highly conductive plasma state in which the resident seed magnetic field is captured. At the onset of the laser pulse, the rapid increase in ablation pressure drives this shock through the shell; it breaks out into the gas, filling the capsule, and fully ionizes it, raising the temperature in the gas post-shock region to about 100 eV. It is this region with a high magnetic Reynolds number (a time-averaged value of  $\text{Re}_m > 60$  is obtained from the simulations) that traps the magnetic field. The colder and more-resistive shell then provides the mechanical work for compression of this plasma and the field embedded in it. Figure 110.2 shows the simulated electron-temperature

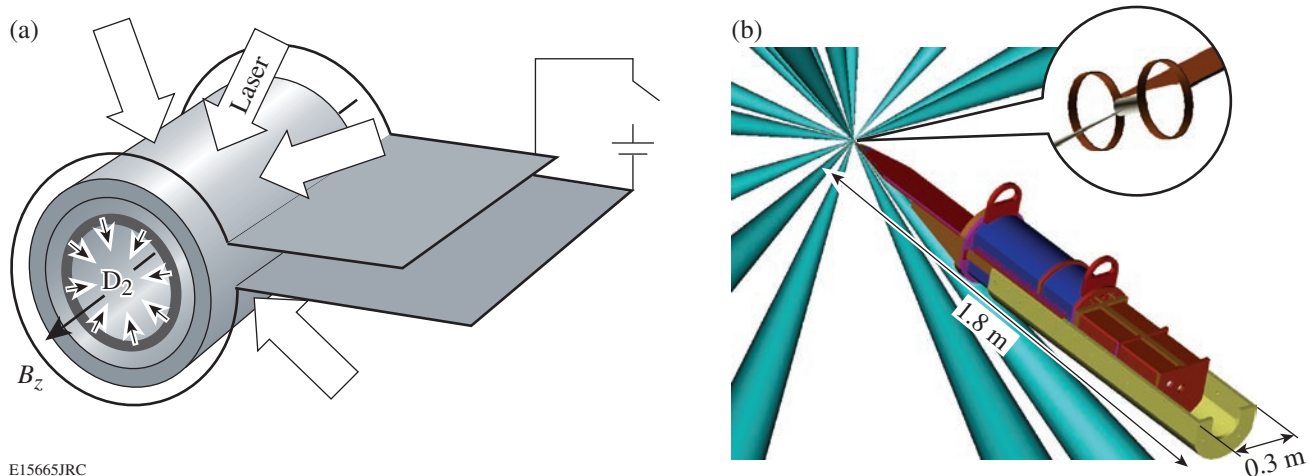
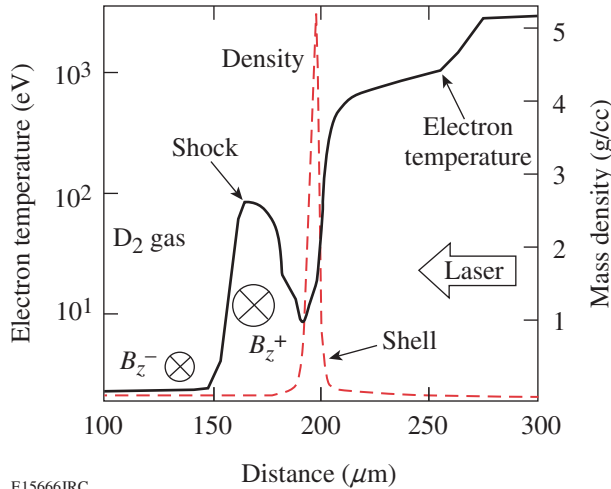


Figure 110.1

(a) Target-coil geometry for magnetic-flux-compression experiments. The cylindrical target is compressed radially by the laser beams. A single-turn coil delivers the seed magnetic pulse. (b) A compact, capacitive discharge system designed for integration in multibeam OMEGA experiments drives the current in the coils.



E15666JRC

Figure 110.2

The imploding shell (peak in dashed curve) compresses the shock-ionized gas fill that has trapped the axial magnetic field in the hot post-shock region.

profile in the  $D_2$  gas fill during shock propagation. This is for a 1.5-mm-long, 860- $\mu\text{m}$ -diam, 20- $\mu\text{m}$ -thick cylindrical plastic shell filled with 3 atm of  $D_2$ . The plastic shell can be identified in the density profile plotted at the same time. It is interesting to note that there is diffusion of magnetic flux out of the post-shock region not only through the shell but also into the unshocked gas inside the target (Fig. 110.2). This is driven by the steep gradient in resistivity and the short scale length of the shock interface, leading to a very large value of the diffusion speed. The simulation confirms it with an increase in the magnetic field ahead of the shock. The shock-front diffusion speed is

$$V_f = \frac{\eta^-}{\mu_0} \frac{1}{B_z^-} \frac{\partial B_z^-}{\partial r}, \quad (5)$$

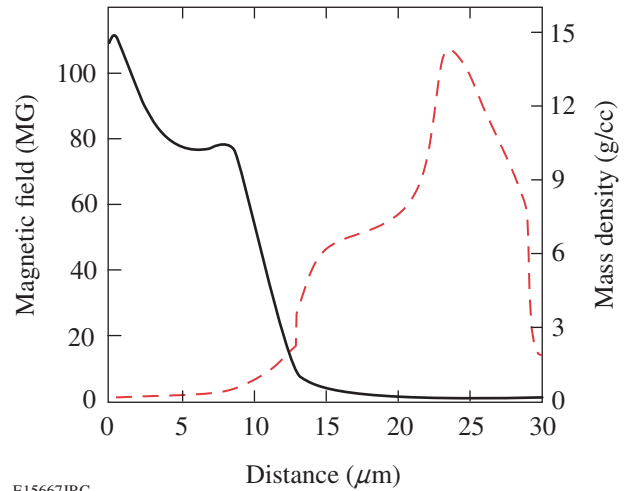
where the “-” denotes the pre-shock region. For our case, if we consider the good approximation  $\eta^- \gg \eta^+ \rightarrow 0$ , an integration of the induction equation across the shock will yield a jump condition written in the frame of reference of the shock front moving with velocity  $u_s$ ,

$$u_s B_z^- - \frac{\eta^-}{\mu_0} \frac{\partial B_z^-}{\partial r} = (u_s - V_i) B_z^+. \quad (6)$$

This can be rewritten as

$$\frac{B_z^+}{B_z^-} = \frac{u_s - V_f}{u_s - V_i}. \quad (7)$$

This ratio shows that field cumulation in the post-shock region (large field ratio) needs large  $V_i$ , while  $V_f$  acts to reduce the field jump by raising the field ahead of the shock. In contrast, at the ionized gas-shell interface, the resistivity scale length is larger and the shell plasma is a conductor, albeit not as good as the plasma in the post-shock region. This leads to lower outward diffusion of the field and net flux compression due to the high convergence velocity of the shell. The field and density profiles at the center of the target, as simulated by *LILAC-MHD*,<sup>13</sup> are shown in Fig. 110.3 for the time of peak compression. One can see that in the hot spot (in this case the central 20  $\mu\text{m}$  of the target) the magnetic field reaches the values (>95 MG) needed for alpha-particle confinement in a DT fusion target. The result is a six-fold increase in the simulated stagnation ion temperature to >7 keV, when compared to a simulation with no seed field.



E15667JRC

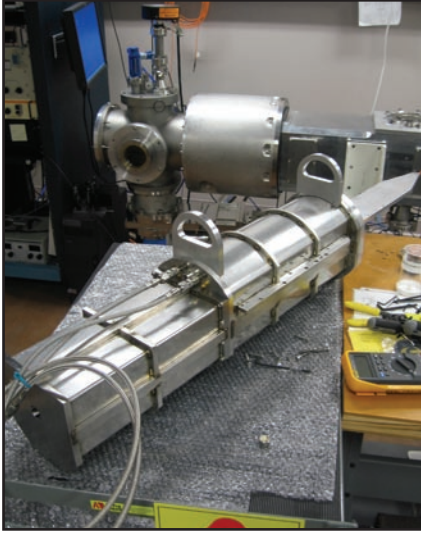
Figure 110.3

*LILAC-MHD* results for a 3-atm,  $D_2$ -filled CH capsule at the time of peak compression: field (solid curve) and density (dashed curve) profiles at the target center.

### MIFEDS (Magneto-Inertial Fusion Energy Delivery System) Seed-Field Generator

To obtain multi-mega-gauss fields with the laser-driven flux-compression (LDFC) scheme, it is necessary to start from substantial seed-field values due to the limit in maximum convergence ratio of the compression. For a cylindrical geometry [Fig. 110.1(a)], the convergence ratio is between 10 and 20. Supplying tens of tesla to the target chamber center of OMEGA is nontrivial since the parametric space is restricted on one side by the small physical volume available and on the other by the need of high energy in the magnetic pulse. This is actually a high-power requirement because of the short duration of an

OMEGA implosion (1-ns pulses are used in the experiments). A compact device shown in Fig. 110.4 [see also Fig. 110.1(b)] generating seed magnetic fields of sufficient strength (up to 0.15 MG measured) was built to test the laser-driven magnetic-flux-compression concept. It fits in a diagnostic insertion port on the OMEGA chamber, stores not more than 150 J, and provides magnetic pulses with an intensity of 0.1 to 0.15 MG and  $\sim 400$ -ns duration.



E15668JRC

Figure 110.4  
MIFEDS device in the diagnostic TIM (ten-inch manipulator) facility.

The interaction volume in the OMEGA target chamber is characterized by the target size and is thus limited to a linear dimension of a few millimeters. This small volume is in the field of view of an extensive suite of diagnostics, pointed at the target chamber center from various angles and occupying conical space envelopes that should not be broken to prevent beam clipping or conflict/collision with other diagnostics. For the LDFC scheme described above, a magnetic pulse of sufficient strength must be delivered to the target interaction volume within such an envelope, and the field must be created by coils that do not obscure laser beams aimed at the target nor the view of the various diagnostics. Such restrictions point at low-mass, single-turn coils as the best solution. For a cylindrical target configuration, a Helmholtz-type coil provides advantageous geometry since a large number of laser beams can be pointed at the target in between the two coils without obscuration. An optimization of the field-to-coil current ratio

$$B_z/I \approx \mu_0 R^2 \left( R^2 + D^2/4 \right)^{-3/2}, \quad (8)$$

with the incident laser beams taken into account, leads to a choice of radius  $R$  for each and separation  $D$  between the coils that deviates from the standard Helmholtz coil where  $R = D$ . In the design suitable for OMEGA experiments,  $R = 2.0$  mm and  $D = 4.4$  mm. Figure 110.1(b) shows a cylindrical target with a typical diameter of  $860 \mu\text{m}$  as it is placed between coils with the above dimensions. The coils were made from copper-clad Kapton foil with a thickness of  $100 \mu\text{m}$  and an individual coil width of  $0.5$  mm. The inductance of such a single-turn coil is very low. The calculated value, obtained from both an analytical formula and simulations of the coil's magnetic energy with the magnetostatic code Radia,<sup>14</sup> was  $\sim 25$  nH, consistent with measurements. To receive most of the energy stored in the charging circuit, the coil inductance must be the dominant portion of the total circuit inductance. If this is observed, the resulting low-inductance circuit will provide the stored energy in a very fast discharge pulse. Since our reference time scale—the duration of the laser-driven implosion—is less than  $3$  ns, this fast discharge is warranted, reducing the total energy required for the generation and support of the seed magnetic field. A discharge pulse that lasts hundreds of nanoseconds will provide a large time window at peak current/field. A very fast discharge is, in fact, required with this type of low-mass ( $9$ -mg total measured mass of the two turns in the base design) coil since the peak current values must be reached before the joule heating destroys the coil and quenches the current rise. The rate of temperature rise, determined from the specific heating rate  $j^2\eta$ , where  $j$  is the current density and  $\eta$  is the resistivity, can be written as  $c_p dT/dt = j^2\eta$ , with  $c_p$  being the specific heat of solid copper, generally a function of temperature. By integrating this relation, we obtain the “fuse” action integral

$$\int_{T_0}^{T_1} \frac{c_p}{\eta} dT = \int_0^{t_p} j^2 dt, \quad (9)$$

which relates the material properties to the time integral of the current density. At some value of this integral, the coils will melt and the current will be interrupted. Since  $j$  is set by the peak field requirement to minimize the action integral, we need to reduce the time of current propagation  $t_p$ . Whether this time will be sufficient for the current to reach its peak value is determined by comparing  $t_p$  to the time constant  $\tau = L/R$  of the discharge. Expressing the joule heating energy deposited from  $t = 0$  to  $t_p$ , in terms of the peak current  $I_{\text{max}}$  and the average resistance  $\bar{R}(B, T)$ , and using the time constant  $\tau$ , we obtain the ratio of the maximum magnetic energy  $E_m(t_p)$  to the heating in the coils, as the ratio of the pulse rise time  $t_p$  to the circuit time constant,

$$E_j(t_p) = \int_0^{t_p} R(t)I^2 dt \approx \bar{R}(B, T) \frac{I_{\max}^2}{2} t_p$$

$$\approx \frac{t_p}{2\tau} LI_{\max}^2 \approx \frac{t_p}{\tau} E_m(t_p). \quad (10)$$

This ratio needs to be minimized for the most-efficient energy transfer. Based on these considerations, we have chosen a capacitor bank consisting of two 100-nF capacitors connected in parallel, with total inductance of ~8 nH. These are S-series<sup>15</sup> plastic case capacitors (Fig. 110.5) from General Atomics, rated for 40 kV, and pulsed currents of 50 kA. Their combined ESR value for the fundamental frequency of the discharge is less than 2.5 mΩ. Charged to their rated voltage, the capacitors can store 160 J but have been used routinely at 30-kV charge voltage, storing 90 J of energy. The same restrictions (as-low-as-possible inductance and resistance) apply to the discharge switch and transmission wiring. In the design, a very-low-inductance, coaxial, laser-triggered spark gap is mounted directly to the capacitors, while the return path consists of two 3-in.-wide copper bars (Fig. 110.5). This compact package can fit in a small vessel that can be placed in an OMEGA TIM (ten-inch manipulator) along with its dedicated charging circuitry. This way, the transmission length is greatly reduced in favor of the desired small overall inductance, and no high-voltage lines are fed into the target chamber.

A CAD drawing of the MIFEDS device as placed in the TIM rolling platform is shown in Fig. 110.6. There are two

distinct compartments: In the front is the energy storage and switch block, while the charger and protection circuitry are located in the back. There is a metal barrier between the compartments, with openings only for the trigger beam and the charging cables. This way, the capacitive coupling of noise from the rapid, high-current discharge in the front into the components in the back is reduced. Those components consist of (a) the power supply—a 30-W dc-to-dc converter<sup>16</sup> with a supply voltage of 24-V dc and a rated peak voltage of 40 kV

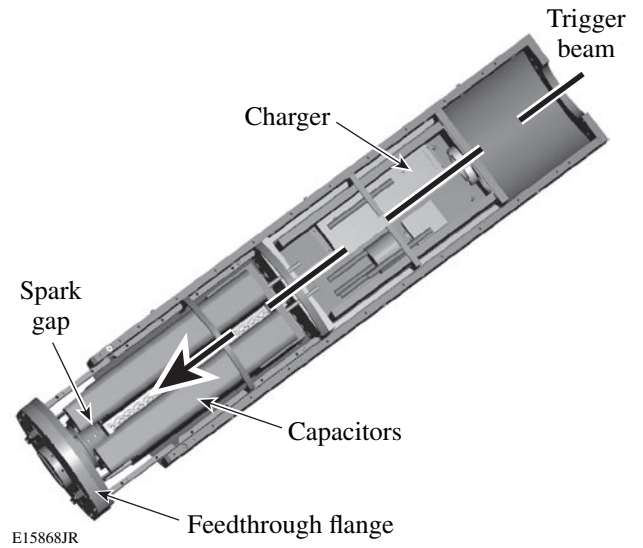


Figure 110.6  
CAD drawing of the main MIFEDS components inside the air box that is mounted to the TIM rolling platform.

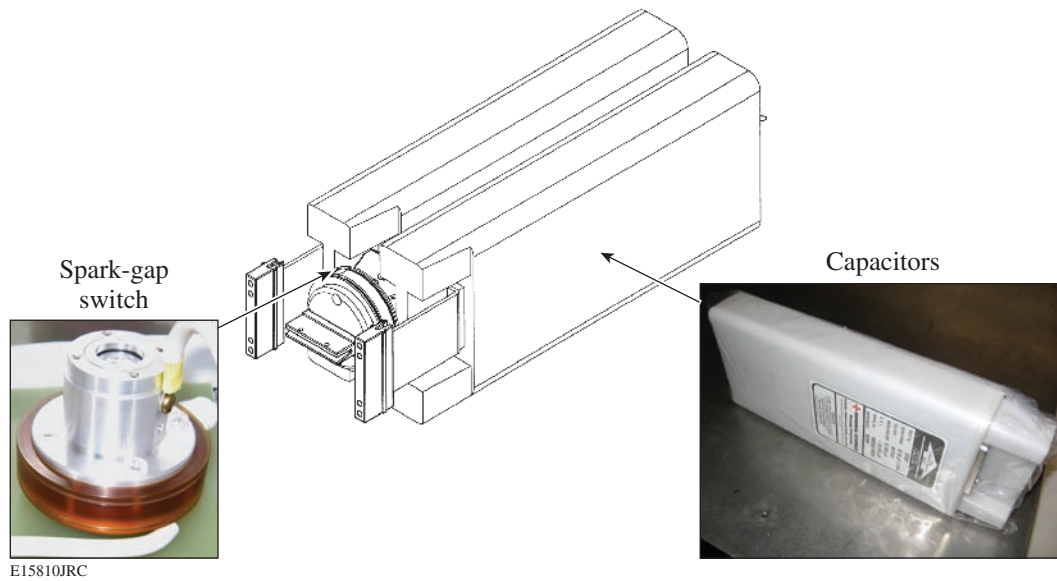


Figure 110.5  
Low-inductance assembly of the energy storage capacitors and the laser-triggered spark-gap switch. The actual devices are also shown.

at maximum current of 750  $\mu\text{A}$ ; (b) a high-voltage relay, used to dump to ground the residual energy immediately after discharge; and (c) an array of diodes and current-limiting resistors to protect the high-voltage power supply from reverse voltage transients, a pressure sensor, a low-voltage solid-state relay, and an interface board to monitor and control the charge cycle. Careful packaging was necessary to be able to place and safely operate these components at  $>30$  kV. Care was taken to provide a clear optical path for the trigger laser beam along the axis of the air box.

**Magnetic-Field Measurements**

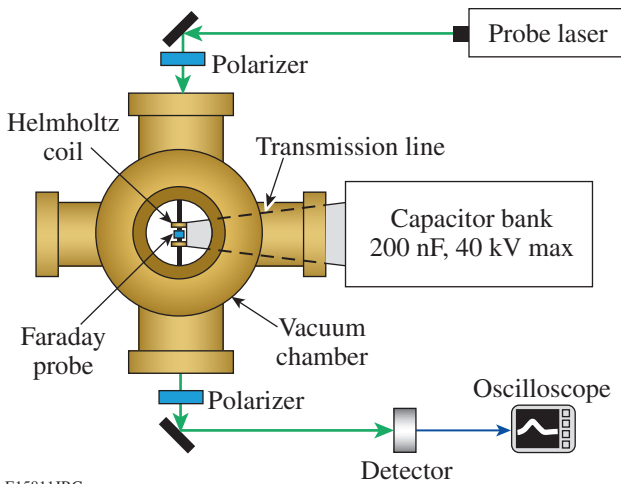
The main diagnostic method for the seed magnetic field during the development of MIFEDS has been magneto-optical. Faraday rotation (Fig. 110.7) was used to measure the fields generated between the MIFEDS coils when testing coil geometry, transmission line design, and the high-voltage switch. The probe laser was a temperature-stabilized, frequency-doubled, cw Nd-YAG laser providing 50 mW of power at 532-nm wavelength. The probe, placed between the two coils, was a 1-mm-thick, terbium-doped glass disk with a 1.5-mm diameter and Verdet constant  $V = 100 \text{ radT}^{-1}\text{m}^{-1}$ . Because of the strong fields expected, the two polarizers were coaligned for maximum transmission of the linearly polarized laser light; this is not the highest sensitivity configuration but the easiest to work with, especially when rotation angles larger than  $90^\circ$  are possible. The drop in the signal due to Faraday rotation in the glass sample during the magnetic pulse was then observed and the field determined from the detected light intensity  $I_{\text{det}}(t)$ ,  $I_{\text{det}}(t) = I_0 \cos^2[\theta_{\text{rot}}(t)]$ , where  $\theta_{\text{rot}}(t) = V\bar{B}_z(t)d_z$  is the Faraday

rotation angle as a function of the average axial field in the sample and its thickness  $d_z$ . Figure 110.8 shows the change in laser intensity triggered by the Faraday rotation and recorded by a fast optical detector connected to an oscilloscope. Three intensity traces show very repetitive magnetic pulses with an average pulsewidth of  $\sim 400$ -ns FWHM and decay time of the order of  $1.5 \mu\text{s}$ . The maximum magnetic field at the center of the coil ranges from 14 to  $15.7 \pm 0.3 \text{ T}$  ( $10 \text{ T} = 0.1 \text{ MG}$ ). These fields correspond to a total coil current of 79.3 kA for a separation  $D = 2.4 \text{ mm}$  and a coil radius of 2 mm used in these tests. The magnetostatic Radia simulations,<sup>14</sup> which account for the aspect ratio of the coil, gave a total current of 76 kA for the same peak field.

A simple analytical model was developed to look at the temporal behavior of the coil current. It is based on the equivalent, damped LRC circuit, where the reference damping  $\alpha$  was given by an average value of the time-dependent coil resistance. The current from the model,

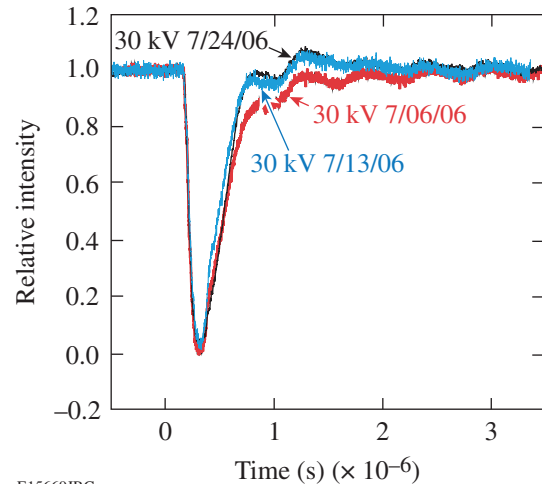
$$I_{\text{mod}}(t) = \frac{\omega_0^2 + \alpha^2}{\sqrt{\omega_0^2 - \alpha^2}} CV_{\text{max}} \exp(-\alpha t) \sin(\sqrt{\omega_0^2 - \alpha^2} t), \quad (11)$$

where  $V_{\text{max}}$  is the charging voltage,  $C$  is the capacitance, and  $\omega_0$  is the fundamental frequency of the circuit, was then converted to the equivalent Faraday rotation signal, using Eq. (8). The best-fit parameters were sought and the fit is shown in Fig. 110.9. The best-fit parameters are  $R_{\text{avg}} = 0.21 \Omega$ ,  $\omega_0 = 8.78 \times 10^6 \text{ rad/s}$ , and  $\alpha = 2.1 \times 10^6 \text{ rad/s}$ . From the fit we then determined a total circuit inductance of 65 nH, which is in line with calculations for the individual components. The agreement between the



E15811JRC

Figure 110.7 Faraday rotation setup for the measurement of the seed magnetic fields on the benchtop.



E15669JRC

Figure 110.8 Faraday rotation data over two weeks of MIFEDS discharges. The data show good repeatability with a pulse duration of  $\sim 400$ -ns FWHM and a rise time of  $\sim 160$  ns.

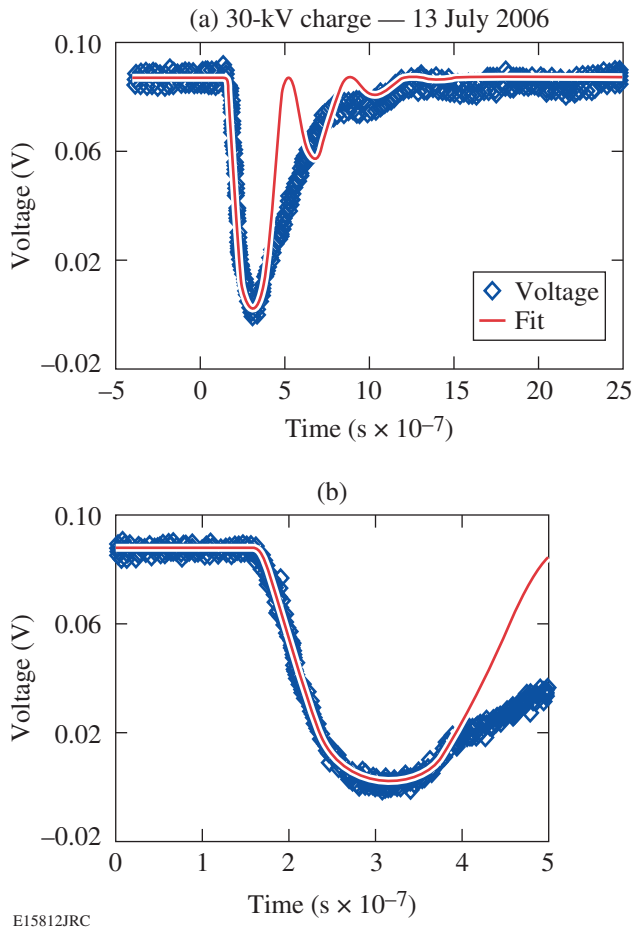


Figure 110.9  
A simple analytical model was fit to the data. It matches the experiment very well until after the current peak.

experiment and the analytical model is very good until after the peak of the current pulse. At later times, the experimental data show rapid change in the time-dependent resistance of the circuit, which becomes overdamped. Several possible reasons for that include joule heating in the coil, extinguishing of the streamer in the spark-gap switch, or even change in the contact resistance somewhere in the transmission path. From a design standpoint this is beneficial since we are able to reach the peak current while the load is less resistive. The detrimental voltage reversal, characteristic of underdamped circuits, is avoided with this rapid increase of the circuit resistance.

**Initial Experiments on OMEGA**

Before testing it on OMEGA, the MIFEDS device was qualified in the diagnostic TIM facility, where a number of discharges were performed to monitor the charge cycle, EMI noise, gas pressure stability, and other parameters. The interfacing of MIFEDS to the diagnostic TIM closely emulated the OMEGA chamber/TIM setup (shown in Fig. 110.10). An optical Faraday rotation setup was arranged and the magnetic field pulses were recorded. The precise time delay from the triggering of a discharge to the time of peak magnetic field was established. The delay was highly repetitive at 310 ns with standard deviation of about 18 ns. One of the concerns was the survival of the cylindrical target during the rise time of the magnetic pulse. The possibility of destroying the target before the laser shot endangers the OMEGA laser components since some of the unterminated beams can back-propagate at full energy. A special safety circuit was implemented to prevent the propagation of OMEGA beams in the case of MIFEDS prefire (Fig. 110.10). It is connected to a pickup coil placed at the spark-gap switch in MIFEDS to detect the current pulse.

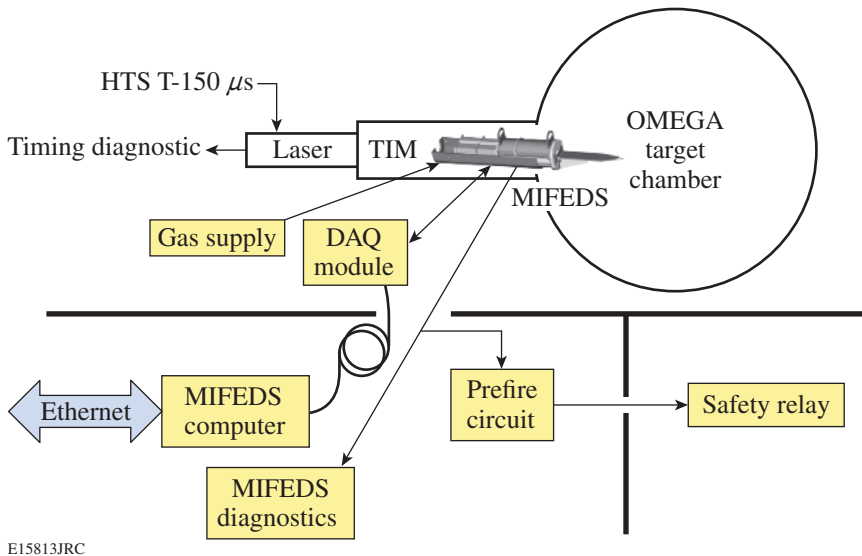


Figure 110.10  
Setup of the MIFEDS infrastructure in the OMEGA Target Bay. The three main components are the switching, control and monitoring, and safety circuits.

It was established that the target needs a 100-nm Al overcoat to provide reasonable retention of the gas at 3- to 5-atm pressure. This raised an important question about the time needed by the seed field to diffuse through the aluminum before an OMEGA shot. If the field is excluded from the inside of the target, the consequent flux compression would be impeded. For this purpose we designed a special experiment in the diagnostic TIM facility, using the Faraday rotation setup. An aluminized CH shell with all of the target parameters except for size (its diameter was 1.5 mm to accommodate a Faraday rotator glass sample) was placed between the MIFEDS coils, and several discharges were performed. The difference in the magnetic pulse rise time of these discharges and the earlier experiments with the stand-alone Faraday probe was within a typical time jitter of 16 ns. From this, it was concluded that the Al layer, much thinner than the skin depth of  $60\ \mu\text{m}$  at the fundamental frequency of the pulse, was not a barrier for the seed field.

Initial experiments were conducted to integrate MIFEDS into OMEGA and test the experimental geometry, to develop the proton backlighter diagnostic, and to measure the convergence ratio of cylindrical implosions. Forty OMEGA beams were radially incident on the cylindrical target, while the remaining 20 were used to generate 14.7-MeV probe protons in a separate  $\text{D}^3\text{He}$ -filled glass shell for magnetic-field measurement. The technique is a further development of the one described in Ref. 17. Figure 110.11(a) shows a typical configuration with a cylindrical target mounted between the MIFEDS coils and imaged with the OMEGA Target Viewing System. One can also see the outlines of rectangular and circular poly-

imide plugs used in this case, as well as the crossbeam on the target stalk used to correctly orient the axis of the cylinder. The inset shows a time-integrated, x-ray self-emission image of the imploded target. The enhanced emission of x rays with average energy in the 1-keV range is seen from the hot compressed core. The  $450\text{-}\mu\text{m}$ -diam glass microballoon used as the proton backlighter is visible in the lower right corner. From these experiments, the time of peak compression was established to within 100 ps. In comparison, the duration of the proton burst is  $\sim 150$  ps (Ref. 17). The detector medium for the protons is a two-layer package of 1-mm-thick, CR-39 plastic track detectors, shielded by Al filters. The initially chosen filter thickness was not optimal, as can be seen from Fig. 110.11(b) where the proton density map at the surface of the second CR-39 detector is shown. The darker areas have a higher proton density. One can see the deficiency of protons in the area of the compressed core, which is undesirable since these are the particles to be deflected by the compressed fields. Monte Carlo simulations based on the experimental data are ongoing to identify the optimal filter thickness for the next experiment. The goal is to match to the CR-39 detector surface a specific portion of the energy loss versus depth curve (near but before the Bragg peak) of the particles that traverse the compressed core, so that these specific particles are centered in the limited readout energy band with a maximum signal-to-noise ratio. Upcoming experiments will utilize the improved detector geometry.

## Conclusions

The concept of laser-driven magnetic-flux compression was briefly introduced with emphasis on its application to the

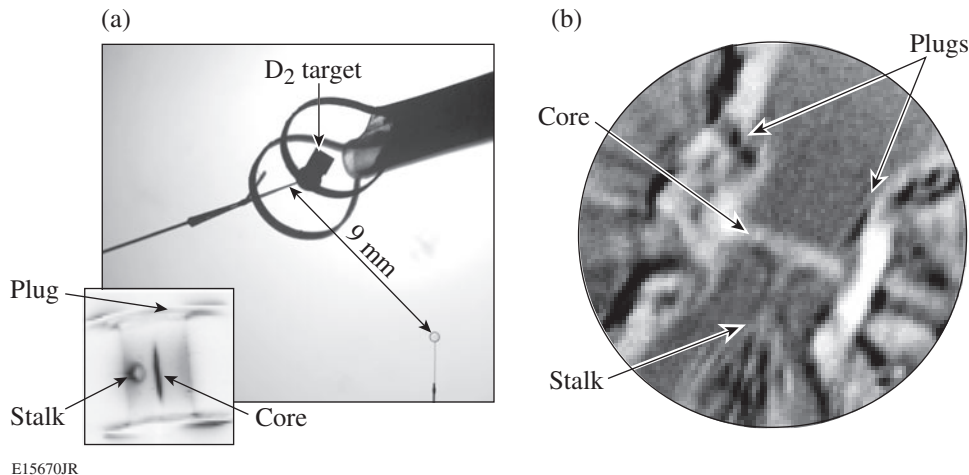


Figure 110.11

(a)  $\text{D}_2$ -filled shell placed between the MIFEDS coils and imaged with the OMEGA Target Viewing System. The proton backlighter is visible in the lower right. The inset depicts a time-integrated x-ray self-emission image showing the enhanced emission from the compressed hot core. (b) Density map of protons imaging the target near peak compression. The protons passing through the core are slowed down below the detection threshold.

improvement of direct-drive laser fusion. The confinement and amplification of seeded magnetic flux in cylindrical, D<sub>2</sub>-filled plastic shells, irradiated by the OMEGA laser, were discussed in this context. A gigawatt seed-field generator that can discharge 100 J of energy in 400 ns was designed and built in a compact package for these experiments. Its spatial and temporal parameters were optimized for the delivery of a strong magnetic pulse in the small (a few tens of mm<sup>3</sup>) laser–target interaction volume of OMEGA. Seed magnetic fields larger than 0.15 MG were measured in the center of the low-mass double-coil assembly. A proton deflectometry technique is being developed for the observation of the flux compression in an optically thick cylindrical target. The initial proton back-lighting experiments helped establish the relative timing of the proton pulse with respect to the time of peak convergence of the target. The data aided the matching of the CR-39 detector surface with the appropriate portion of the dose versus depth curve (near but before the Bragg peak) for the protons that are slowed down through the core. These form the basis for future flux-compression experiments, first in cylindrical and later in spherical geometry. Applications of the laser-driven flux compression will not be limited to ICF studies. Work is in progress to use the seed field for OMEGA experiments in the context of laboratory astrophysics experiments, such as magnetized plasma jets. In addition, a scheme that uses moderate flux compression in cylindrical geometry is being evaluated for the confinement of electron–positron plasma<sup>18</sup> generated in an integrated OMEGA/OMEGA EP<sup>19</sup> experiment.

#### ACKNOWLEDGMENT

One of the authors (O. V. Gotchev) would like to thank Dr. A. V. Okishev, W. A. Bittle, G. Brent, and G. Raffaele-Addamo for their expert advice and helpful discussions. This work was supported by the U.S. Department of Energy Office of Fusion Energy Sciences under Grants DE-FG02-04ER54768 and DE-FC02-ER54789 and by the Office of Inertial Confinement Fusion under Cooperative Agreement No. DE-FC52-92SF19460, as well as the University of Rochester and the New York State Energy Research and Development Authority. The support of DOE does not constitute an endorsement by DOE of the views expressed in this article.

#### REFERENCES

1. S. E. Bodner, D. G. Colombant, J. H. Gardner, R. H. Lehmborg, S. P. Obenschain, L. Phillips, A. J. Schmitt, J. D. Sethian, R. L. McCrory, W. Seka, C. P. Verdon, J. P. Knauer, B. B. Afeyan, and H. T. Powell, *Phys. Plasmas* **5**, 1901 (1998).
2. R. L. McCrory, D. D. Meyerhofer, S. J. Loucks, S. Skupsky, R. Betti, T. R. Boehly, T. J. B. Collins, R. S. Craxton, J. A. Delettrez, D. H. Edgell, R. Epstein, K. A. Fletcher, C. Freeman, J. A. Frenje, V. Yu. Glebov, V. N. Goncharov, D. R. Harding, I. V. Igumenshchev, R. L. Keck, J. D. Kilkenny, J. P. Knauer, C. K. Li, J. Marcianti, J. A. Marozas, F. J. Marshall, A. V. Maximov, P. W. McKenty, S. F. B. Morse, J. Myatt,

- S. Padalino, R. D. Petrasso, P. B. Radha, S. P. Regan, T. C. Sangster, F. H. Séguin, W. Seka, V. A. Smalyuk, J. M. Soares, C. Stoeckl, B. Yaakobi, and J. D. Zuegel, *J. Phys. IV France* **133**, 59 (2006).
3. R. Betti, K. Anderson, T. R. Boehly, T. J. B. Collins, R. S. Craxton, J. A. Delettrez, D. H. Edgell, R. Epstein, V. Yu. Glebov, V. N. Goncharov, D. R. Harding, R. L. Keck, J. H. Kelly, J. P. Knauer, S. J. Loucks, J. A. Marozas, F. J. Marshall, A. V. Maximov, D. N. Maywar, R. L. McCrory, P. W. McKenty, D. D. Meyerhofer, J. Myatt, P. B. Radha, S. P. Regan, C. Ren, T. C. Sangster, W. Seka, S. Skupsky, A. A. Solodov, V. A. Smalyuk, J. M. Soares, C. Stoeckl, W. Theobald, B. Yaakobi, C. Zhou, J. D. Zuegel, J. A. Frenje, C. K. Li, R. D. Petrasso, and F. H. Séguin, *Plasma Phys. Control. Fusion* **48**, B153 (2006).
4. R. Betti and C. Zhou, *Phys. Plasmas* **12**, 110702 (2005).
5. P. W. McKenty, V. N. Goncharov, R. P. J. Town, S. Skupsky, R. Betti, and R. L. McCrory, *Phys. Plasmas* **8**, 2315 (2001).
6. C. M. Fowler, W. B. Garn, and R. S. Caird, *J. Appl. Phys.* **31**, 588 (1960).
7. A. D. Sakharov *et al.*, *Sov. Phys. Doklady AN SSSR* **165**, 65 (1965).
8. A. I. Bykov *et al.*, *Physica B* **294–295**, 574 (2001).
9. T. R. Boehly, D. L. Brown, R. S. Craxton, R. L. Keck, J. P. Knauer, J. H. Kelly, T. J. Kessler, S. A. Kumpan, S. J. Loucks, S. A. Letzring, F. J. Marshall, R. L. McCrory, S. F. B. Morse, W. Seka, J. M. Soares, and C. P. Verdon, *Opt. Commun.* **133**, 495 (1997).
10. M. A. Liberman and A. L. Velikovich, *J. Plasma Phys.* **31**, 369 (1984).
11. A. L. Velikovich *et al.*, *Sov. Phys.-JETP* **61**, 261 (1985).
12. F. Herlach, *Rep. Prog. Phys.* **62**, 859 (1999).
13. N. W. Jang, R. Betti, J. P. Knauer, O. Gotchev, and D. D. Meyerhofer, *Bull. Am. Phys. Soc.* **51**, 144 (2006).
14. O. Chubar, P. Elleaume, and J. Chavanne, *J. Synchrotron Radiat.* **5**, 481 (1998).
15. Series S/SS High Voltage Rep-Rate Capacitors, General Atomics Energy Products, General Atomics Electronic Systems, Inc., San Diego, CA 92123, <http://www.gaep.com/series-s-ss-capacitors.html> (18 June 2007).
16. 40A Series, part no. 40A24N30, Ultravolt, Inc., Ronkonkoma, NY 11779, <http://www.ultravolt.com/coa-40aser.htm> (18 June 2007).
17. C. K. Li, F. H. Séguin, J. A. Frenje, J. R. Rygg, R. D. Petrasso, R. P. J. Town, P. A. Amendt, S. P. Hatchett, O. L. Landen, A. J. Mackinnon, P. K. Patel, V. Smalyuk, J. P. Knauer, T. C. Sangster, and C. Stoeckl, *Rev. Sci. Instrum.* **77**, 10E725 (2006).
18. J. Myatt, A. V. Maximov, and R. W. Short, *Bull. Am. Phys. Soc.* **51**, 25 (2006).
19. L. J. Waxer, D. N. Maywar, J. H. Kelly, T. J. Kessler, B. E. Kruschwitz, S. J. Loucks, R. L. McCrory, D. D. Meyerhofer, S. F. B. Morse, C. Stoeckl, and J. D. Zuegel, *Opt. Photonics News* **16**, 30 (2005).

---

# Gain Curves and Hydrodynamic Simulations of Ignition and Burn for Direct-Drive Fast-Ignition Fusion Targets

## Introduction

In fast-ignition<sup>1</sup> inertial confinement fusion (ICF) a cryogenic shell of deuterium and tritium (DT) is first imploded by a high-energy driver to produce an assembly of thermonuclear fuel with high densities and areal densities. Such a dense core is then ignited by the fast electrons (or protons) accelerated through the interaction of a high-power, ultra-intense laser pulse with either a coronal plasma or a solid, cone-shaped target.<sup>2,3</sup> The fast particles slow down in the cold, dense fuel and deposit their kinetic energy through collisions with the background plasma. In direct-drive fast ignition, the high-energy driver is typically a laser with a wavelength  $\lambda_L \approx 0.25, 0.35,$  or  $0.53 \mu\text{m}$ , and the high-intensity laser has a power in the petawatt range with a wavelength of  $0.53$  or  $1.06 \mu\text{m}$ . The energy gain is defined as the ratio between the thermonuclear energy yield and the laser energy on target. Such a definition does not take into account the energy required to power the lasers. Including the wall-plug efficiency of the lasers is essential to assess the ultimate validity of fast-ignition inertial confinement fusion as an economical energy source but it requires detailed considerations of the laser technology that are beyond the scope of this article. Earlier attempts<sup>4</sup> to determine the gain curves for fast ignition were based on heuristic models of the fuel assembly and thermonuclear yields. The results shown here represent a calculation of the gain curve based on realistic target designs and hydrodynamic simulations of the implosion, as well as simulations of the ignition by a collimated electron beam and burn propagation. The targets are chosen according to the design of Ref. 5, where the laser pulses and target characteristics are optimized to achieve a fuel assembly with a small hot spot, large densities, and areal densities suitable for fast ignition. Here, we consider a high-energy laser as the compression driver and focus on two forms of the thermonuclear gain. The first is the maximum gain  $G_M = E_F/E_c$  given by the ratio between the thermonuclear energy  $E_F$  and the compression laser energy on target  $E_c$ . The second is the total gain  $G_T = E_F/E_T$  defined as the ratio between the thermonuclear energy and the total laser energy on target including the petawatt laser energy  $E_T = E_c + E_{pw}$ . It is shown in this article that the maximum gain  $G_M$  is only a function of the compression laser energy and

wavelength  $G_M = G_M(E_c, \lambda_L)$ , thus leading to the following form of total gain:

$$G_T = \frac{G_M(E_c, \lambda_L)}{1 + E_{pw}/E_c}. \quad (1)$$

The second term in the denominator of Eq. (1) can be neglected for large compression lasers with  $E_c \gg E_{pw}$ , thus leading to  $G_T \approx G_M$ .

It is important to emphasize that the hydrodynamic simulations of fast-ignition (FI) targets reported in this article are meant to address only one aspect of the physics pertaining to fast ignition: the issue of the hydrodynamic fuel assembly and its potential for high energy gains. The complicated physics of the fast-electron beam generation and transport is not considered here. Instead, the  $e$ -beam is assigned as an ideal beam, collimated and uniform, with or without a Maxwellian energy spread. Likely, such an ideal beam is very different from the experimental conditions, where the beam may be broken up into filaments and become divergent. Based on the available experimental data, it is currently not possible to predict the  $e$ -beam characteristics in a fast-ignition target because most of the experiments on fast-electron generation and transport pertain to the interaction of intense light with solid targets rather than plasmas relevant to fast ignition.<sup>6</sup> Fast-electron transport properties in plasmas are vastly different than in solid targets,<sup>6</sup> and fast-ignition-relevant plasmas are difficult to produce without an implosion facility. However, the next generation of petawatt lasers such as FIREX-I<sup>7</sup> and OMEGA EP<sup>8</sup> will be combined with an implosion facility and integrated experiments will become possible. Such experiments should provide a wealth of experimental data to be used for the characterization of the fast-electron beam produced in the fast-ignition targets. In this article, the injection of an ideal electron beam is simply assumed. All of the difficulties pertaining to hot-electron generation and transport physics are buried in the parameter describing the conversion efficiency of laser light into collimated hot electrons and the hot-electron temperature.

The latter is either assigned or estimated using the widely used ponderomotive scaling formula,<sup>9</sup> derived from particle-in-cell (PIC) simulations of intense light–plasma interaction. Results based on such a formula should be taken with caution since there is no experimental confirmation that the ponderomotive scaling is applicable to fast-ignition targets. It is also worth mentioning that the conversion efficiency used here defines the conversion of laser light into an ideal collimated beam. Departures from the collimated beam configuration would cause deterioration in efficiency. Because of uncertainties in values of conversion efficiency, the results in this article are parameterized as a function of efficiency.

The hydrodynamic simulations of fast-ignition targets<sup>5</sup> reported in this article include one-dimensional (1-D) simulations of the implosion and two-dimensional (2-D) axisymmetric simulations of ignition by a collimated electron beam and burn propagation. In the case of cone-in-shell targets, the final phase of the implosion is simulated in two dimensions assuming that the cone walls are rigid and truncated at a given distance from the center. This idealized, optimistic configuration is used to estimate the deterioration of the gain due to the presence of the cone. The targets are thick shells of wetted-foam (DT)<sub>6</sub>CH with an inner DT-ice layer and a thin CH overcoat. Such targets<sup>5</sup> are designed to achieve a massive compressed core with a uniform density and a small hot spot. Because of their low in-flight aspect ratio (IFAR), such targets are not sensitive to the growth of hydrodynamic instabilities during the acceleration phase. Thus, one-dimensional simulations of the implosions provide a reasonably accurate description of the final fuel assembly (unless a cone is present).

A derivation of the gain curves for target densities around  $\rho \approx 300 \text{ g/cm}^3$  is described briefly by the same authors in Ref. 10. There, an analytic gain formula is derived and compared with the results of ignition and burn simulations of imploded targets. In Ref. 10, ignition is triggered by a monoenergetic 1- to 3-MeV electron beam with an energy of 15 kJ. The approach used in this article is similar to the one taken by Atzeni in Ref. 11 to describe the ignition conditions for a uniform-density, spherical DT plasma heated by a collimated electron beam. A major step forward in our work is that the DT plasma core is produced by simulating the implosion of realistic fast-ignition targets. Such targets are designed to produce an optimized fuel assembly for fast ignition featuring high densities, high areal densities, and small hot spots. Furthermore, our simulations of ignition and burn are extended to an entire family of fast-ignition targets, scaled for different compression driver energies, to generate a gain curve for direct-drive fast ignition.

This article presents the details of the simulation results that led to the conclusions of Ref. 10. As in Ref. 10, we use a simple parallel straight-line transport model for the fast electrons, in which the electrons lose their energy in the dense core according to the well-established relativistic slowing-down theory of Refs. 12 and 13. Furthermore, we extend the work of Ref. 10 to include sensitivity studies of ignition and gain deterioration due to the cone. The ignition sensitivity studies are carried out with respect to the electron-beam parameters (spot size, duration, electron energy), injection time, fast-electron temporal distribution, and fast-electron distribution function.

To model the energy spectrum of electrons generated by the ultra-intense laser–plasma interaction, simulations using Maxwellian electrons are performed, having ponderomotive temperature scaling with the laser intensity and the wavelength, and assuming a Gaussian temporal profile of the laser pulse. A minimum laser energy for ignition exceeding 100 kJ is found for the 1.054- $\mu\text{m}$  wavelength. Electrons generated by such laser pulses have energies in the range of several MeV. The stopping distance of such energetic electrons in the DT plasma greatly exceeds the optimal for ignition<sup>11</sup>  $\rho R = 0.3$  to 1.2, thus increasing the energy required for ignition. The simulations show that the energy of fast electrons, the stopping distance, and the minimum energy for ignition can be reduced using frequency-doubled laser pulses since the mean energy of fast electrons is proportional to the laser wavelength. This conclusion is in agreement with earlier results by Atzeni *et al.*<sup>14</sup> and Honrubia *et al.*,<sup>15</sup> where the ponderomotive scaling was used to estimate the fast-electron energy.

In this article, the gain of cone-in-shell targets is also estimated through two-dimensional simulations. Gold cones were suggested as a way to keep a plasma-free path for the fast-ignitor pulses and deliver the petawatt pulse energy to the fuel core. While improving the energy transport to the hot spot, cone-focus geometries can complicate the implosion. A simple model of cone-in-shell targets is considered here, where the shell is imploding along a fixed-boundary “rigid” cone with a truncated tip. After the shell departs from the cone tip, the high-pressure shell plasma is free to expand into the hole left by the cone. This last phase of the implosion is simulated with the two-dimensional hydrocode *DRACO*,<sup>16</sup> which is also used to simulate the ignition and burn phases. This is a highly simplified model of cone-in-shell target implosions, and the resulting gains should be viewed as an optimistic estimate. The simulations show that, in spite of the fact that the shell integrity is not preserved and the density profile is modified facing the cone, the minimum energy for ignition (using monoenergetic

electron beams) is only weakly increased by 3 to 4 kJ, while the target gain is reduced by only 20% to 30%.

The following sections (1) present a summary of the high-density and high- $\rho R$  target design recently developed for fast ignition; (2) describes the simulations of ignition and burn using monoenergetic (and Maxwellian) electron beams with prescribed parameters and calculation of the gain curve; (3) discuss the effects of a fast-electron Maxwellian distribution, ponderomotive temperature scaling, and Gaussian laser pulses; and (4) present and discuss the results from simulations of pseudo-cone targets.

### Review of the Target Designs and Gain Formula

We follow the work of Ref. 5 with regard to the optimization of the target designs for fast ignition. The optimal fuel assembly for fast ignition<sup>5</sup> requires a small-size, low-temperature hot spot surrounded by a massive cold shell of densities in the 300- to 500-g/cm<sup>3</sup> range. A small and relatively cold hot spot is preferred in that most of the driver energy is used to compress the fuel assembly rather than heating the hot spot. The optimum density for ignition is determined based on considerations concerning the fast-electron energy required for ignition and the fast-electron beam radius. It follows from Atzeni's work<sup>11</sup> that the minimum energy for ignition using a monoenergetic electron beam can be approximated by  $E_{\text{ig}}^{\text{min}} = 11[400/\rho(\text{g/cm}^3)]^{1.85}$  and the optimum beam radius by  $r_b^{\text{opt}} = 16[400/\rho(\text{g/cm}^3)]^{0.97}$ , where  $\rho$  is the density of the precompressed DT fuel. While lower ignition energies are needed for greater fuel densities, they require a more-focused electron beam. A reference density of 300 g/cm<sup>3</sup> is often used in the literature, for which a reasonable-sized electron beam of about 20- $\mu\text{m}$  radius requires about 20 kJ of electron energy for ignition. Since technological limitations make it difficult to achieve electron-beam radii shorter than 15 to 20  $\mu\text{m}$ , a fuel density of 300 to 500 g/cm<sup>3</sup> can be a reasonable compromise to keep the ignition energy relatively low without imposing severe requirements on the  $e$ -beam focus.

In Ref. 5, relations between the in-flight and stagnation hydrodynamic variables of the imploded shells are derived and used to design optimized fast-ignition targets. According to these relations, the maximum density at stagnation scales as  $\rho_{\text{max}} \sim V_i/\alpha$  and the maximum areal density scales as  $\rho R \sim E_c^{0.33}/\alpha^{0.57}$ , where  $V_i$  is the implosion velocity at the end of the acceleration phase and  $\alpha$  is the value of the in-flight adiabat at the inner shell surface. Here the adiabat is defined as the ratio of the plasma pressure to the Fermi pressure of a degenerate electron gas. For a DT plasma, the adiabat can be

approximated by  $\alpha \approx p(\text{Mbar})/2.2\rho(\text{g/cm}^3)^{5/3}$ . The aspect ratio at stagnation, defined as the ratio of the hot-spot radius to the shell thickness  $A_s = R_h/\Delta_s$ , scales as  $A_s \sim V_i$ . Simple formulas for the target gain and the maximum in-flight aspect ratio (IFAR) are also obtained, according to which  $G_M \sim V_i^{-1.25}\theta$  and  $\text{IFAR} \sim V_i^2/\langle\alpha\rangle^{0.6}$ , where  $\langle\alpha\rangle$  is the average in-flight adiabat and the common expression for the burn fraction  $\theta \approx (1 + 7/\rho R)^{-1}$  can be used. The energy gain decreases with the implosion velocity and increases with  $\rho R$ . For a given driver energy on target, lower implosion velocities require more massive targets, and therefore more fuel available for reactions. Higher  $\rho R$ 's lead to longer confinement time and therefore higher burn fractions. Thus low implosion velocities (i.e., massive targets) and low adiabats (i.e., high  $\rho R$ ) are necessary to achieve high gains. A low implosion velocity also decreases the IFAR, reducing the growth rate of the most-dangerous Rayleigh–Taylor instability modes. The latter are the Rayleigh–Taylor modes with a wave number  $k$  such that  $k\Delta_{\text{if}} \approx 1$ , where  $\Delta_{\text{if}}$  represents the in-flight thickness. Furthermore, with a low implosion velocity, the stagnation aspect ratio, and, consequently, the size and energy of the hot spot, decreases.

The scaling law for the maximum density at stagnation suggests that the minimum implosion velocity is set by the adiabat and the density required for ignition. Thus, high-gain fast-ignition implosions require low values of the inner-surface in-flight adiabat. As long as the ratio  $V_i/\alpha \sim \rho$  is sufficiently large to achieve the densities required for fast ignition, the implosion velocity can be minimized by driving the shell on the lowest-possible adiabat. However, very low adiabat implosions require long pulse lengths and careful pulse shaping. The long pulse length is due to the slow velocity of the low-adiabat shocks, and the careful shaping is required to prevent spurious shocks from changing the desired adiabat. Furthermore the ratio between the peak power and the power in the foot of the laser pulse (i.e., the power contrast ratio) increases as the adiabat decreases, thus leading to difficult technical issues in calibrating the pulse shape. These constraints on the pulse shape are alleviated by using the relaxation laser-pulse technique.<sup>17</sup> As suggested in Ref. 5, reasonable minimum values of the inner surface adiabat and implosion velocity are  $\alpha \approx 0.7$  and  $V_i \sim 1.7 \times 10^7$  cm/s, corresponding to an average density of about 400 g/cm<sup>3</sup>. An adiabat below unity implies that at shock breakout, the inner portion of the shell is not fully ionized. Reference 5 also shows that a very modest IFAR  $\approx 16$  corresponds to such implosion velocity and adiabat. Since the number of  $e$  foldings for the growth of the most-dangerous Rayleigh–Taylor instability modes with wave number  $k \approx 1/\Delta_{\text{if}}$  is approximately  $0.9\sqrt{\text{IFAR}} \approx 3.6$ , one concludes that the implosion of such capsules is approximately

one dimensional. This is an important consideration since it allows us to make use of the one-dimensional code *LILAC*<sup>18</sup> to simulate the generation of the dense core of the fast-ignition fuel assembly (in the absence of a cone).

It is important to emphasize that the peak values of the density and total areal density occur at different times. As the shell stagnates, the density and areal density grow as a result of the plasma compression induced by the return shock traveling outward from the center. The peak density occurs before the time of peak areal density. Furthermore, a significant amount of relatively low density ( $\rho < 200 \text{ g/cm}^3$ ), unshocked free-falling plasma surrounds the dense core at the time of peak  $\rho R$ . Such a low-density plasma carries a significant fraction of the areal density ( $\sim 25\%$ ), thus preventing the fast particles from fully penetrating the dense core. Hence, it can be beneficial to launch the igniter beam soon after the time of peak  $\rho R$  when the return shock has propagated farther out and compressed the low-density region. One-dimensional simulations of the implosions indicate that at such a time, the average density of the compressed core is about half its peak value.

Using low-velocity implosions of massive shells for fast-ignition fuel assembly should also improve the performance of cone-in-shell targets where a gold cone is inserted into the shell to keep a plasma-free path for the fast-ignitor pulse.<sup>2,3</sup> Recent experiments and simulations of cone-in-shell target implosions<sup>19</sup> have shown that the integrity of the cone tip is compromised by the large hydrodynamic pressures and that a low-density plasma region develops between the cone tip and the dense core, thus complicating the fast-electron transport. Since the stagnation pressure scales as  $\rho \sim V_i^{1.8}$  (Ref. 20), the fuel assemblies from low-velocity implosions can improve the cone target's performance since the resulting dense core has relatively low pressure (due to the low velocity), thus reducing the hydrodynamic forces on the cone tip. Furthermore, since low velocities are obtained by imploding shells with large masses, the resulting core size is large, thus reducing the distance between the tip and the dense core edge.

While the simulations in Ref. 5 consider only implosions driven by a compression laser pulse with a wavelength  $\lambda = 0.35 \text{ } \mu\text{m}$ , the wavelength dependence for the stagnation variables is included analytically into the gain formula. After setting the values of the adiabat  $\alpha \approx 0.7$  and implosion velocity  $V_i \sim 1.7 \times 10^7 \text{ cm/s}$ , the maximum gain becomes a function of the compression laser energy and wavelength (see Ref. 10):

$$G_M \approx \frac{743 I_{15}^{-0.09} (0.35/\lambda_L)^{0.66} (1 - E_{\text{cut}}/E_c)^\mu}{1 + 21 (\lambda_L/0.35)^{0.25} / [\xi E_c^{0.33}]}, \quad (2)$$

where  $E_c$  is in kilojoules and a weak analytical dependence on the maximum pulse intensity  $I_{15} \sim 1$  (in units of  $10^{15} \text{ W/cm}^2$ ) is included. This expression uses fitting parameters  $\mu$  and  $\xi$ , which need to be determined by comparison with ignition and burn simulations. Here  $\xi$  represents the fraction of the maximum total areal density available for the burn to be used in  $\theta(\rho R)[\rho R = \xi(\rho R)_{\text{max}}]$ . The *ad hoc* term  $(1 - E_{\text{cut}}/E_c)^\mu$  has been introduced to account for the yield deterioration of small targets where the burn temperature is below 30 keV and the electron-beam size is of the order of the compressed core size occurring for  $E_c \sim E_{\text{cut}} \approx 40 \text{ kJ}$ . The factors  $\mu$  and  $\xi$  are of order unity and are to be determined by a numerical fit to the gain in the ignition and burn simulations reported in the next section.

### Simulation of Ignition and Burn by Monoenergetic and Maxwellian Electron Beams

To simulate the burn phase of the fast-ignited capsules, we start from the one-dimensional fuel assembly obtained from the code *LILAC* and simulate the ignition by a collimated electron beam and subsequent burn with the two-dimensional, two-fluid hydrocode *DRACO*.<sup>16</sup> The latter has been recently modified<sup>21</sup> to include the electron-beam-energy deposition into the dense fuel. The effects of electron-beam instabilities such as Weibel and resistive filamentation are not included in this work. An overview of the physics issues related to fast-electron generation and transport problem in fast ignition can be found in Refs. 6 and 22. Here a simple straight-line transport model for fast electrons is chosen, in which fast electrons lose energy due to collisions with thermal electrons and to collective plasma oscillations. We use the slowing-down theory of Ref. 13 that includes the effect of multiple scattering. The value of the Coulomb logarithm in the stopping-power term of Ref. 13 has been modified to account for quantum effects. Burn simulations of several fuel assemblies have been performed, characterized by the implosion parameters mentioned above. The targets used in the simulations (Fig. 110.12 shows three of them) are massive wetted-foam targets with an initial aspect ratio of about 2 (outer radius/thickness) driven by UV laser energies varying from 50 kJ to 2 MJ and  $I_{15} \simeq 1$ . The relaxation-type<sup>17</sup> laser pulses are shown in Fig. 110.13 with the main pulse length varying from 11.5 ns for the 100-kJ target to 22 ns for the 750-kJ target. In all cases, the fast electrons are injected at about 50  $\mu\text{m}$  from the dense core and close to the time of peak areal density.

The main properties of the ignition and burn propagation are illustrated below for a particular example of the 300-kJ fuel assembly. Figure 110.14 shows the target radial density profiles at consecutive moments of time close to the time of maximum areal density. During this period of time, the target expands and the maximum density drops from about  $700 \text{ g/cm}^3$  to  $300 \text{ g/cm}^3$ . The dense part of the core is surrounded by a relatively low density unshocked region. As the return shock propagates outward, more fuel gets compressed, thus increasing the total  $\rho R$  available for the burn. Figure 110.15 shows the density (a) as a function of the areal density and (b) as a function of the volume. The areal density of the dense region varies between  $1.1$  to  $1.3 \text{ g/cm}^2$ , while the

$\rho R$  in the unshocked region decreases from  $0.6$  to  $0.28 \text{ g/cm}^2$  with time. The hot-spot volume [Fig. 110.15(b)] is less than 8% of the compressed volume.

Figure 110.16 shows snapshots of ignition and burn simulations for the 300-kJ fuel assembly. Ignition is triggered by a 2-MeV monoenergetic electron beam with a radius of  $20 \mu\text{m}$  and duration of 10 ps. The cylindrically symmetric, radially uniform electron beam is injected from the right. The beam's temporal distribution is also uniform. Ignition is triggered first in a small plasma volume heated by the electrons [Figs. 110.16(a) and 110.16(b)]; the thermonuclear burn wave then propagates to the remaining fuel [Figs. 110.16(c)–110.16(f)].

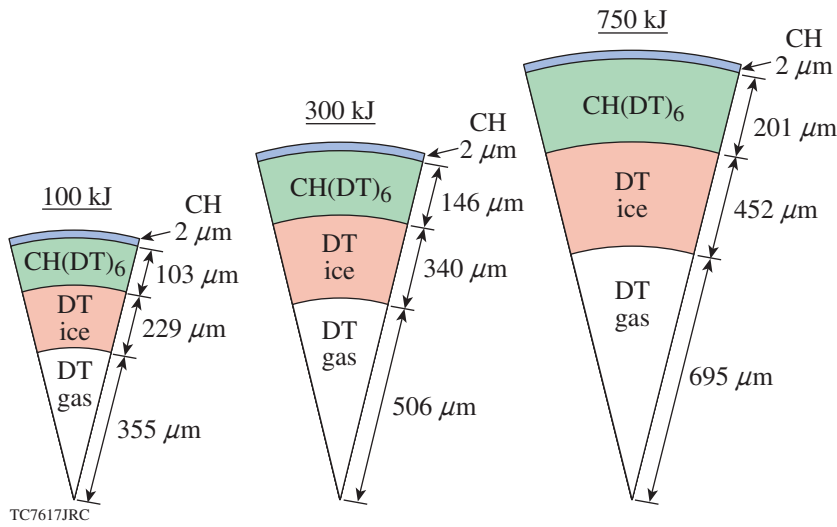


Figure 110.12  
100-, 300-, and 750-kJ targets for optimized fast-ignition fuel assembly.

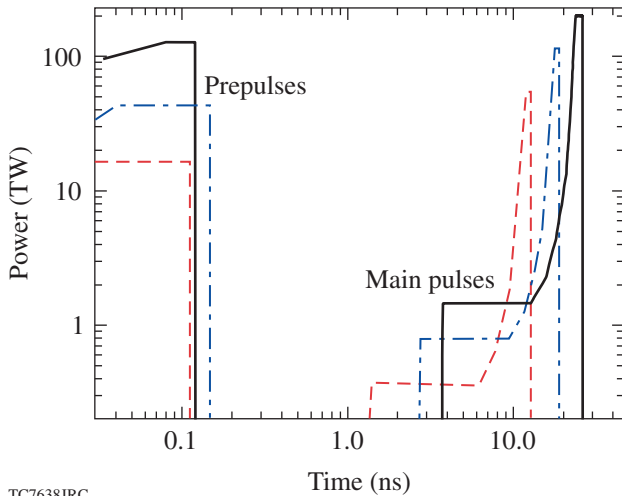


Figure 110.13  
Laser pulses (power versus time) for the 100-kJ (dashed lines), 300-kJ (dashed-dotted lines), and 750-kJ (solid lines) targets.

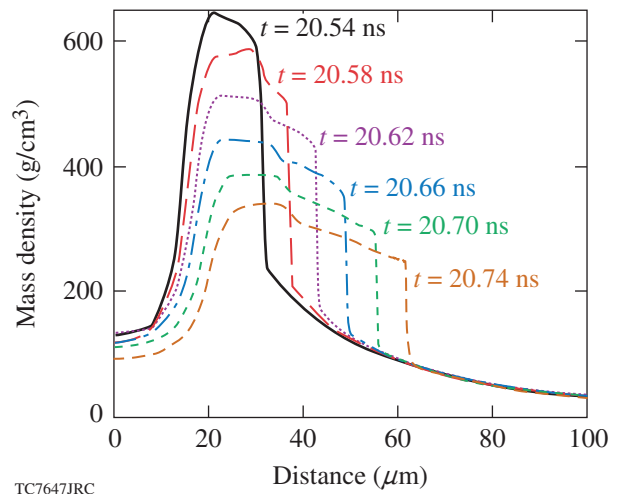
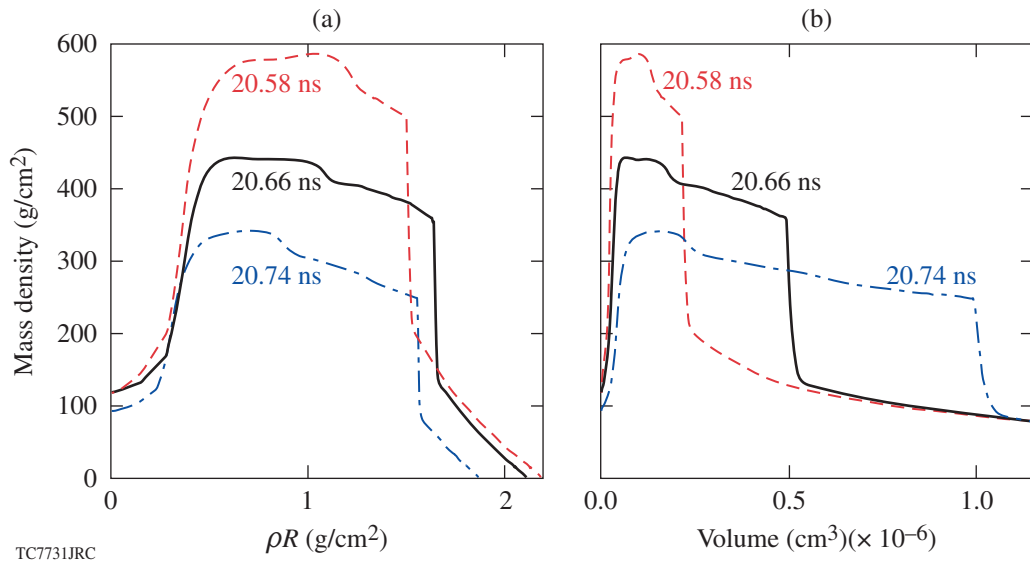
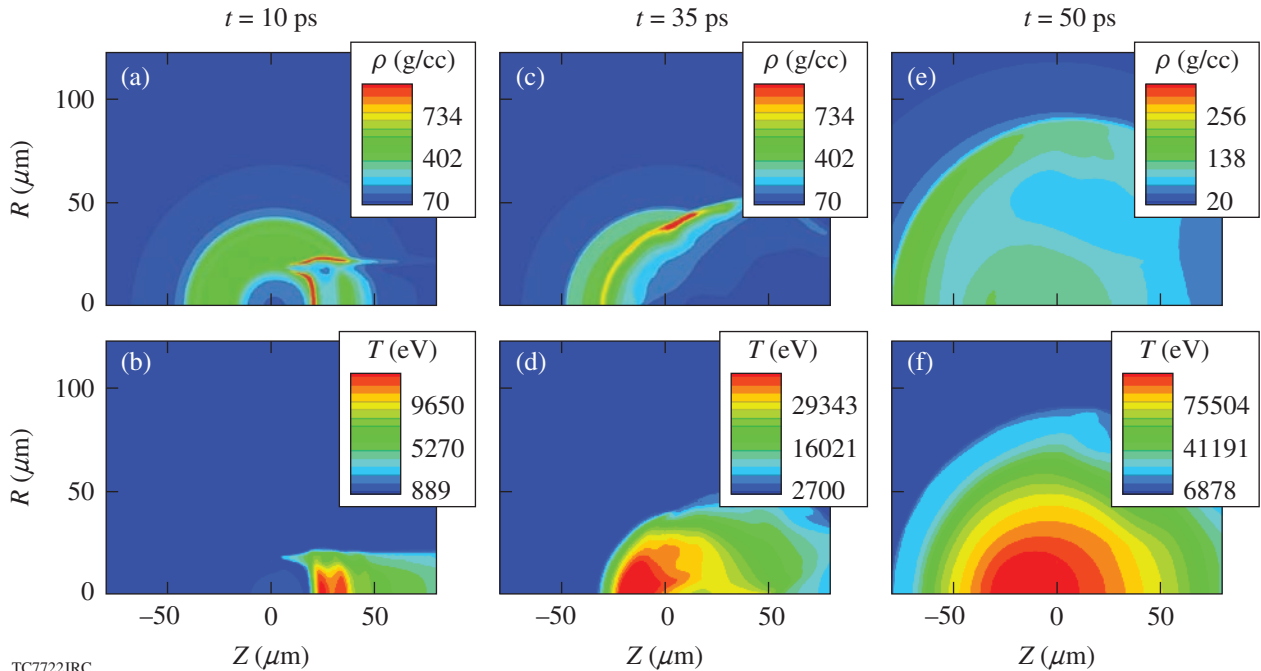


Figure 110.14  
Density profiles of the 300-kJ target at different times (about the time of peak  $\rho R$ ) when the fast electrons are injected in the simulations of Fig. 110.17.



TC7731JRC

Figure 110.15  
Density profiles of the 300-kJ target versus (a) areal density and (b) volume at three times near the time of peak  $\rho R$ .



TC7722JRC

Figure 110.16  
Contour plots of the density ( $\rho$ ) and ion temperature ( $T$ ) at selected moments of time in the burn simulation induced by ignition by an 18-kJ, 10-ps, 2-MeV monoenergetic electron beam.

We have performed simulations using monoenergetic electron beams to find how the minimum energy for ignition depends on the electron-beam parameters and the injection time. The results for the 300-kJ fuel assembly are shown below. Figure 110.17 shows the dependence of the minimum ignition energy for a 10-ps, 2-MeV monoenergetic electron beam on the beam injection time for three beam radii: 20, 30, and 40  $\mu\text{m}$ . The minimum ignition energy is found with an error  $\leq 4\%$  by changing the total electron-beam energy while keeping all the other parameters constant. For a 20- $\mu\text{m}$  electron beam, minimum ignition energy of about 15 kJ is found when the density is maximum for earlier injection times. It increases for late injections when the target density decreases. While focused beams with a radius  $\leq 20 \mu\text{m}$  are preferable for ignition, realistic electron beams may have a larger spot size when entering the fuel core because of their angular spread. For a 30- $\mu\text{m}$  electron beam, the ignition energy reaches its minimum of 26 kJ at the injection time of  $t = 20.58 \text{ ns}$  and for a 40- $\mu\text{m}$  beam the minimum ignition energy is 41 kJ at  $t = 20.62 \text{ ns}$ .

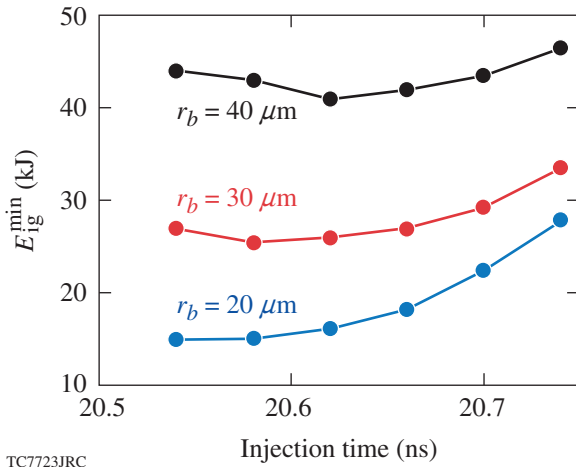


Figure 110.17  
Minimum ignition energy versus injection time for a 10-ps, 2-MeV monoenergetic electron beam and three values of the beam radius: 20, 30, and 40  $\mu\text{m}$ .

The minimum energy for ignition found in our simulations is in good agreement with that found by Atzeni.<sup>11</sup> According to Atzeni's formula, the minimum ignition energy of 19.7 kJ is reached for a density of  $300 \text{ g/cm}^3$  and a beam radius of 20  $\mu\text{m}$ . Our simulations predict a minimum ignition energy of about 25 kJ for the same beam radius and injection when the density has a similar value in the dense region. The 25% difference in the ignition energy between our simulations and

Atzeni's formula can be attributed to the loss of fast electrons in the low-density unshocked region. Notice that the electron-pulse duration in our simulation is less than the hydrodynamic confinement time of the heated region as required by Atzeni.

Figure 110.18(a) shows the dependence of the minimum ignition energy on the beam radius for a pulse duration of 10 ps and injection time of 20.62 ns. Figure 110.18(b) shows how the minimum ignition energy depends on the electron-pulse duration for a fixed radius of 20  $\mu\text{m}$  and the same injection time. The minimum ignition energy increases with both the electron-beam radius and pulse duration.

Figure 110.19 shows the dependence of the minimum ignition energy on the electron energy. The beam radius is 20  $\mu\text{m}$ , the pulse duration is 10 ps, and the injection time is 20.62 ns.

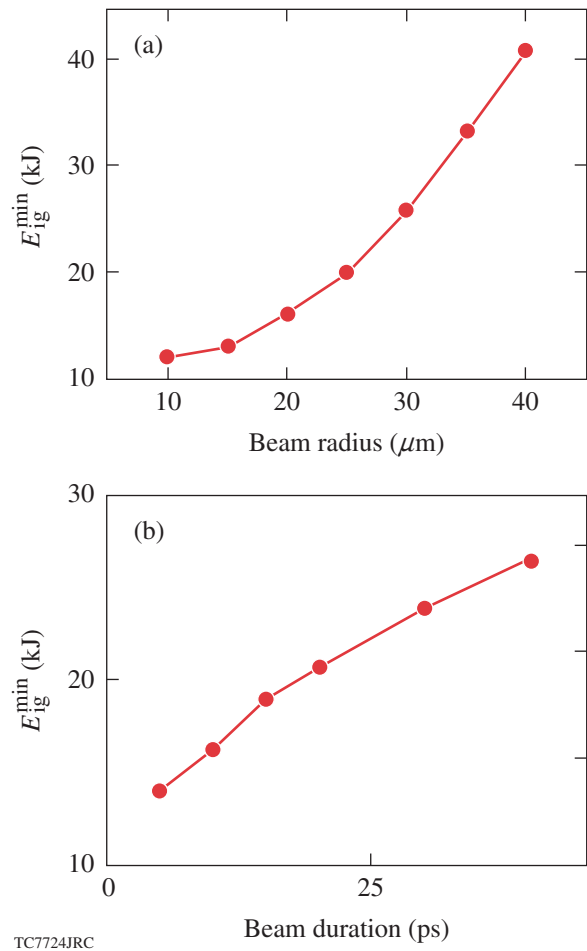
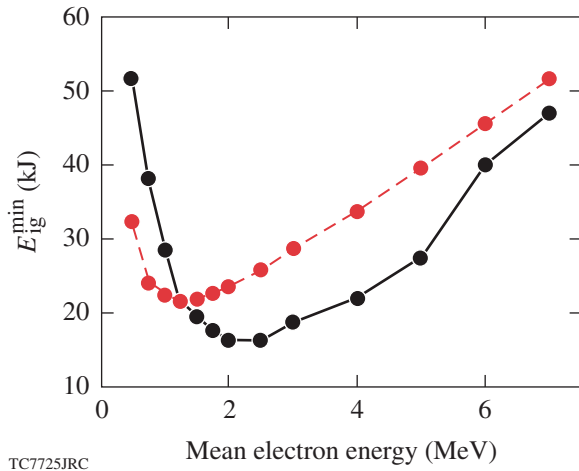


Figure 110.18  
Minimum ignition energy versus (a) beam radius and (b) duration for a 2-MeV monoenergetic electron beam. (a) The beam duration is 10 ps and (b) the beam radius is 20  $\mu\text{m}$ .

The results for monoenergetic electrons (solid line) and electrons with an energy spread (dashed line) are shown. In the simulations with an energy spread, a relativistic Maxwellian electron distribution function is used. For monoenergetic electrons, the lowest ignition energy of 16.25 kJ is reached at 2 MeV, while for Maxwellian electrons, 21.5 kJ for the mean energy of 1.25 MeV is reached. The minimum ignition energy is higher for Maxwellian electrons because the energy is deposited over a larger region in the longitudinal direction and is not as localized as for monoenergetic electrons. This is seen from the snapshots for the plasma temperature just after the energy is deposited by fast electrons ( $t = 10$  ps) in the simulations with 2-MeV Maxwellian (Fig. 110.20) and monoenergetic electrons (Fig. 110.16). Maxwellian electrons with  $E > \langle E \rangle$  transfer more energy than electrons with  $E < \langle E \rangle$ . This explains why the mean electron energy that minimizes the ignition energy is lower for Maxwellian than for monoenergetic electrons. Figure 110.19 also shows that the minimum ignition energy greatly increases for high-energy multi-MeV electrons. This is because the stopping length of such electrons greatly exceeds the optimal size of the heated region<sup>11</sup>  $0.3 < \rho R < 1.2 \text{ g/cm}^2$ , so that a much longer region is heated. Unfortunately, this appears to be the case of realistic laser pulses (see **Simulation of Ignition by Maxwellian Electrons with Ponderomotive Temperature Scaling and Gaussian Laser Pulses**, p. 82).

Our simulations for different targets show that, for a 20- $\mu\text{m}$  beam radius, the minimum energy required for ignition is consistently  $\approx 15$  kJ using electron beams with a 20- $\mu\text{m}$  radius.



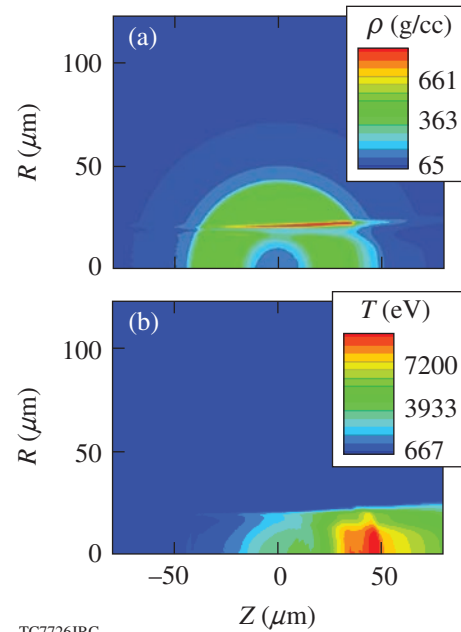
TC7725JRC

Figure 110.19 Minimum ignition energy versus electron energy for 2-MeV monoenergetic (solid line) and Maxwellian (dashed line) electron beams. The beam duration is 10 ps and the radius is 20  $\mu\text{m}$ .

As long as the ignition is triggered, the thermonuclear energy yield is approximately independent of the electron-beam characteristics. The neutron yields for the 100-, 300-, and 750-kJ assemblies are  $2.0 \times 10^{18}$ ,  $1.2 \times 10^{19}$ , and  $4.2 \times 10^{19}$ , and the thermonuclear energy yields are 5.6, 34, and 118 MJ, respectively. The results of these simulations are used to determine the fitting parameters  $\xi \approx 0.7$  and  $\mu \approx 1.1$  in Eq. (2), leading to the following maximum gain formula:

$$G_M = \frac{743 I_{15}^{-0.09} (0.35/\lambda_L)^{0.66} (1 - E_{\text{cut}}/E_c)^{1.1}}{1 + 30(\lambda_L/0.35)^{0.25}/E_c^{0.33}}, \quad (3)$$

where  $E_c$  is in kilojoules and  $E_{\text{cut}} \approx 40$  kJ. Notice that even a modest-sized UV laser driver with an energy of 100 kJ can produce a fuel assembly yielding a maximum gain close to 60. Figure 110.21 shows that Eq. (3) accurately fits all simulation results and can be used to determine the total gain in Eq. (1). Figure 110.22 shows the total gain for three values of the ignition-pulse energy  $E_{\text{PW}} = 50$  kJ, 75 kJ, and 150 kJ. Even in the case of  $E_{\text{PW}} = 150$  kJ, the target gain from a 100-kJ fuel assembly is still remarkably high ( $G_T \approx 22$ ).



TC7726JRC

Figure 110.20 Contour plots of the density and ion temperature after the 300-kJ target is heated by a 25-kJ, 10-ps, 20- $\mu\text{m}$ , 2-MeV Maxwellian electron beam.

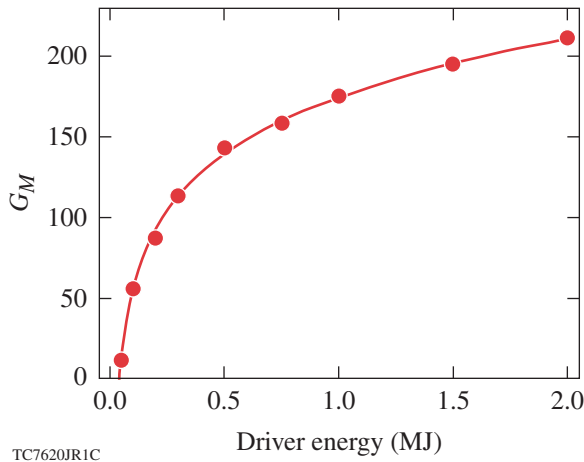


Figure 110.21  
Maximum gain (energy yield/compression driver energy) versus compression driver energy from Eq. (3) (curve) and *DRACO* simulations (dots).

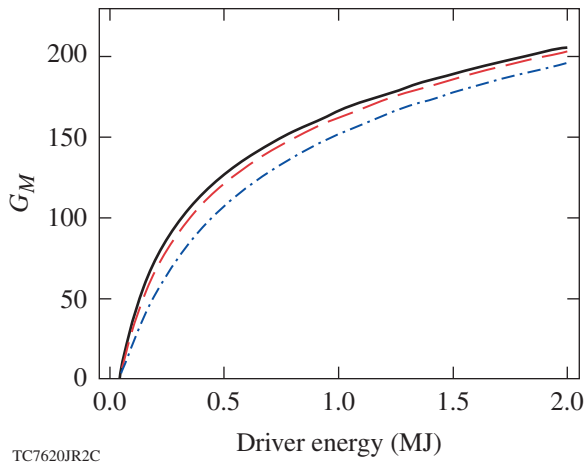


Figure 110.22  
Target gain (energy yield/total energy on target) versus compression driver energy for  $E_{PW} = 50$  kJ (solid line), 75 kJ (dashed line), and 150 kJ (dashed-dotted line).

### Simulation of Ignition by Maxwellian Electrons with Ponderomotive Temperature Scaling and Gaussian Laser Pulses

Hot electrons in fast ignition are produced during the interaction of ultra-intense laser pulses with either the coronal plasma or a solid target. The spectrum of fast electrons and the energy conversion efficiency from the laser to electrons generally depend on the details of this interaction. An assumption, however, is often used<sup>14,15,23</sup> that the mean energy of hot electrons equals the energy of their oscillation in the laser field  $E \sim mc^2(\gamma-1)$  (so-called ponderomotive scaling<sup>9</sup>), where

$\gamma = \sqrt{1+p^2/2}$ ,  $p \sim eA/mc^2$  is the momentum of electrons (normalized to  $mc$ ) in the linearly polarized laser field with the amplitude of the vector potential  $A$ . The experimental data predict different values of the energy conversion efficiency from the laser to electrons in the range  $\eta \sim 0.2$  to  $0.5$  for laser intensities  $I > 10^{19}$  W/cm<sup>2</sup> (Refs. 2 and 24). We have performed simulations assuming a Gaussian temporal profile for the laser pulse and a relativistic Maxwellian distribution function for fast electrons with a mean energy following the ponderomotive scaling that can also be rewritten as

$$\langle E \rangle \approx \left[ \frac{I(\lambda/1.054 \mu\text{m})^2}{10^{19} \text{ W/cm}^2} \right]^{1/2} \text{ MeV.} \quad (4)$$

According to this scaling, the mean energy is a function of the laser intensity and the wavelength. Notice that for a relativistic Maxwellian distribution function of the form  $f(E) \sim \exp[-mc^2(\gamma-1)/kT](\gamma^2-1)^{1/2}\gamma$ , the mean energy is  $\langle E \rangle = 3kT/2$  in the nonrelativistic and  $\langle E \rangle = 3kT$  in the ultra-relativistic limit. Two values of the energy conversion efficiency to fast electrons were used:  $\eta = 0.3$  and  $\eta = 0.5$ . Simulations with different parameters of the laser pulse such as spot size (rectangular beam profile in the radial direction), duration, and wavelengths of  $1.054 \mu\text{m}$  and  $0.527 \mu\text{m}$  were performed for the 300-kJ fuel assembly to find the minimum energy required for ignition. The optimal injection time is found to be close to  $t = 20.62$  ns when the averaged density is about  $450 \text{ g/cm}^3$ . Using a smaller beam radius and pulse duration lead to higher intensities and more-energetic electrons, according to the ponderomotive scaling Eq. (4). However, very energetic (multi-MeV) electrons require a large stopping distance that can even exceed the size of small-to-moderate energy targets. Larger beam radii with  $\rho r_b > 0.6 \text{ g/cm}^2$  lead to a heated volume greater than the optimal value.<sup>11</sup> Also very long laser pulses with durations exceeding the confinement time of the heated region are detrimental and lead to a higher ignition energy. Optimal values of the duration and radius exist for which the laser ignition energy is minimized.

A set of simulations was performed to find such conditions. Tables 110.I and 110.II summarize the results. The optimal laser pulse duration and radius, the mean hot-electron energy (at the time of the Gaussian peak), the electron-beam fuel coupling efficiency, and the minimum ignition energy (of the laser pulse and the electron beam) are provided from simulations carried out with two values of the coupling efficiency and two laser wavelengths ( $\lambda = 1.054 \mu\text{m}$  and  $0.527 \mu\text{m}$ ). The minimum laser energy for ignition is 235 kJ (with 71 kJ in fast electrons) for

Table 110.I: Summary of the simulations for  $\lambda = 1.054 \mu\text{m}$ .

$\eta$	$r_b$ ( $\mu\text{m}$ )	$\tau_b$ (ps)	$E_{\text{las.ig}}^{\text{min}}$ (kJ)	$E_{\text{e.ig}}^{\text{min}}$ (kJ)	$\langle E \rangle$ (MeV)	$\eta_{e\text{-pl}}$
0.3	26.3	16.3	235	71	7.7	0.69
0.5	22.5	13.8	105	53	6.3	0.76

 Table 110.II: Summary of the simulations for  $\lambda = 0.527 \mu\text{m}$ .

$\eta$	$r_b$ ( $\mu\text{m}$ )	$\tau_b$ (ps)	$E_{\text{las.ig}}^{\text{min}}$ (kJ)	$E_{\text{e.ig}}^{\text{min}}$ (kJ)	$\langle E \rangle$ (MeV)	$\eta_{e\text{-pl}}$
0.3	19	8	106	32	3.7	0.86
0.5	16.8	7	50	25	3.2	0.92

wavelength  $\lambda = 1.054 \mu\text{m}$  and conversion efficiency  $\eta = 0.3$  (Table 110.I). Figure 110.23 shows snapshots of the plasma density and ion temperature for this simulation at two moments of time: at the end of the laser pulse and at the developed burn stage. Figure 110.23(b) shows that the plasma is heated throughout the core. Electrons are not completely stopped in the core and continue to heat the low-density plasma behind it. Ignition is triggered first in the plasma column heated by the electrons and the burn region then expands radially [Figs. 110.23(c) and 110.23(d)]. The laser intensity at the time of the Gaussian peak is  $6.5 \times 10^{20} \text{ W/cm}^2$ , and very energetic electrons are

produced with a mean energy of 7.7 MeV (Table 110.I). Only 69% of the total electron energy is deposited into the plasma. Table 110.I also shows that the laser energy required for ignition decreases to 105 kJ (53 kJ in fast electrons) for  $\eta = 0.5$ . This significant reduction in the ignition energy is due not only to a larger fraction of the laser energy converted into hot electrons but also to the lower electron energies produced with reduced intensities.

It was suggested by Atzeni and Tabak<sup>14</sup> that shorter laser wavelengths can reduce the mean energy of fast electrons [see Eq. (4)], their stopping length, and the energy required for ignition. Indeed, Table 110.II shows that for a frequency-doubled green light ( $\lambda = 0.527 \mu\text{m}$ ), the laser energy required for ignition decreases to 106 kJ (32 kJ in fast electrons) for  $\eta = 0.3$  and 50 kJ (25 kJ in fast electrons) for  $\eta = 0.5$ . The mean hot-electron energy, however, is still high in these simulations (3.7 MeV and 3.2 MeV, respectively), which suggests that even shorter laser wavelengths can be desirable.

While simulations predict that using a green laser light reduces the energy required for ignition, frequency doubling of the red light with high conversion efficiency can present a technologically challenging task. In this context, finding other mechanisms to reduce the energy of hot electrons generated by ultra-intense laser pulses would be very helpful.

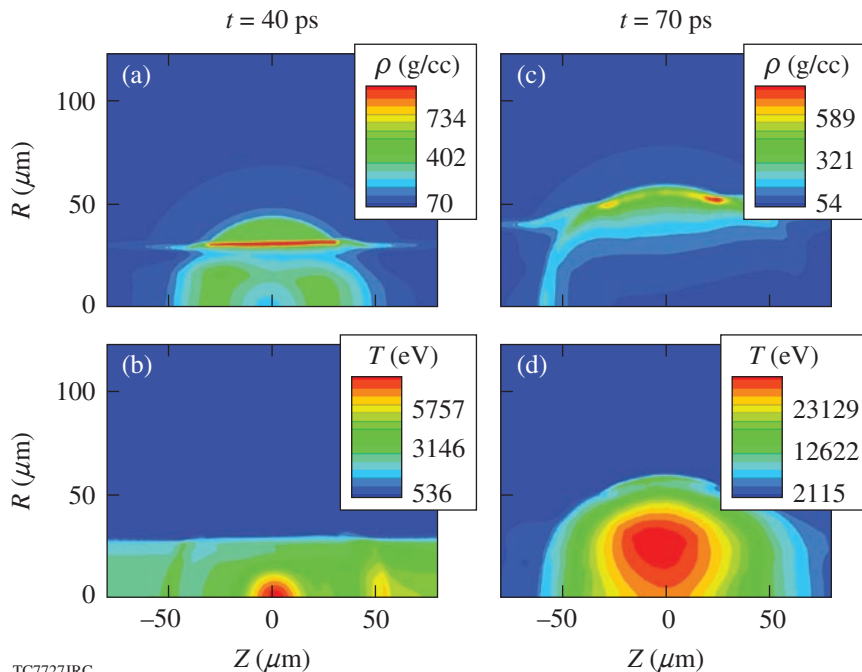


Figure 110.23

Contour plots of the density and ion temperature at selected moments of time in the burn simulation induced by a 235-kJ, 26.3- $\mu\text{m}$ , 16.3-ps laser pulse with an energy conversion efficiency to fast electrons of  $\eta = 0.3$ .

TC7727JRC

### Simulations of Pseudo-Cone Targets

The use of gold cones is currently considered as one of the most promising options to deliver the petawatt-pulse laser energy to the compressed fuel. The cone provides an access path for an ignition laser beam to the fuel, free of the coronal plasma that otherwise can reflect the laser light at the critical plasma surface 1 to 2 mm away from the compressed core. Fast electrons are produced by the interaction of the laser beam with the cone tip located tens to a few hundred microns from target center and then transported toward the core. Cone-focus geometries, while improving the transport of energy to the hot spot, can complicate the implosion. The question arises whether the fuel can still be compressed to the same high densities and areal densities as for spherically symmetric implosions. The compressed core should be significantly modified from the side of the cone where the laser-generated fast electrons enter the core to ignite it. It is important to determine how the minimum energy for ignition and the target gain are affected by the cone.

We have performed simulations of cone-target implosions using a highly simplified model of the cone. We assume that the cone walls are rigid and truncated at a given distance from the center. The pseudo-cone target is schematically shown in Fig. 110.24. The cone walls are directed toward the center of the target and truncated at a distance of about  $200\ \mu\text{m}$  from it. The cone opening angle is  $90^\circ$ . A narrow cone tip may exist and go farther toward the center. We use 1-D *LILAC* implo-

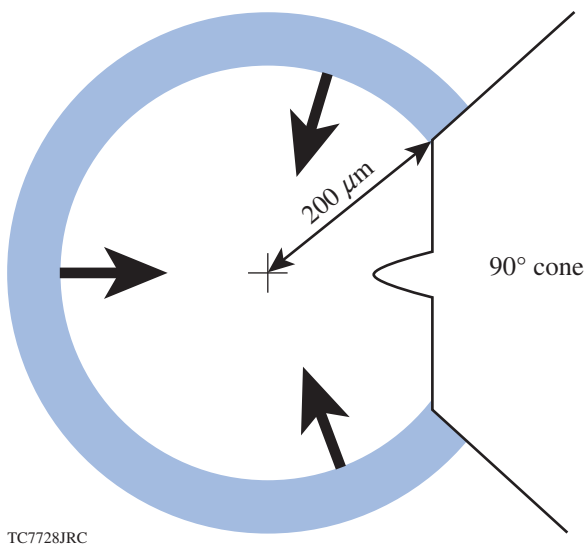


Figure 110.24  
Pseudo-cone target.

sion simulations until the converging shell reaches the cone tip. From this point on, the simulation is continued with the 2-D *DRACO* code. The 1-D *LILAC* outputs are used as initial conditions (time  $t = 0$ ) after removing the section of the shell corresponding to the cone tip. Such a model accounts only for the effect associated with the hole left in the shell after its departure from the cone. Other effects such as shear flow down the sides of the cone and DT contamination by the gold<sup>19,25</sup> or more-complicated cone shapes are not considered here and will be addressed in future work.

We first study how the perturbed shell converges. Figure 110.25 shows snapshots of the fuel density in the *DRACO* simulation for the 300-kJ fuel assembly. The 2-D simulation starts from the spherically symmetric shell with the hole caused by the cone. When the shell approaches the center, the hole does not close and the hot gas flows out from the central region. Figure 110.25(c) shows the density profile at the moment of time ( $t = 0.98\ \text{ns}$ ) when the maximum density is reached in the simulation without the cone, while Fig. 110.25(d) covers the moment of time ( $t = 1.14\ \text{ns}$ ) slightly before the maximum areal density. At  $t = 0.98\ \text{ns}$ , the density profile on the left side of the target is practically the same as in the 1-D simulation (without the cone) and the maximum density is approximately the same. At  $t = 1.14\ \text{ns}$ , the density profile on the left side is still close to that in the 1-D simulation except for the hot spot, which shrinks. The opening in the shell at  $t = 1.14\ \text{ns}$  has a radius of about  $6\ \mu\text{m}$  and is surrounded by a high-density region. While the compressed core is certainly modified by the cone, these changes do not seem to significantly affect the ignition energy requirements. To verify this, we have performed burn simulations using a 2-MeV monoenergetic electron beam with a radius of  $20\ \mu\text{m}$  and a duration of 10 ps, injected at  $t = 1.14\ \text{ns}$  in the  $z$  direction. It is found that the ignition energy increased by only 4 kJ to 19 kJ with respect to the 1-D implosion without the cone. The maximum gain in the pseudo-cone target simulation is equal to 90 instead of 113 without the cone.

Similar pseudo-cone simulations were performed for other targets driven by laser pulses with energies ranging from 50 kJ to 2 MJ. For all of the targets, the minimum ignition energy ranges from 18 to 20 kJ and is found to be only weakly affected by the cone. Figure 110.26 shows the maximum gain in the pseudo-cone target simulations and the gain predicted by Eq. (3). The maximum gain decreases by 20% to 25% for driver pulse energy between 200 kJ and 2000 kJ and slightly more (up to 30%) for lower-energy drivers. Notice that removing a part of the shell in place of the cone in these simulations reduces the total mass of the thermonuclear fuel by approximately 15%;

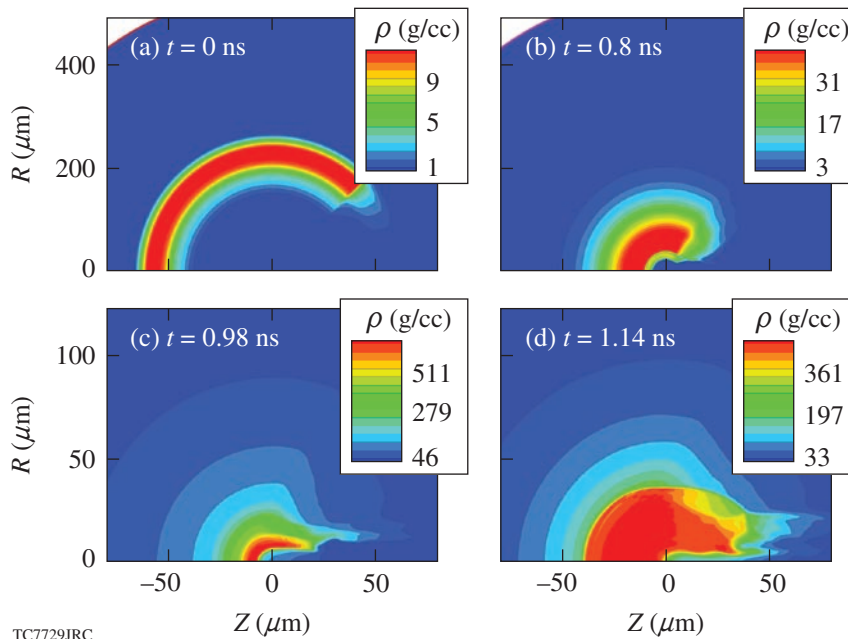
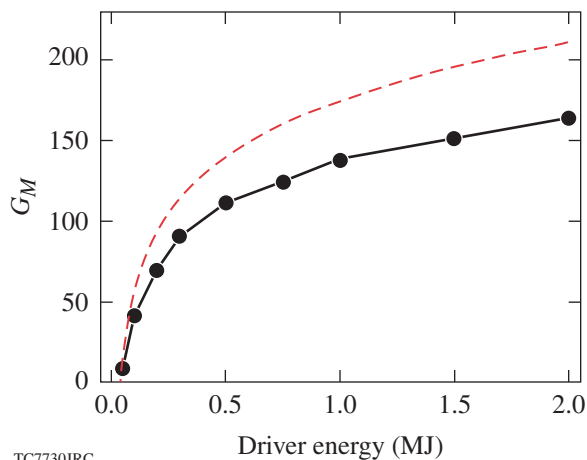


Figure 110.25  
Contour plots of the density at different times in the pseudo-cone-target simulation.

TC7729JRC



TC7730JRC

Figure 110.26  
Maximum gain versus compression driver energy for the pseudo-cone targets (dots connected by a solid line) and for spherically symmetric implosions [Eq. (3)] (dashed line).

however, the maximum gain in the simulation is reduced more than that. This signifies that not all of the remaining fuel can be assembled so effectively as for an unperturbed shell. Nevertheless, the reduced gain in the pseudo-cone target simulations is still remarkably high; in particular, a maximum gain of 70 is still possible with driver-pulse energies of only 200 kJ.

### Summary and Discussion

Hydrodynamic simulations of realistic, high-gain, fast-ignition targets, including one-dimensional simulations of the

implosion and two-dimensional simulations of ignition by a collimated electron beam and burn propagation are presented and discussed in this article. The targets' design is based on the fuel assembly theory of Ref. 5. The fast-ignition targets are massive wetted-foam, cryogenic DT shells with an initial aspect ratio close to 2. They are imploded by relaxation-type pulses to form high-density and high-areal-density cores with small hot spots, which are optimal for fast ignition. Due to the large thickness and small in-flight aspect ratio, such targets are practically unperturbed by Rayleigh–Taylor instability, making 1-D hydrocodes suitable to simulate the implosion.

The simulations of ignition and burn have been used to find the minimum energy for ignition and to generate gain curves for direct-drive, fast-ignition inertial confinement fusion based on realistic fast-ignition target designs. A large number of runs for targets driven by UV-laser compression pulses with energies from 50 kJ to 2 MJ have been performed. Fitting parameters in the analytical scaling for the target gain are obtained, accounting for the fraction of the maximum total areal density available for the burn and yield deterioration of small targets. It is found that even modest-sized UV-laser drivers, with an energy of 100 kJ, can produce a fuel assembly yielding a maximum gain (energy yield/compression driver energy) close to 60. Assuming a 100-kJ ignition laser pulse, the total gain (energy yield/total energy on target) can be as high as 30 for a 100-kJ compression pulse and about 60 for a 200-kJ driver. Notice that at 1 MJ, the total gain of the optimized fast-ignition target  $G_T = 160$  (for a 100-kJ ignition pulse) is considerably higher than the gain of

direct-drive NIF targets,  $G \simeq 50$  (Ref. 26). Although less than earlier heuristic model predictions<sup>4</sup> (which also use different optimizations), Eq. (3) shows that fast ignition can achieve significant gains with relatively small drivers.

In our simulations of ignition and burn, the energy of fast electrons, beam radius (20  $\mu\text{m}$  and larger), and pulse length were varied to find the minimum beam energy for ignition close to 15 kJ for different (25-kJ to 2-MJ driver-pulse energy) fuel assemblies, using monoenergetic electron beams. The dependence of the minimum beam energy for ignition on the electron-beam parameters and injection time has been analyzed in detail. The minimum beam energy for ignition increases up to 20 kJ for electrons with energy spread (relativistic Maxwellian distribution function) and optimal mean energy. Simulations using ponderomotive temperature scaling for fast electrons with the laser intensity and Gaussian (in time) laser pulses have also been performed for the 300-kJ fuel assembly. It is shown that for a laser wavelength of 1.054  $\mu\text{m}$ , the minimum laser pulse energy required for ignition is 235 kJ (with 71 kJ in fast electrons) if the energy conversion efficiency from the laser to fast electrons is 30%. The laser ignition energy decreases to 105 kJ (53 kJ in fast electrons) if the energy conversion efficiency is 50%. Such large laser ignition energies are caused by the high electron energy. Indeed, the hot electrons produced by ultra-intense laser pulses have multi-MeV energies, and their stopping range can greatly exceed the optimal value for fast ignition. A possible solution may be using frequency-doubled ignition pulses, for which the mean energy of fast electrons decreases by a factor of 2 (for the same laser intensity). Simulations for a laser wavelength of 0.527  $\mu\text{m}$  predict a minimum laser pulse energy for ignition of 106 kJ (with 32 kJ in fast electrons) for an energy conversion efficiency of 30% and 50 kJ (25 kJ in fast electrons) for a conversion efficiency of 50%. It has been reported<sup>27</sup> that sharp solid-plasma interface electrons can be produced with energy below the ponderomotive scaling prediction. A strong reduction in energy conversion efficiency to fast electrons, however, simultaneously takes place. Finding mechanisms to reduce the energy of fast electrons without a significant loss of conversion efficiency would be very helpful to avoid a technologically complicated task of resorting to green laser light for high-power lasers.

We have also performed simplified cone-target simulations assuming that the cone walls are rigid and truncated at a certain distance from the center. Such simulations predict a gain deterioration of 20% to 30% and a small increase in the minimum ignition energy with respect to unperturbed targets. More-sophisticated cone models are currently under

implementation in the code *DRACO*<sup>28</sup> and the results from more-realistic cone-in-shell target implosion simulations will be reported in future articles.

#### ACKNOWLEDGMENT

This work was supported by the U.S. Department of Energy under Cooperative Agreement DE-FC02-ER54789 (Fusion Science Center, Office of Inertial Fusion Energy Science) and DE-FC52-92SF19460 (Office of Inertial Confinement Fusion), the University of Rochester, and the New York State Energy Research and Development Authority. The support of DOE does not constitute an endorsement by DOE of the views expressed in this article.

#### REFERENCES

1. M. Tabak *et al.*, Phys. Plasmas **1**, 1626 (1994).
2. R. Kodama *et al.*, Nature **412**, 798 (2001).
3. K. A. Tanaka *et al.*, Phys. Plasmas **10**, 1925 (2003); P. A. Norreys, K. L. Lancaster, C. D. Murphy, H. Habara, S. Karsch, R. J. Clarke, J. Collier, R. Heathcote, C. Hernandez-Gomez, S. Hawkes, D. Neely, M. H. R. Hutchinson, R. G. Evans, M. Borchesi, L. Romagnani, M. Zepf, K. Akli, J. A. King, B. Zhang, R. R. Freeman, A. J. MacKinnon, S. P. Hatchett, P. Patel, R. Snavely, M. H. Key, A. Nikroo, R. Stephens, C. Stoeckl, K. A. Tanaka, T. Norimatsu, Y. Toyama, and R. Kodama, Phys. Plasmas **11**, 2746 (2004).
4. M. Tabak *et al.*, Fusion Sci. Technol. **49**, 254 (2006).
5. R. Betti and C. Zhou, Phys. Plasmas **12**, 110702 (2005).
6. R. R. Freeman *et al.*, Fusion Sci. Technol. **49**, 297 (2006); R. R. Freeman, K. Akli, F. Beg, R. Betti, S. Chen, D. J. Clark, P. M. Gu, G. Gregori, S. P. Hatchett, D. Hey, K. Highbarger, J. M. Hill, N. Izumi, M. Key, J. A. King, J. A. Koch, B. Lasinski, B. Langdon, A. J. MacKinnon, D. Meyerhofer, N. Patel, P. Patel, J. Pasley, H. S. Park, C. Ren, R. A. Snavely, R. B. Stephens, C. Stoeckl, M. Tabak, R. Town, L. Van Woerkom, R. Weber, S. C. Wilks, and B. B. Zhang, J. Phys. IV France **133**, 95 (2006); M. Tabak *et al.*, Phys. Plasmas **12**, 057305 (2005); R. B. Stephens, R. P. J. Snavely, Y. Aglitskii, K. U. Akli, F. Amiranoff, C. Andersen, D. Batani, S. D. Baton, T. Cowan, R. R. Freeman, J. S. Green, H. Habara, T. Hall, S. P. Hatchett, D. S. Hey, J. M. Hill, J. L. Kaae, M. H. Key, J. A. King, J. A. Koch, R. Kodama, M. Koenig, K. Krushelnick, K. L. Lancaster, A. J. MacKinnon, E. Martinolli, C. D. Murphy, M. Nakatsutsumi, P. Norreys, E. Perelli-Cippo, M. Rabec Le Gloahec, B. Remington, C. Rousseaux, J. J. Santos, F. Scianitti, C. Stoeckl, M. Tabak, K. A. Tanaka, W. Theobald, R. Town, T. Yabuuchi, and B. Zhang, J. Phys. IV France **133**, 355 (2006).
7. K. Mima, T. Takeda, and FIREX Project Group, Fusion Sci. Technol. **49**, 358 (2006).
8. C. Stoeckl, J. A. Delettrez, J. H. Kelly, T. J. Kessler, B. E. Kruschwitz, S. J. Loucks, R. L. McCrory, D. D. Meyerhofer, D. N. Maywar, S. F. B. Morse, J. Myatt, A. L. Rigatti, L. J. Waxer, J. D. Zuegel, and R. B. Stephens, Fusion Sci. Technol. **49**, 367 (2006).
9. S. C. Wilks *et al.*, Phys. Rev. Lett. **69**, 1383 (1992).
10. R. Betti, A. A. Solodov, J. A. Delettrez, and C. Zhou, Phys. Plasmas **13**, 100703 (2006).

11. S. Atzeni, *Phys. Plasmas* **6**, 3316 (1999).
12. C. Deutsch *et al.*, *Phys. Rev. Lett.* **77**, 2483 (1996).
13. C. K. Li and R. D. Petrasso, *Phys. Rev. E* **70**, 067401 (2004).
14. S. Atzeni and M. Tabak, *Plasma Phys. Control. Fusion* **47**, B769 (2005).
15. J. J. Honrubia and J. Meyer-ter-Vehn, *Nucl. Fusion* **46**, L25 (2006).
16. P. B. Radha, T. J. B. Collins, J. A. Delettrez, Y. Elbaz, R. Epstein, V. Yu. Glebov, V. N. Goncharov, R. L. Keck, J. P. Knauer, J. A. Marozas, F. J. Marshall, R. L. McCrory, P. W. McKenty, D. D. Meyerhofer, S. P. Regan, T. C. Sangster, W. Seka, D. Shvarts, S. Skupsky, Y. Srebro, and C. Stoeckl, *Phys. Plasmas* **12**, 056307 (2005).
17. R. Betti, K. Anderson, J. Knauer, T. J. B. Collins, R. L. McCrory, P. W. McKenty, and S. Skupsky, *Phys. Plasmas* **12**, 042703 (2005).
18. J. Delettrez, R. Epstein, M. C. Richardson, P. A. Jaanimagi, and B. L. Henke, *Phys. Rev. A* **36**, 3926 (1987).
19. R. B. Stephens *et al.*, *Phys. Rev. Lett.* **91**, 185001 (2003); R. B. Stephens, S. P. Hatchett, M. Tabak, C. Stoeckl, H. Shiraga, S. Fujioka, M. Bonino, A. Nikroo, R. Petrasso, T. C. Sangster, J. Smith, and K. A. Tanaka, *Phys. Plasmas* **12**, 056312 (2005).
20. C. D. Zhou and R. Betti, "Hydrodynamic Relations for Direct-Drive Fast-Ignition and Conventional Inertial Confinement Fusion Implosions," submitted to *Physics of Plasmas*.
21. J. A. Delettrez, J. Myatt, P. B. Radha, C. Stoeckl, S. Skupsky, and D. D. Meyerhofer, *Plasma Phys. Control. Fusion* **47**, B791 (2005).
22. Y. Sentoku *et al.*, *Fusion Sci. Technol.* **49**, 278 (2006).
23. R. P. J. Town *et al.*, *Nucl. Instrum. Methods Phys. Res. A* **544**, 61 (2005); R. J. Mason, *Phys. Rev. Lett.* **96**, 035001 (2006).
24. M. H. Key *et al.*, *Phys. Plasmas* **5**, 1966 (1998); R. Kodama *et al.*, *Nature* **418**, 933 (2002); K. Yasuike *et al.*, *Rev. Sci. Instrum.* **72**, 1236 (2001); M. H. Key, M. D. Cable, T. E. Cowan, K. G. Estabrook, B. A. Hammel, S. P. Hatchett, E. A. Henry, D. E. Hinkel, J. D.ilkenny, J. A. Koch, W. L. Kruer, A. B. Langdon, B. F. Lasinski, R. W. Lee, B. J. MacGowan, A. MacKinnon, J. D. Moody, M. J. Moran, A. A. Offenberger, D. M. Pennington, M. D. Perry, T. J. Phillips, T. C. Sangster, M. S. Singh, M. A. Stoyer, M. Tabak, G. L. Tietbohl, M. Tsukamoto, K. Wharton, and S. C. Wilks, *Phys. Plasmas* **5**, 1966 (1998).
25. S. P. Hatchett, D. Clark, M. Tabak, R. E. Turner, C. Stoeckl, R. B. Stephens, H. Shiraga, and K. Tanaka, *Fusion Sci. Technol.* **49**, 327 (2006).
26. P. W. McKenty, V. N. Goncharov, R. P. J. Town, S. Skupsky, R. Betti, and R. L. McCrory, *Phys. Plasmas* **8**, 2315 (2001).
27. S. C. Wilks and W. L. Kruer, *IEEE J. Quantum Electron.* **33**, 1954 (1997).
28. K. S. Anderson, R. Betti, P. W. McKenty, P. B. Radha, and M. M. Marinak, *Bull. Am. Phys. Soc.* **51**, 32 (2006).

---

# Femtosecond Optical Generation and Detection of Coherent Acoustic Phonons in GaN Single Crystals

## Introduction

Coherent acoustic phonons (CAP's) excited by ultrafast laser pulses have been investigated using optical pump/probe spectroscopy in GaN systems, including GaN thin films,  $\text{In}_x\text{Ga}_{1-x}\text{N}$ /GaN heterostructures, and multiple quantum wells.<sup>1–5</sup> A common feature of such structures is the existence of a significant lattice mismatch, which results in highly strained interfaces. Since GaN and its alloys are piezoelectric semiconductors with large piezoelectric constants, the presence of strain at the interface gives rise to a strong, of-the-order-of-several-MV/cm,<sup>5</sup> built-in piezoelectric field. When a pump-laser pulse excites electron-hole pairs, the strain-induced piezoelectric field spatially separates the electrons and holes and, in turn, leads to a stress that serves as the source of CAP generation.

In addition to the piezoelectric effect, two other CAP-generation mechanisms have been reported in the literature:<sup>6,7</sup> the deformation-potential-coupled electronic stress and the heat-induced thermal stress. Both of these stresses originate in the transient photoexcitation of electron-hole pairs in the material. In one case, the transition of electrons from the valence band to the conduction band breaks the lattice equilibrium and results in a deformation of the lattice. Such deformation, in turn, alters the semiconductor band structure and induces the electronic stress coupled to the conduction-band free carriers through the deformation potential. In the other case, the photoexcited carriers simply transfer their excess energy to the lattice via electron-phonon scattering, as they relax down toward the band edge. The fast cooling process of hot carriers produces a sharp increase in the lattice temperature, leading to thermal stress.

Among the above-mentioned mechanisms of CAP generation, the piezoelectric effect always makes the dominant contribution in the strained systems, studied in Refs. 1–5, while the other two typically play only a very weak role, as discussed in Ref. 5. However, in bulk semiconductor single crystals (GaN, in our case), there is obviously no lattice-mismatch-induced strain and the piezoelectric field cannot be built. Thus, the CAP

generation can only be due to either the electronic or thermal stress, or both, depending on the photon excitation energy and the studied material's properties.

In recent work,<sup>8</sup> we have demonstrated that in bulk GaN crystals the stress-induced CAP's are very long lived and propagate macroscopic distances without losing their coherence. We utilized far-above-bandgap, ultraviolet (UV) femtosecond pump pulses to excite the CAP's at the sample surface and detected them by measuring the transient differential reflectivity ( $\Delta R/R$ ) signal of a time-delayed, near-infrared (NIR) probe pulse. We observed the CAP oscillations (superimposed on the exponentially decaying  $\Delta R/R$  electronic transient) with the amplitude of the order of  $10^{-5}$  to  $10^{-6}$  and the frequency linearly dependent (no dispersion) on the probe-beam wave number. We have also made an early prediction that the electronic stress was the dominant factor in CAP generation in bulk GaN crystals.

In this work, we report our systematic experimental and detailed theoretical modeling studies on all-optical generation and detection of CAP's in bulk GaN crystals with the two-color (UV/blue–NIR), time-resolved, femtosecond pump/probe technique. Our theoretical modeling is based on the one-dimensional elastic wave equation and diffusion effects and predicts that the electronic stress is the dominant factor in CAP generation in GaN single crystals. For a CAP-detection mechanism, we have derived an analytic expression for the time-dependent, probe-beam reflectivity change caused by the propagating CAP's. Experimentally, we have varied the energy of the pump excitation pulses from far above the GaN bandgap, through near bandgap, up to just below bandgap (band-tail states). In all cases, we were able to produce easily measurable CAP oscillations, and, by careful investigation of their amplitude changes as a function of the energy (wavelength) of the pump photons, we confirmed that indeed the CAP excitation origin was due to the electronic stress, generated by the femtosecond pump at the sample surface region. By using, in all of our tests, probe beams with photon energies far below

the GaN bandgap (corresponding wavelengths were around 800 nm), we took advantage of a very small,  $\sim 50\text{-cm}^{-1}$  absorption coefficient (very weak attenuation) of probe light in GaN crystals<sup>8,9</sup> and were able to demonstrate that the CAP pulses propagated deeply into the GaN crystal volume without any measurable loss of coherence/attenuation.

Another advantage of our two-color pump/probe configuration was that the NIR probe was not sensitive to the details of the band-gap structure, nor to any interband absorption.<sup>10</sup> The possibility of the two-photon-absorption process was also negligible because the total energy of two  $\sim 800\text{-nm}$  probe photons was still considerably lower than the GaN bandgap energy. Thus, the UV-NIR, two-color femtosecond spectroscopy allowed us to avoid any undesired effects and made our phonon dynamics studies in GaN very clear to interpret.

In the next section we present our theoretical approach to the phenomenon of acoustic phonon generation and their coherent propagation in bulk semiconducting single crystals, stressing the need to include both electronic and thermal stresses in the phonon-generation mechanism. We also demonstrate that under our experimental conditions, for GaN, the amplitude of the CAP's depends only on the energy/wavelength of pump photons, while their oscillation frequency is probe dependent only in the simplest-possible dispersionless manner. The last two sections (1) briefly review our GaN crystal growth, describe the two-color femtosecond spectroscopy setup used in our measurements, and present detailed experimental results and their interpretation; and (2) present our conclusions and underline the applicability of our theoretical model for CAP studies in any high-quality single-crystal semiconducting materials.

### Theoretical Modeling

Following the approach presented by Thomsen *et al.*,<sup>7</sup> we have developed a theoretical model of the generation, propagation, and detection of CAP's in bulk GaN crystals, studied using a femtosecond, two-color pump/probe technique. In our scheme, an intense, femtosecond laser pump pulse with photon energy above the material bandgap excites both the electronic and thermal stresses at the sample surface. These two stresses act as the driving terms in the elastic wave equation that describes generation and propagation of CAP's. The propagating CAP's modulate optical properties of the GaN dielectric function, which is represented as disturbance of a dielectric permittivity in Maxwell's equations. By solving the Maxwell equations, we obtained an analytical expression for the time-dependent modulation of the  $\Delta R/R$  transient caused by the

traveling CAP waves, which, in turn, could be directly measured in our experiments, using below-bandgap probe pulses.

We stress that the Thomsen model was developed to explain generation and detection of CAP's in  $\alpha\text{-As}_2\text{Te}_3$  and similar compounds with a picosecond, one-color pump/probe method.<sup>7</sup> In such a case, the CAP generation was assumed to be solely due to the thermal stress, and the detection was limited in a near-surface region. In the model presented here, we will consider both the electronic- and thermal-stress generation mechanisms. Since GaN exhibits relatively large deformation potential and different coefficients in ambipolar and thermal diffusion, the contribution of the electronic stress to the CAP's amplitude and shape is different from that of the thermal stress. Our theoretical calculations show that in GaN, CAP's generated by electronic stress have actually an-order-of-magnitude-larger strength than that generated by the thermal stress.

In the experimental CAP detection, we use far-below-bandgap femtosecond probe-beam pulses. For bulk samples, surface-generated CAP's propagate forward into the material with no reflections toward the surface. Thus, the surface (one-color scheme) detection scheme that was used by Thomsen *et al.*<sup>7</sup> to detect the echo of a CAP pulse is not appropriate in our case. In contrast, by using a far-below-bandgap probe beam, we were able to detect the CAP perturbation propagating deeply inside the material, taking advantage of the very long penetration depth (very low absorption) of our NIR probe photons.

#### 1. CAP Pulse Generation

We consider a femtosecond UV pump pulse with photon energy higher than the GaN bandgap that is incident on the surface of a bulk GaN crystal. Given that the diameter of the irradiated area is much larger than the UV pulse absorption depth, both the electronic and thermal stresses generated by the pump pulse can be assumed to depend only on the  $z$  axis, which is defined to be perpendicular to the sample surface and pointing into the sample. Therefore, the lattice displacement has a nonzero component only in the  $z$  direction, and, in our case, the CAP generation is reduced to a one-dimensional (1-D) problem.

The 1-D elastic (nondissipative) wave equation describing generation and propagation of CAP's is given by

$$\frac{\partial^2 \eta_{zz}(z,t)}{\partial t^2} - v_s^2 \frac{\partial^2 \eta_{zz}(z,t)}{\partial z^2} = \frac{1}{\rho} \frac{\partial}{\partial z} (\sigma_{zz}^{\text{th}} + \sigma_{zz}^e), \quad (1)$$

where  $\eta_{zz}(z,t) = \partial u(z,t)/\partial z$  represents the acoustic phonon field with  $u(z,t)$  defined as the lattice displacement,  $v_s$  is the longitudinal sound velocity in GaN,  $\rho$  is the mass density of GaN, and  $\sigma_{zz}^{\text{th}}$  and  $\sigma_{zz}^e$  are the thermal and electronic stresses, respectively. Both  $\sigma_{zz}^{\text{th}}$  and  $\sigma_{zz}^e$  are functions of  $z$  and time  $t$  and can be expressed as

$$\sigma_{zz}^{\text{th}}(z,t) = -3B\beta\Delta T(z,t), \quad (2)$$

$$\sigma_{zz}^e(z,t) = d_c n_e(z,t) - d_v n_h(z,t), \quad (3)$$

where  $B$  is the bulk modulus,  $\beta$  is the linear thermal expansion coefficient,  $\Delta T(z,t)$  is the lattice temperature rise,  $d_c$  and  $d_v$  are the conduction-electron and valence-hole deformation potentials, respectively, and, finally,  $n_e(z,t)$  and  $n_h(z,t)$  are the photoexcited electron and hole densities, respectively. In general,  $n_e(z,t)$  and  $n_h(z,t)$  have different spatiotemporal evolutions, but, since in our case they are initially excited in equal numbers by the same pump pulse, we are going to ignore this difference and assume that  $n_e(z,t) \approx n_h(z,t) = n(z,t)$ , and, hence, Eq. (3) becomes

$$\sigma_{zz}^e(z,t) = (d_c - d_v)n(z,t). \quad (4)$$

Assuming that both the carrier motion and heat conduction have a diffusive character, we utilize a simple transport model to describe the evolution of  $n(z,t)$  and  $\Delta T(z,t)$ :

$$\frac{\partial n(z,t)}{\partial t} - D \frac{\partial^2 n(z,t)}{\partial z^2} = 0, \quad (5)$$

$$\frac{\partial \Delta T(z,t)}{\partial t} - \chi \frac{\partial^2 \Delta T(z,t)}{\partial z^2} = 0, \quad (6)$$

with the initial conditions

$$n(z,0) = \frac{\alpha_{\text{pump}}(1 - R_{\text{pump}})Q}{E_{\text{pump}}} \exp(-\alpha_{\text{pump}}z), \quad (7)$$

$$\Delta T(z,0) = \frac{\alpha_{\text{pump}}(1 - R_{\text{pump}})Q}{E_{\text{pump}}} \times \frac{E_{\text{pump}} - E_g}{C_V} \exp(-\alpha_{\text{pump}}z), \quad (8)$$

and boundary conditions

$$D \frac{\partial n(0,t)}{\partial z} = 0, \quad (9)$$

$$\chi \frac{\partial \Delta T(0,t)}{\partial z} = 0, \quad (10)$$

where  $D$  is the ambipolar diffusion coefficient of the GaN electron-hole plasma;  $\chi$  is the thermal diffusivity;  $R_{\text{pump}}$ ,  $Q$ ,  $\alpha_{\text{pump}}$ , and  $E_{\text{pump}}$  are the reflectance, fluence, absorption coefficient, and photon energy of the pump beam; and  $E_g$  and  $C_V$  are the GaN bandgap energy and the specific heat per unit volume, respectively. We have also assumed above that during the duration of our  $\sim 150$ -fs-wide pump pulses, the photoexcitation is instantaneous and the plasma diffusion is negligible.

Knowing the  $n(z,t)$  and  $\Delta T(z,t)$  distributions, we can readily solve the wave equation [Eq. (1)], subject to the initial,  $t = 0$ , and elastic boundary,  $z = 0$ , conditions:

$$\eta_{zz}(z,0) = 0, \quad (11)$$

$$\eta_{zz}(0,t) = \frac{1}{\rho V_s^2} [3B\beta\Delta T(0,t) - (d_c - d_v)n(0,t)]. \quad (12)$$

In our analysis of CAP generation, the two trigger mechanisms, namely, the electronic and thermal stresses, are completely decoupled. Thus, the CAP fields excited by each mechanism can be treated separately, and the total CAP field is just the simple sum of both the electronic and thermal components. Figure 110.27 presents examples of numerically computed profiles of CAP transients, generated by the electronic stress, the thermal stress, and the sum of both, respectively. The CAP pulses plotted in Fig. 110.27(a) were calculated for the far-above-bandgap pump-photon excitation (photon energy of 4.59 eV; corresponding wavelength 270 nm), while those shown in Fig. 110.27(b) correspond to the excitation using just-above-bandgap pump photons (energy of 3.54 eV; wavelength 350 nm). In both cases,  $Q$  was kept constant and equal to 0.08 mJ/cm<sup>2</sup>/pulse, the value actually implemented in our pump/probe experiments, while the  $\alpha_{\text{pump}}$  values were taken to be  $2.07 \times 10^5$  and  $1.29 \times 10^5$  cm<sup>-1</sup>, corresponding to the pump-photon energies of 4.59 eV and 3.54 eV, respectively.<sup>9</sup> The other GaN material parameters used in our calculations can be found in Table 110.III.

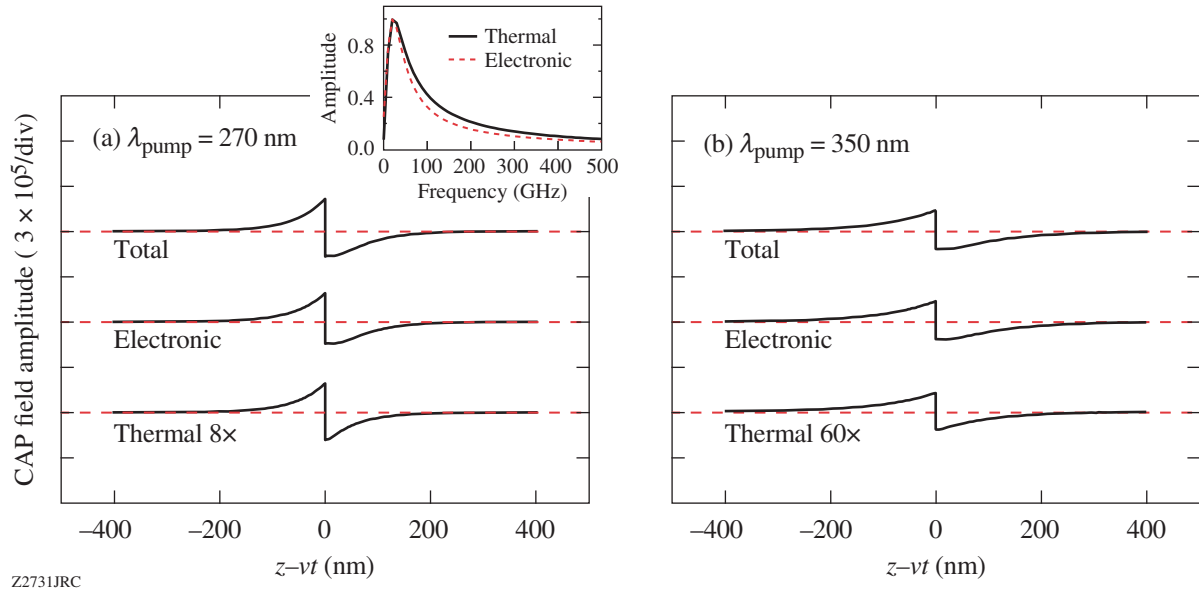


Figure 110.27

Simulation of spatial-time profiles of propagating CAP transients generated by the electronic stress, thermal stress, and the sum of both, respectively. The CAP pulses shown in (a) and (b) were excited by the pump photons with photon energies of 4.59 eV and 3.54 eV (wavelengths 270 nm and 350 nm), respectively. The inset shows the frequency spectra of the electronically (solid line) and thermally induced (dashed line) CAP.

Table 110.III. Material parameters for wurtzite GaN.

Parameter	GaN
Longitudinal sound velocity $v_s$ (m/s)	8020 <sup>(11)</sup>
Mass density $\rho$ (g/cm <sup>3</sup> )	6.15 <sup>(12)</sup>
Bulk modulus $B$ (GPa)	207 <sup>(13)</sup>
Linear thermal expansion coefficient $\beta$ (K <sup>-1</sup> )	$3.17 \times 10^{-6}$ <sup>(14)</sup>
Electron deformation potential $d_c$ (eV)	-4.08 <sup>(15)</sup>
Hole deformation potential $d_v = D1 + D3$ (eV)	2.1 <sup>(16)</sup>
Ambipolar diffusion coefficient $D$ (cm <sup>2</sup> /s)	2.1 <sup>(17)</sup>
Thermal diffusivity $\chi$ (cm <sup>2</sup> s <sup>-1</sup> )	0.43 <sup>(12)</sup>
Band gap $E_g$ (eV)	3.4 <sup>(18)</sup>
Specific heat per unit volume $C_V$ (J cm <sup>-3</sup> C <sup>-1</sup> )	3.01 <sup>(12)</sup>

As seen in Fig. 110.27, CAP pulses have a strength of the order of  $10^{-5}$  and a spatial width of approximately twice the pump-beam penetration depth ( $\xi_{\text{pump}} = 1/\alpha_{\text{pump}}$ ). We note, however, that our simulations predict that the electronic stress contribution is the major, dominant contribution in CAP generation, as compared to the thermal-stress contribution, in both the far-above- and just-above-bandgap excitations [Figs. 110.27(a) and 110.27(b), respectively], with the strength ratio between the electronic- and thermal-induced CAP's equal to about 8 and 60 for the 4.59- and 3.54-eV pump photons, respectively. The electronically induced strength of CAP's decreases only slightly when the pump photon energy decreases from 4.59 eV to 3.54 eV, while the thermal one drops by about an order of magnitude. Thus, the change of the total CAP strength is small [see Figs. 110.27(a) and 110.27(b), bottom curves], as it is electronically dominated. The CAP amplitude is determined mainly by  $\alpha_{\text{pump}}$ , which changes only a little in the studied above-bandgap, pump-energy region.

The shapes of all CAP pulses presented in Fig. 110.27 are asymmetrically bipolar with a slight broadening at their trailing sides. This broadening is caused by the diffusion effects<sup>7</sup> and is much more pronounced in the electronically induced CAP's because the electron-hole diffusion is about five times faster than the thermal diffusion. The diffusion effects not only broaden the CAP pulse, but they also narrow its frequency

spectrum [inset in Fig.110.27(a)], where the spectra of the electronically and thermally induced CAP's are shown.

## 2. CAP Pulse Detection

In the discussed GaN sample geometry, the surface-generated CAP pulses propagate into the crystal along the  $z$  axis, causing a spatiotemporal modulation of the material's dielectric function. This modulation can be detected through the change in the reflectivity  $R$  of a time-delayed probe beam. The  $R$  dependence in the presence of a generalized disturbance of the dielectric function can be obtained by solving the Maxwell equations inside the GaN sample and was derived by Thomsen *et al.*<sup>7</sup> as

$$R = |r_0 + \Delta r|^2, \quad (13)$$

where

$$r_0 = \frac{1 - n - i\kappa}{1 + n + i\kappa} \quad (14)$$

is the reflection coefficient at the sample surface and represents that part of the probe beam's electric field reflected from the free surface, while

$$\Delta r = \frac{2i\omega}{c(1 + n + i\kappa)^2} \int_0^\infty dz' e^{2i(n + i\kappa)k_0 z'} \Delta\mathcal{E}(z, t) \quad (15)$$

corresponds to the probe beam's electric field reflected from the CAP pulse. In Eqs. (14) and (15),  $n$  and  $\kappa$  are the real and imaginary parts of the refractive index, respectively;  $\omega$ ,  $c$ , and  $k_0$  are the angular frequency of the probe light, the light speed, and the wave vector of the probe beam in vacuum, respectively; and  $\Delta\mathcal{E}(z, t)$  is the change in dielectric function, which, under assumption that the disturbance is caused only by the propagating CAP pulse, can be expressed as

$$\Delta\mathcal{E}(z, t) = 2(n + i\kappa) \left( \frac{dn}{d\eta_{zz}} + i \frac{d\kappa}{d\eta_{zz}} \right) \eta_{zz}(z, t). \quad (16)$$

Finally, we note that  $\kappa$  is related to the probe-beam absorption coefficient  $\alpha_{\text{probe}}$  or, equivalently, the penetration depth  $\zeta_{\text{probe}}$  through  $\kappa = \alpha_{\text{probe}} \lambda / 4\pi = \lambda / 4\pi \zeta_{\text{probe}}$ , where  $\lambda$  is the probe-beam wavelength.

Since our experiments measure the probe's  $\Delta R/R$  signal, Eq. (13) must be rewritten in the form

$$\Delta R/R = \frac{|r_0 + \Delta r|^2 - |r_0|^2}{|r_0|^2}. \quad (17)$$

The analytic expression of  $\Delta R/R$  can be obtained if  $n_{zz}(z, t)$ , which we have only in a numerical form presented in Fig. 110.27, is substituted in Eq. (16) by an analytic expression:

$$\eta_{zz}(z, t) = -A e^{-\alpha_{\text{pump}} |z - v_s t|} \text{sgn}(z - v_s t), \quad (18)$$

which fits our stress pulses very well and neglects only the electron-hole and thermal diffusion effects in the CAP generation, and  $A$  is the strength of the CAP pulse given by

$$A = \frac{\alpha_{\text{pump}}(1 - R_{\text{pump}})Q}{2E_{\text{pump}}\rho v_s^2} \times \left[ -(d_c + d_v) + \frac{3B\beta}{C_V}(E_{\text{pump}} - E_g) \right]. \quad (19)$$

Combining the above formulas and considering that for our two-color pump/probe technique the condition  $\alpha_{\text{pump}} \gg \alpha_{\text{probe}}$  holds, we find an analytic expression for  $\Delta\mathcal{E}(z, t)$  and, finally, obtain the closed-form formula for  $\Delta R/R$ , correct to the first order in  $n_{zz}(z, t)$ :

$$\Delta R/R = \sqrt{\left( \frac{dn}{d\eta_{zz}} \right)^2 + \left( \frac{d\kappa}{d\eta_{zz}} \right)^2} A F_1 \times \left[ \sin\left( \frac{4\pi n v_s t}{\lambda} - \phi \right) e^{-v_s t / \zeta_{\text{probe}}} + F_2 e^{-v_s t / \zeta_{\text{pump}}} \right], \quad (20)$$

where

$$F_1 = \frac{\sqrt{n^2(n^2 + \kappa^2 - 1)^2 + \kappa^2(n^2 + \kappa^2 + 1)^2}}{n(n^2 + \kappa^2 + 1)^2 - 4n^3} \quad (21)$$

is the probe-beam-related amplitude,

$$\phi = \arctan\left[ \frac{\kappa(n^2 + \kappa^2 + 1)}{n(n^2 + \kappa^2 - 1)} \right] \arctan\left[ \frac{dn/d\eta_{zz}}{d\kappa/d\eta_{zz}} \right] \quad (22)$$

is the phase, and

$$F_2 = \frac{8\pi^2 n^2 \sin \phi - 2\pi n \lambda \alpha_{\text{pump}} \cos \phi}{16\pi^2 n^2 + \lambda^2 \alpha_{\text{pump}}^2}. \quad (23)$$

Equation (20) allows us to directly compare our theoretical modeling with the experiments, facilitating data analysis and making our results more explicit. We can, however, simplify Eq. (20) somewhat further by noting that under our experimental conditions,  $\zeta_{\text{pump}}$  is of the order of several tens of nanometers; thus, for the GaN sound speed  $v_s = 8020$  m/s, the second term in the square bracket in Eq. (20) rapidly damps out within several picoseconds and can be neglected, as in our experiments we study CAP's within at least a few-hundred-ps-wide time delay window. The simplified expression of  $\Delta R/R$  can be written as

$$\Delta R/R = \sqrt{\left(\frac{dn}{d\eta_{zz}}\right)^2 + \left(\frac{d\kappa}{d\eta_{zz}}\right)^2} \times AF_1 \sin\left(\frac{4\pi n v_s t}{\lambda} - \phi\right) e^{-v_s t / \zeta_{\text{probe}}}. \quad (24)$$

The temporal dependence of  $\Delta R/R$  is represented in Eq. (24) as a simple damped-sinusoidal function and it follows Eq. (48) in Ref. 7, but now we also have an expression for the  $\Delta R/R$  amplitude, as the product of  $A$ ,  $F_1$ , and  $\sqrt{(dn/d\eta_{zz})^2 + (d\kappa/d\eta_{zz})^2}$ . The probe-related  $F_1$  [see Eq. (21)] can be considered as a constant since for far-below-bandgap NIR light,  $n$  and  $\kappa$  in high-quality GaN crystals remain almost unchanged. The  $dn/d\eta_{zz}$  and  $d\kappa/d\eta_{zz}$  terms are the photoelastic constants and are related only to  $n$  and  $\kappa$ ; thus,  $\sqrt{(dn/d\eta_{zz})^2 + (d\kappa/d\eta_{zz})^2}$  also contributes a constant term in the total  $\Delta R/R$  amplitude. Finally, following Eq. (19), the term  $A$  (strength of the CAP pulse) is only pump light related. We note that  $A$  experiences a dramatic change when the pump energy is tuned across the band edge because of the step-like change of  $\alpha_{\text{pump}}$  near  $E_g$ . Experimentally it means that the total  $\Delta R/R$  amplitude measured using the two-color pump/probe technique should change with the pump-beam energy, following the same functional dependence as  $A$ , namely the spectral characteristics of  $\alpha_{\text{pump}}$ . Furthermore, this theoretical prediction indicates that we should be able to undeniably determine which stress contribution—electronic or thermal—is the dominant factor for triggering the CAP's in our bulk GaN crystals. If the electronic stress is dominant, as we saw in **CAP Pulse Generation** (p. 89), the experimentally observed  $\Delta R/R$  amplitude should exhibit only a slight decrease when the pump energy changes from far above to just above bandgap. On the

other hand, when the thermal stress is dominant, the oscillation amplitude should experience an-order-of-magnitude drop in the same pump-energy range. Independently, when the pump beam energy is tuned across band edge, the amplitude of the experimental  $\Delta R/R$  signal should almost abruptly decrease to zero, due to the rapid decrease of  $\alpha_{\text{pump}}$ .

In agreement with the Thomsen model,<sup>7</sup> the  $\Delta R/R$  damping constant in Eq. (21) is determined by the  $\zeta_{\text{probe}}/v_s$  ratio. For the  $\sim 800$ -nm-wavelength (energy far below the GaN bandgap) probe light used in our two-color measurements,  $\zeta_{\text{probe}}$  is  $\sim 200$   $\mu\text{m}$ ,<sup>8,9</sup> which gives a damping time of  $\sim 25$  ns. Thus, we should observe CAP's propagating deeply into the GaN crystal, actually, in full agreement with our early studies.<sup>8</sup>

Following again Eq. (24), the frequency of the  $\Delta R/R$  oscillations is given by

$$f = 2n v_s / \lambda = \frac{n v_s}{\pi} k_0 \quad (25)$$

and is related only to the probe beam. For a constant  $n$ , expected under our experimental conditions,  $f$  is proportional to  $k_0$ , which indicates a linear dispersion relation for CAP's with the slope corresponding to the fixed  $v_s$ . Finally,  $\phi$  [see Eq. (22)] is, in our case, predicted to be a constant.

## Experimental Procedures and Results

### 1. Sample Fabrication and Experimental Setup

Our GaN single crystals were grown with a high-pressure, solution-growth (HPSG) method.<sup>19</sup> The growth process was carried out at an external nitrogen gas pressure of 8 to 14 kbar and temperatures of 1350°C to 1600°C because of the high solubility of GaN in Ga at high temperatures. Nitrogen was first compressed to a 10- to 15-kbar level with a two-step pressure compressor and intensifier and then transported into the metallic Ga melt with a temperature gradient of 5°C to 50°C  $\text{cm}^{-1}$ . GaN single crystals formed at the cooler zone of the HPSG chamber. They grew up to 1-mm-thick platelets with typical sizes of up to  $3 \times 4$   $\text{mm}^2$ . These crystals exhibited an excellent wurtzite crystalline structure according to x-ray diffraction measurements, while their morphology depended on the growth process pressure, temperature range, and nitrogen supersaturation. In our experiments, we have studied a  $2.5 \times 2.5$ - $\text{mm}^2$ , transparent (slightly brownish) GaN crystal piece that was  $\sim 0.4$  mm thick.

Two-color, femtosecond pump/probe spectroscopy experiments were performed in a reflection mode using a commercial mode-locked Ti:sapphire laser with a pulse duration

of  $\sim 100$  fs and repetition rate of 76 MHz. Our experimental setup is schematically shown in Fig. 110.28. In our study, two arrangements were used to generate the pump beam with desired photon energy. One optical path (see Fig. 110.28) was designed to deliver photons with energies in the range of 3.1 to 3.54 eV (wavelength of 400 to 350 nm) in the vicinity of a GaN bandgap of 3.4 eV and was based on frequency doubling of the fundamental Ti:sapphire pulse train. The other included our homemade third-harmonic generator and allowed us to generate pump photons with energies ranging from 4.13 eV to 4.64 eV (wavelength of 300 to 267 nm), far above the GaN bandgap. The pump beam was focused onto the surface of the GaN crystal with a spot diameter of  $\sim 20$   $\mu\text{m}$  at an incident angle of  $\sim 30^\circ$ . The incident fluence was  $\sim 0.08$  mJ/cm<sup>2</sup> per pulse and was kept constant while varying the pump-photon energy. Probe pulses were directly generated by the Ti:sapphire laser and had photon energies varying from 1.38 eV to 1.77 eV (wavelengths from 900 nm to 700 nm) far below the GaN gap; their fluence was always much lower (at least by a factor of 10) than that of the pump. The probe beam was delayed with respect to the pump and near-normally incident on the same area on the sample surface with a spot diameter of  $\sim 10$   $\mu\text{m}$ , and its reflection from the sample surface was filtered from any scattered pump photons and collected by a photodetector connected to a lock-in amplifier. The lock-in amplifier was synchronized with a mechanical chopper that modulated the pump beam at a frequency of  $\sim 2$  KHz. The lock-in output was sent to a computer for data processing. The magnitude of  $\Delta R/R$  that we measured was in the range of  $10^{-3}$  to  $10^{-6}$ .

## 2. Experimental Results

Typical time-resolved  $\Delta R/R$  probe signals from our GaN crystal excited with far-above-bandgap (wavelength of 283 nm) and just-above-bandgap (wavelength of 350 nm) pump photons

are shown in Figs. 110.29(a) and 110.29(b), respectively. The corresponding probe wavelengths are 850 nm in Fig. 110.29(a) and 720 nm in Fig. 110.29(b). As we can see, although the two presented  $\Delta R/R$  waveforms exhibit different electronic relaxation features, observed during the initial few picoseconds of relaxation and associated with the conduction band inter- and intra-valley electron scattering,<sup>10</sup> both are characterized by the same, few-hundred-ps-long exponential decay, associated

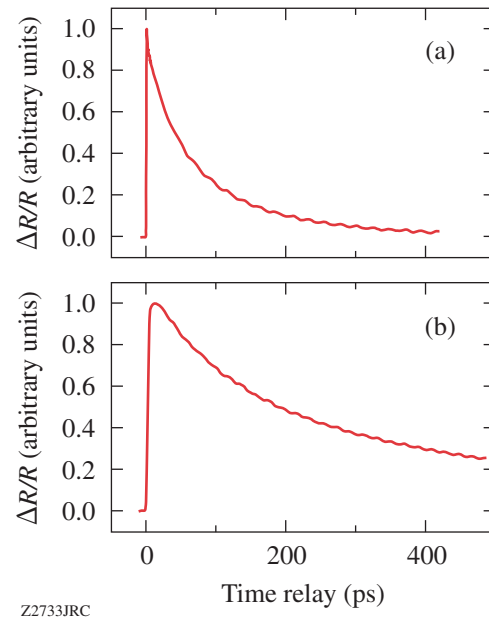


Figure 110.29

Time-resolved normalized  $\Delta R/R$  waveforms as a function of the pump/probe delay time, measured in GaN single crystals for (a) the pump/probe wavelength of 283 nm/850 nm; (b) pump/probe wavelength of 360 nm/720 nm. The case (a) corresponds to the far-above-bandgap optical excitation, while case (b) corresponds to just-above-bandgap excitation.

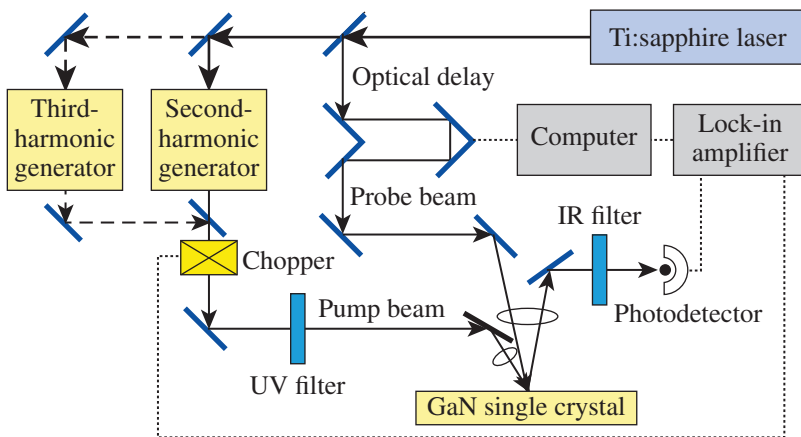


Figure 110.28

Experimental setup for the two-color, femtosecond pump/probe spectroscopy.

Z2732JRC

with the electron-hole recombination, with pronounced regular oscillations on top of it.

In this work, we focus only on this latter oscillatory feature, which we identify as propagation of the CAP transient inside the crystal.<sup>8</sup> Thus, in order to get a clearer view, we have subtracted numerically the electronic relaxation background from all of our collected raw data. Figure 110.30(a) shows the oscillatory component of the measured  $\Delta R/R$  signal for four experimental examples, representative of our measurement cases. The presented traces correspond to the three different experimental conditions for CAP excitation, namely, far-above-bandgap excitation (trace 283 nm/850 nm), just-above-bandgap excitation (traces 350 nm/700 nm and 360 nm/720 nm), and band-tail-state excitation (trace 370 nm/740 nm), respectively. In all cases, no attenuation of the oscillations is observed within our experimental  $\sim 450$ -ps-wide time-delay window, which is consistent with Eq. (24), predicting that in our experiments the CAP oscillation damping constant is limited by the  $\zeta_{\text{probe}}/v_s$  ratio and for  $\zeta_{\text{probe}}/v_s \approx 25$  ns is much longer than our experimental time window.

Figure 110.30(b) presents four  $\Delta R/R$  CAP-related transients calculated using Eq. (24) and corresponding directly to the four experimental transients shown in Fig. 110.30(a). In our theoretical calculations, the refractive index  $n = 2.3$  and the probe absorption coefficient  $\alpha_{\text{probe}} = 50 \text{ cm}^{-1}$  are assumed to remain unchanged for all of the studied probe wavelengths. The pump reflectance  $R_{\text{pump}}$  was set to be 0.2 and the constants  $dn/d\eta_{zz}$  and  $dk/d\eta_{zz}$  entering into Eqs. (21) and (22) were set to be

1.2 and 0.5, respectively, in order to keep the CAP amplitude term  $F_1$  and phase  $\phi$  consistent with our experimental values. We note that there is extremely good agreement between the corresponding experimental [Fig. 110.30(a)] and theoretical [Fig. 110.30(b)] traces, in terms of both the oscillation amplitude and frequency.

Comparing the traces 283 nm/850 nm, 350 nm/700 nm, and 360 nm/720 nm, we observe only a slight amplitude decrease as we move from the far-above- to just-above-bandgap excitation. On the other hand, the 370-nm/740-nm trace, collected for the pump-photon energy corresponding to GaN band-tail states, has a much smaller amplitude than the other three, but the oscillatory feature is still observable. The above observations experimentally confirm our theoretical prediction that the driving mechanism for CAP generation in bulk GaN crystals is the electronic stress associated with the deformation potential. The rapid drop in CAP amplitude that occurs when we move the energy of our excitation photons across the GaN bandgap (compare traces 360 nm/720 nm and 370 nm/740 nm in Fig. 110.30) is caused by the dramatic change of the  $\alpha_{\text{pump}}$  coefficient at the band edge. The latter is clearly illustrated in Fig. 110.31, where we plot the experimental CAP oscillation amplitude dependence on the pump-photon wavelength (energy) for the whole pump tuning range. The solid line shows the theoretical  $\Delta R/R$  amplitude dependence on the pump-photon energy, using Eq. (24) [see also Eq. (19)]. We used the values listed in Ref. 9 for the  $\alpha_{\text{pump}}$  spectral dependence in GaN crystals. The solid squares, circles, and triangles represent our experimental data corresponding to the far-above-bandgap, just-above-bandgap,

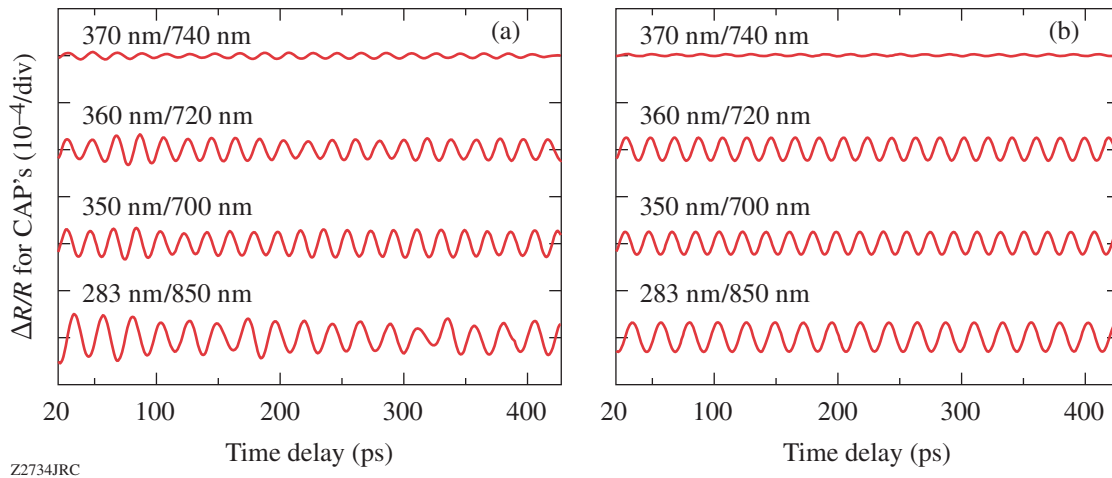


Figure 110.30

The oscillatory components of the  $\Delta R/R$  signals as a function of the pump/probe delay time for several pump/probe wavelength configurations: 370 nm/740 nm, 360 nm/720 nm, 350 nm/700 nm, and 283 nm/850 nm. Panels (a) and (b) show the experimental and theoretical results, respectively.

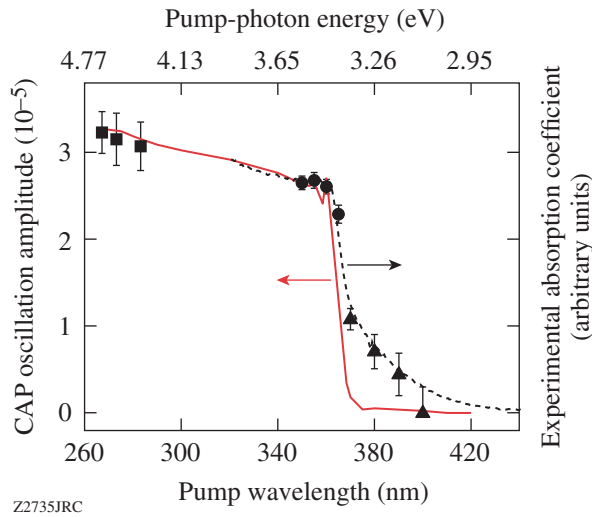


Figure 110.31

The amplitude of the CAP oscillations versus the pump-beam wavelength (energy–top axis). The solid line is the theoretical curve, while the solid squares, circles, and triangles are our experimental data points corresponding to the far-above-bandgap, just-above-bandgap, and band-tail-state pump excitations, respectively. The dashed line (right axis) is the experimental GaN absorption coefficient spectrum, extracted from the transmission and reflection data obtained for our actual GaN single crystal.

and band-tail-state pump excitations, respectively. We see very good overall agreement between our experimental points and the modeling. Only in the case of the pump photons exciting the band-tail states (solid triangles in Fig. 110.31), the decrease of the CAP amplitudes with the pump-wavelength increase is slower than the theoretical prediction. The latter discrepancy, however, is clearly a consequence that in our theoretical calculations we used the values of  $\alpha_{\text{pump}}$  from Ref. 9 and not  $\alpha_{\text{pump}}$  directly measured for our GaN samples. The dashed line in Fig. 110.31 corresponds to the GaN absorption coefficient spectrum extracted from the transmission and reflection data of our actual GaN single crystal, experimentally measured using a Perkin-Elmer Lambda 900 spectrophotometer. We note that in this case the agreement is excellent.

For all of the traces plotted in Fig. 110.30, the CAP oscillation phase was essentially constant and equal to  $\sim 1.2$ , as shown in Fig. 110.32, which presents  $\phi$  as a function of the probe-photon wavelength (energy) for our entire experimental tuning range. The constant  $\phi$  is very consistent with our theoretical prediction based on Eq. (22) and the fact that  $n$ ,  $\kappa$ ,  $dn/d\eta_{zz}$ , and  $d\kappa/d\eta_{zz}$  can be assumed constant for our NIR probe photons. The solid line in Fig. 110.32 was obtained by fitting Eq. (20) with  $(dn/d\eta_{zz})/(d\kappa/d\eta_{zz}) = 2.5$  as the best fit.

Finally, Fig. 110.33 demonstrates the dispersion relation of the CAP oscillation frequency on the probe beam's wave number. For the entire probe-beam tuning range from 700 nm to 850 nm, we observe a linear (dispersionless) relationship between  $f$  and  $k_0$ , as predicted by Eq. (25). The slope of the data (solid line in Fig. 110.33) gives  $v_s = 8002 \pm 22$  m/s. The

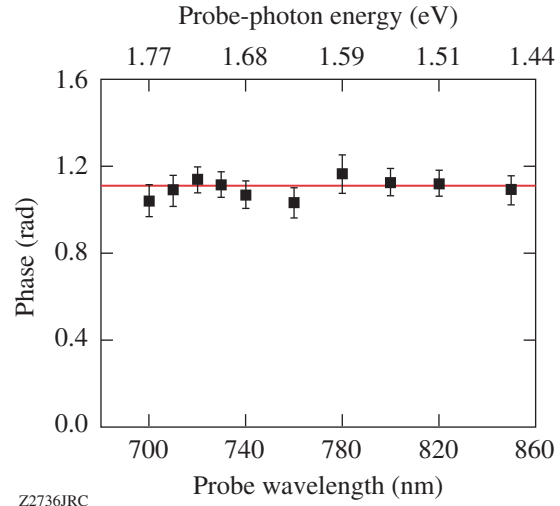


Figure 110.32

The phase of the CAP oscillation versus the probe-beam wavelength (energy–top axis). The solid line shows the theoretical fit based on Eq. (22) with  $(dn/d\eta_{zz})/(d\kappa/d\eta_{zz}) = 2.5$ .

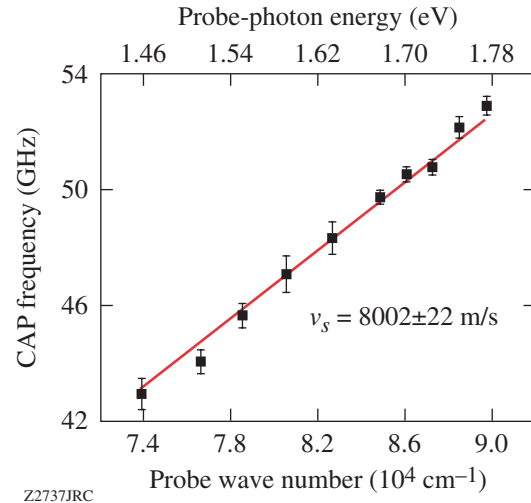


Figure 110.33

The CAP oscillation frequency dependence on the probe beam's wave number (energy–top axis). The solid squares are the peak values of the CAP oscillations Fourier spectra, while the solid line shows the linear fit, intercepting the plot origin, based on Eq. (25).

latter result is very close to our earlier finding,<sup>8</sup> as well as to the values of 8160 m/s and 8020 m/s reported in literature.<sup>1,11</sup>

## Conclusions

We have presented our comprehensive studies of CAP generation and detection in a bulk GaN single crystal, using a time-resolved, femtosecond, two-color pump/probe technique. We theoretically predicted and experimentally confirmed that the CAP transients, in our case, were initiated by electronic stress induced at the GaN crystal surface by generation of free carriers, photoexcited by  $\sim 100$ -fs pump UV pulses. Using far-below-bandgap,  $\sim 100$ -fs-wide probe pulses with a very long penetration depth into the GaN crystal, we monitored the CAP propagation that manifested itself as regular, single-frequency oscillations superimposed on the probe  $\Delta R/R$  signal. The amplitude of the oscillations was of the order of  $10^{-5}$  to  $10^{-6}$ , and within our  $\sim 450$ -ps time window, we observed no signal attenuation. We also found that the CAP oscillation amplitude was dependent only on the pump-photon energy and, in general, followed the spectral dependence of the GaN optical absorption coefficient, as was predicted by our theoretical model. For the entire tuning range of our NIR probe photons, the phase of the CAP oscillations was constant and the CAP frequency was dispersionless (proportional to the probe  $k_0$ ) with the slope corresponding to  $v_s = 8002 \pm 22$  m/s, the speed of sound in GaN. Very good agreement between our theoretical modeling and experimental results demonstrates that our theoretical approach, which is a generalization of the Thomsen model,<sup>7</sup> comprehensively describes the dynamics of CAP's in bulk materials, generated by the strong, above-the-bandgap optical excitation and synchronously probed using almost nonattenuated probe pulses. Thus, our above-bandgap pump and far-below-bandgap probe experimental approach makes it possible to successfully generate nanoscale acoustic waves at the surface of bulk semiconductors and, simultaneously, to nondestructively probe the material's structure deeply under its surface. The two-color femtosecond spectroscopy technique, implemented here for the studies of GaN, should be very promising in producing and detecting CAP waves in a large variety of bulk semiconducting materials.

## ACKNOWLEDGMENT

The authors would like to thank D. Wang and A. Cross for many valuable discussions throughout the course of this work. S. Wu acknowledges support from the Frank Horton Graduate Fellowship Program. This work was

supported by the U.S. Department of Energy Office of Inertial Confinement Fusion under Cooperative Agreement No. DE-FC52-92SF19460, the University of Rochester, and the New York State Energy Research and Development Authority. The support of DOE does not constitute an endorsement by DOE of the views expressed in this article.

## REFERENCES

1. Y.-K. Huang *et al.*, Appl. Phys. Lett. **79**, 3361 (2001).
2. R. L. Liu *et al.*, Phys. Rev. B **72**, 195335 (2007).
3. C.-K. Sun, J.-C. Liang, and X.-Y. Yu, Phys. Rev. Lett. **84**, 179 (2000).
4. Ü. Özgür, C.-W. Lee, and H. O. Everitt, Phys. Status Solidi B **228**, 85 (2001).
5. G. D. Sanders and C. J. Stanton, Phys. Rev. B **64**, 235316 (2001).
6. O. Matsuda *et al.*, Phys. Rev. B **71**, 115330 (2005).
7. C. Thomsen *et al.*, Phys. Rev. B **34**, 4129 (1986).
8. S. Wu, P. Geiser, J. Jun, J. Karpinski, J.-R. Park, and R. Sobolewski, Appl. Phys. Lett. **88**, 041917 (2006).
9. G. Yu *et al.*, Appl. Phys. Lett. **70**, 3209 (1997).
10. S. Wu, P. Geiser, J. Jun, J. Karpinski, D. Wang, and R. Sobolewski, J. Appl. Phys. **101**, 043701 (2007).
11. C. Deger *et al.*, Appl. Phys. Lett. **72**, 2400 (1998).
12. V. Bougrov *et al.*, in *Properties of Advanced Semiconductor Materials: GaN, AlN, InN, BN, SiC, SiGe*, edited by M. E. Levinshtein, S. L. Rumyantsev, and M. Shur (Wiley, New York, 2001), Chap. 1, pp. 1–30.
13. M. Leszczynski *et al.*, J. Phys. D: Appl. Phys. **28**, A149 (1995).
14. W. Qian, M. Skowronski, and G. S. Rohrer, in *III-Nitride, SiC, and Diamond Materials for Electronic Devices*, edited by D. K. Gaskill, C. D. Brandt, and R. J. Nemanich, Mat. Res. Soc. Symp. Proc. Vol. 423 (Materials Research Society, Pittsburgh, PA, 1996), pp. 475–486.
15. S. L. Chuang and C. S. Chang, Phys. Rev. B **54**, 2491 (1996).
16. G. Tamulaitis *et al.*, Phys. Status Solidi C **3**, 1923 (2006).
17. S. N. Nakamura and G. Fasol, *The Blue Laser Diode: GaN Based Light Emitters and Lasers* (Springer, Berlin, 1997).
18. J. Karpinski, J. Jun, and S. Porowski, J. Cryst. Growth **66**, 1 (1984).

---

# Subsurface Damage and Microstructure Development in Precision Microground Hard Ceramics Using MRF Spots

## Introduction

Chemical vapor-deposited (CVD) silicon carbide ( $\text{Si}_4\text{C}/\text{SiC}$ ), polycrystalline alumina ( $\text{Al}_2\text{O}_3/\text{PCA}$ ), and aluminum oxynitride ( $\text{Al}_{23}\text{O}_{27}\text{N}_5/\text{ALON}$ ) polycrystalline ceramics display a great potential for advanced optical applications in severe environments that require high hardness, high toughness, and excellent thermal properties. These materials are nominally fully dense; therefore, there is growing interest in grinding and ultimately polishing them to nanometer levels of surface microroughness.

Grinding of ceramic materials usually involves the use of metal- or resin-bonded diamond abrasive wheels.<sup>1</sup> The material-removal mechanism can be described by indentation fracture mechanics, where removal is caused by multiple indentation events.<sup>2,3</sup> Two crack systems extend from the plastic deformation zone induced by the indentation: median/radial and lateral cracks.<sup>2</sup> For a given process, lateral cracks control the extent of material removal,<sup>4,5</sup> while the extensions of median/radial cracks are commonly associated with subsurface damage (SSD),<sup>6</sup> which contributes to the degradation of the materials' strength.<sup>2</sup>

For optical applications, SSD can be the source of component instability (e.g., surface stress) and contamination. Polishing abrasives embedded in cracks can lead to laser-induced damage, and thermal cycling can result in component fracture.<sup>7-9</sup> Therefore, determination of SSD depth is critical for high-quality optics. Unfortunately, SSD from grinding is often masked by a deformed surface layer that is smoothed or smeared over the part surface.<sup>9-11</sup> For polycrystalline ceramics, this layer may also consist of pulverized grains or powder. The thickness of this deformed layer varies along the ground surface because of the nonhomogeneity of the composite and the nonuniform distribution of diamond abrasives on the grinding wheel.<sup>12</sup> Therefore, it is valuable to develop new analytical techniques for understanding the damaged surface left from grinding and how it extends into the subsurface for these optical ceramics.<sup>9,10</sup>

Different techniques for estimating SSD depth induced by grinding have been pursued. Randi *et al.*<sup>13</sup> reviewed both non-destructive and destructive techniques to evaluate SSD in brittle materials. Nondestructive methods include transverse electron microscopy, x-ray diffractometry, Raman spectroscopy, optical microscopy, photoluminescence, and the use of ultrasound for ground ceramic materials. Destructive techniques include taper polishing, cleavage, sectioning, ball dimpling, and spotting with magnetorheological finishing (MRF). These destructive techniques are ultimately followed by microscopy or diffractive-based techniques to observe and measure SSD depth.

One recent example of a nondestructive technique is light scattering, as described by Fine *et al.*,<sup>7</sup> whose results were confirmed by the sectioning technique. Another recent study by Wang *et al.*<sup>8</sup> showed how the measurement of the quasi-Brewster angle (qBAT) as a function of wavelength could be used to estimate SSD depth for polished  $\text{CaF}_2$  (111) surfaces. The MRF spot technique, as described by Randi *et al.*,<sup>13</sup> was used by Wang *et al.*<sup>8</sup> to validate their results.

Examples of sectioning techniques include the work by Xu *et al.*<sup>14</sup> done on polycrystalline alumina scratched by a single diamond, or Kanematsu,<sup>10</sup> who visualized the morphology of SSD induced by grinding on silicon nitride. His approach included a combination of taper-polishing and plasma-etching techniques, finally observing SSD using scanning electron microscopy (SEM). In addition, dye impregnation was used to identify the crack morphology of previously ground samples that were subsequently broken using a flexure test.<sup>10</sup> Miller *et al.*<sup>9</sup> and Menapace *et al.*<sup>5,15</sup> utilized MRF computer numerically controlled (CNC) machines with raster polishing capabilities to study the distribution of SSD in larger, polished fused-silica parts by fabricating a wedge.

SSD depth can also be estimated by correlating SSD depth to the grinding-induced surface microroughness, or by correlating SSD depth to the size of grinding or polishing abrasives. Preston<sup>16</sup> showed that surface microroughness was three to four

times the SSD depth, by comparing polished and ground glass microscope slides in the early 1920s. In the 1950s Aleinikov<sup>17</sup> expressed the proportionality factor to be  $\sim 4$  for optical glasses and ceramics. Hed *et al.*<sup>18</sup> extended Aleinikov's work using bound-abrasive tools (diamond and boron carbide), finding that the ratio between SSD depth and peak-to-valley (p-v) surface microroughness (measured using a contact profilometer) for Zerodur, fused silica, and BK-7 glass was  $\sim 6.5$ , a much higher value than previous results. For a large variety of optical glasses ground with bound-abrasive diamond tools, Lambropoulos *et al.*<sup>19</sup> estimated SSD depth to be less than two times the p-v surface microroughness (from areal measurements using a white-light interferometer). In more recent work, Randi *et al.*<sup>13</sup> found the ratio between p-v microroughness (from areal measurements using a white-light interferometer) and SSD to be 1.4 for some optical single crystals ground with diamond-bonded tools, where SSD was measured directly by combining MRF spotting and microscopy techniques. Using the MRF-based technique described here, we demonstrated that, for nonmagnetic nickel-based tungsten carbides (WC-Ni—a challenging composite for optical applications), there is a strong positive correlation between p-v surface microroughness (from areal measurements using a white-light interferometer) and SSD depth for rough-ground surfaces.<sup>20</sup> The application of this technique to magnetic cobalt-based tungsten carbides (WC-Co) was also successful.<sup>21</sup> In all work cited above, it is critical to be aware of the instruments used to characterize surface roughness since different instruments produce different surface-roughness values, due to their different lateral scale-length capabilities.

SSD was also found to be a function of abrasive size used in the controlled grinding stages for fabrication of precision optics, as discussed by Lambropoulos<sup>22</sup> for a variety of optical glasses and glass ceramics. In practice, by reducing the abrasive size with each grinding cycle, the plastically deformed material is removed, reducing the residual stresses associated with the indentation events, and subsequently reducing the initiation of cracks within the plastic zone.<sup>4</sup> This suggests that, by gradually reducing abrasive size, SSD can be minimized with every subsequent grinding step.

We present here a procedure for estimating SSD depth induced by deterministic microgrinding of hard polycrystalline optical ceramics with diamond-bonded tools. This estimate comes from tracking the evolution of surface microroughness (measured using a white-light interferometer) with the amount of material removed by multiple MRF spots (measured using a contact profilometer) of increasing depth into the surface. In

addition to extending our p-v microroughness/SSD correlation to hard ceramics, this technique also reveals information about the specimen microstructure (i.e., grain size), mechanical properties (i.e., hardness and fracture toughness), and the grinding conditions (i.e., abrasive size used), from extended spotting with the MRF process.

## Experimental Procedure

### 1. Materials

Samples were obtained from the following sources: three ALON (Surmet Corp., MA, Lot 1472, April 2006) disks (40 mm in diameter  $\times$  15 mm thick), two PCA (commercial manufacturer) disks (40 mm in diameter  $\times$  2.5 mm thick), and three CVD SiC (Rohm and Haas Company, Advanced Materials, MA) disks (76 mm in diameter  $\times$  11.5 mm thick). Grain-size ranges were 150 to 250  $\mu\text{m}$  for ALON, submicron size for PCA, and 5 to 10  $\mu\text{m}$  for CVD SiC.

### 2. Mechanical Properties (Hardness and Fracture Toughness)

Hardness measurements were taken on a Tukon micro-indenter equipped with a Vickers diamond indenter and a built-in microscope ( $\times 50$  objective). A constant dwell time of 15 s was used, with a nominal indentation load of 1 kgf (9.8 N). Averaging was performed on the diagonals of five to ten random indents on the surface.

In the case of ALON, individual grains were easily distinguished, allowing placement of indentations in the middle of individual grains. There were no grain boundaries observable for CVD SiC and PCA using the microscope. For all of the materials tested, indentations were randomly placed on specimen surfaces, avoiding large pores and/or inclusions.

Fracture toughness  $K_{IC}$  values were calculated from the observed radial cracks produced at the indentation corners using the Evans correlation.<sup>23</sup> The relevant physical and mechanical properties are listed in Table 110.IV.

### 3. Grinding Experiments

All samples were processed under the same conditions using deterministic microgrinding. The first set of grinding experiments was performed on a CNC grinding machine<sup>25</sup> using a contour-tool grinding configuration for flat surfaces [see Fig. 110.34(a)], with three different diamond tools: rough, medium, and fine (40- $\mu\text{m}$ , 10- to 20- $\mu\text{m}$ , and 2- to 4- $\mu\text{m}$  grit size, respectively). Both the rough and medium tools had a bronze matrix while the fine tool matrix was resin. To avoid tak-

ing the part off the machine between operations, the tools were trued and dressed in advance using  $Al_2O_3$  dressing sticks that were 320 or 800 grit (29- to 32- $\mu m$  and 9- to 12- $\mu m$  grit size, respectively). Table 110.V lists the grinding conditions used.

For PCA an additional grinding experiment was performed because of the large form error on the part surface from grind-

ing using the previous contour configuration. These experiments were completed on a CNC grinding machine<sup>26</sup> using a ring-tool grinding configuration for flat surfaces [see Fig. 110.34(b)]. Grinding was done using rough and medium diamond tools (65- $\mu m$  and 10- to 20- $\mu m$  grit size, respectively). Both tools had a bronze matrix, and dressing procedures were performed as discussed above. Table 110.V lists the grinding conditions used.

Table 110.IV: Physical and mechanical properties of hard ceramics listed by increasing Vickers hardness and fracture toughness.<sup>(a)</sup>

Material ID	Density $\rho$ (g/cm <sup>3</sup> )	Grain size ( $\mu m$ )	Young's modulus $E$ (GPa)	Vickers hardness $H_V$ (GPa)	Fracture toughness $K_c$ (MPa $\sqrt{m}$ ) <sup>(b)</sup>
ALON ( $Al_{23}O_{27}N_5$ )	3.69 <sup>(c)</sup>	150 to 250	334	15.4 $\pm$ 0.3 <sup>(d)</sup>	2.7 $\pm$ 0.2
PCA ( $Al_2O_3$ )	3.99 <sup>(e)</sup>	<1	400 <sup>(f)</sup>	21.6 $\pm$ 0.3 <sup>(g)</sup>	3.3 $\pm$ 0.1
CVD SiC ( $Si_4C$ )	3.21	5 to 10	466	25.0 $\pm$ 0.1 <sup>(g)</sup>	5.1 $\pm$ 0.3

(a) Catalog values, unless otherwise specified.  
 (b) Calculated using the Evans correlation.<sup>23</sup>  
 (c) Density may vary slightly depending on the stoichiometry.  
 (d) Averaging ten Vickers indentations at 1 kgf.  
 (e) Using Archimedes' water immersion principles.<sup>24</sup>  
 (f) Calculated from measurement using ultrasonic tests and density values. Data were averaged for two PCA disks (~30 mm in diameter  $\times$  ~1 mm thick) polished on both sides.  
 (g) Averaging five Vickers indentations at 1 kgf.

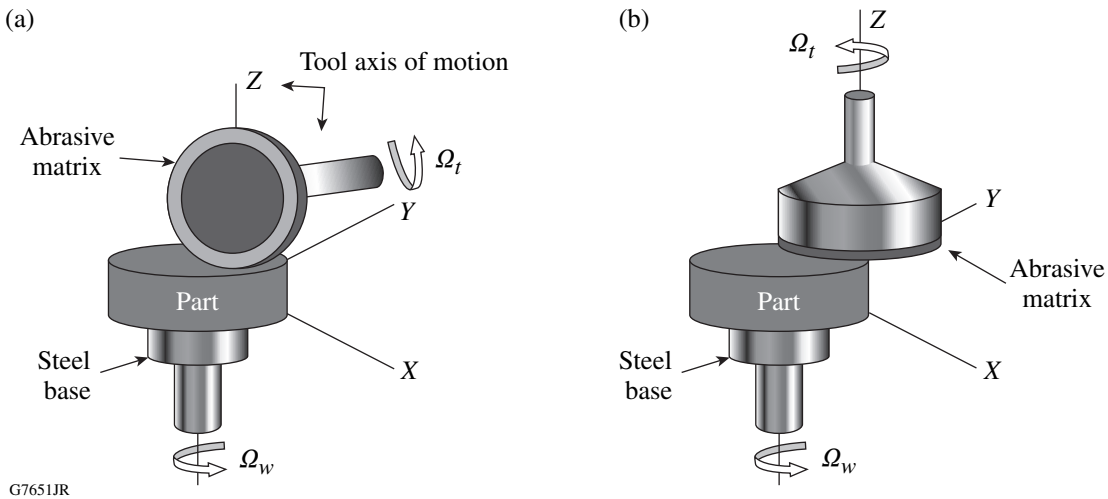


Figure 110.34 Schematics of the two grinding configurations used in our experiments: (a) contour and (b) ring-tool configurations.

Table 110.V: Grinding conditions used in a single pass.<sup>(a)</sup>

Tool grit size ( $\mu\text{m}$ )	Depth of cut ( $\mu\text{m}$ )	In-feed (z axis) (mm/min)	Duration of single pass	Cross-feed (x axis) (mm/min)	Duration of single pass (min)
Contour tool grinding configuration. <sup>25</sup>					
40 <sup>(b)</sup>	100	0.5	12 (s)	1.0	30 to 40
10 to 20 <sup>(b)</sup>	20	0.5	2.4 (s)	1.0	30 to 40
2 to 4 <sup>(c)</sup>	5	0.5	0.6 (s)	5.0	6 to 8
Ring tool grinding configuration. <sup>26</sup>					
65 <sup>(b)</sup>	100	0.1	~20 (min)	NA	NA
10 to 20 <sup>(b)</sup>	30	0.01	~45 (min)	NA	NA
<sup>(a)</sup> The following parameters remained constant: Wheel speed, $\Omega_t = 6800$ rpm for contour tool grinding; $\Omega_t = 3000$ rpm for ring tool grinding; work spindle speed, $\Omega_w = 100$ rpm in both cases. <sup>(b)</sup> Bronze bonded, 75 diamond concentration. <sup>(c)</sup> Resin bonded, 75 diamond concentration.					

Before all grinding experiments, each workpiece was attached to a steel base with hot wax and then placed in the grinding machine parallel to the tool axis of rotation. Water–oil emulsion coolant<sup>27</sup> was delivered to the tool/workpiece interface to avoid burnout and thermal damage. In the case of the contour grinding configuration, grinding was done with two passes for each tool; i.e., the total material removed per tool was 200, 40, and 10  $\mu\text{m}$  (rough, medium, and fine tools, respectively). No subsequent “spark-out” passes were performed. For example, the fine grinding was done only after the part had gone through two-pass cycles with the rough and medium tools. Finally, the workpieces were cleaned using acetone. For ring-tool grinding, multiple tool passes were performed until material was evenly removed from the surface.

#### 4. Spotting of Ground Surfaces

Magnetorheological finishing (MRF)<sup>28,29</sup> is a commercial polishing process for the manufacturing of precision optics. We used MRF spotting, with a commercial CNC machine,<sup>30</sup> in our experiment to estimate the depth of subsurface damage induced by grinding. For all of our experiments, MRF spots were polished onto the ground surface of a nonrotating part, by lowering the part surface into contact with a rotating magnetic fluid ribbon. The MRF fluid used was a commercial product<sup>31</sup> that consisted of an aqueous mixture of nonmagnetic nanodiamond abrasives, magnetic carbonyl iron, water, and stabilizers. Machine parameters such as the magnetic-field strength (~2 to 3 kG), wheel speed (250 rpm), pump speed (125 rpm), ribbon height (1.6 mm), and depth of the part penetrating into the ribbon (0.3 mm) were kept constant and the spotting time

was varied. Spotting was done on previously rough-ground, medium-ground, and fine-ground surfaces of each material. Multiple spots with time durations of 1 to 8, 12, and 16 min were taken on subsets of the ground surfaces of ALON and CVD SiC, whereas in the case of the PCA, multiple spots with time durations of 6, 12, 24, 48, and 96 min were taken as described in **Surface Evaluation from the Spotting Experiments** (p. 103).

#### 5. Microscopy of Processed Surfaces

Surfaces were studied using a contact profilometer, a white-light interferometer, a scanning electron microscope (SEM), and an atomic force microscope (AFM). Before the surfaces were analyzed, the samples were ultrasonically cleaned in acetone (30 min at room temperature), then rinsed with alcohol, and finally dried using a nitrogen gun.

Metrology was conducted as follows:

- A stylus profilometer<sup>32</sup> was used to perform 3-D scans of the MRF spots, which were then used to extract the spots’ physical dimensions, i.e., spot volume, peak removal depth, and spot profile. The stylus tip is a cone with a 60° angle and a 2- $\mu\text{m}$  spherical tip radius of curvature. The instrument has a 12-nm vertical resolution, and the lateral resolution is about the size of the tip.
- Average microroughness data [peak-to-valley (p–v) and root mean square (rms)] were obtained with a noncontacting white-light interferometer<sup>33</sup> over five 350 × 250- $\mu\text{m}^2$  areas

randomly distributed across ground areas and within MRF spots as described in **Surface Evaluation from the Spotting Experiments** (p. 103). This instrument has a lateral resolution of  $\sim 1 \mu\text{m}$  and a vertical resolution of  $\sim 0.3 \text{ nm}$ . The motorized XY stage and field-of-view stitching software allow this instrument to be programmed to measure a large area at high resolution.

- The morphologies of the processed surfaces following grinding, and for selected MRF spots, were analyzed using a field emission SEM.<sup>34</sup> The preferred imaging configuration was a mix signal of the in-lens and in-chamber secondary electron detectors. Surfaces of ground and spotted CVD SiC material were not etched or coated prior to SEM. Imaging of the nonconductive materials (i.e., PCA and ALON) was also performed without etching or application of a conductive coating, using a low beam voltage (1.5 to 0.7 kV), at an  $\sim 3\text{-mm}$  working distance.
- Additional surface scans for selected spots were taken on the AFM<sup>35</sup> over three  $10 \times 10\text{-}\mu\text{m}^2$  areas randomly distributed within spots where the deepest point of fluid penetration (ddp) occurred, as discussed in **Surface Evaluation from**

**the Spotting Experiments** (p. 103). Silicon tips with tip radii of approximately 10 nm were used. The lateral image resolution can be as small as the tip radius (5 to 15 nm) and the instrument vertical noise resolution is less than  $0.5 \text{ \AA}$ .

## Experimental Results

### 1. Surface Microroughness and Surface Morphology from Grinding

Surface microroughness data for all materials after each grinding stage were taken using the white-light interferometer. As expected, surface microroughness decreased with decreasing diamond abrasive size. Using the light microscope<sup>36</sup> we observed pitting on the ground surfaces, with no traces of grain boundaries for all the materials tested, as seen in Fig. 110.35. The p-v surface microroughness varied from  $\sim 14.5 \mu\text{m}$  (ALON) to  $\sim 3.7 \mu\text{m}$  [CVD SiC; see Fig. 110.35(a)] after grinding with the rough tool ( $40\text{-}\mu\text{m}$  grit size), from  $\sim 12 \mu\text{m}$  (ALON) to  $\sim 3.5 \mu\text{m}$  (CVD SiC) for the medium tool ( $10\text{-}$  to  $20\text{-}\mu\text{m}$  grit size), and from  $\sim 4 \mu\text{m}$  [ALON; see Fig. 110.35(b)] to  $\sim 0.4 \mu\text{m}$  [CVD SiC; see Fig. 110.35(c)] for the fine tool ( $2\text{-}$  to  $4\text{-}\mu\text{m}$  grit size). Surface microroughness for PCA was  $\sim 9 \mu\text{m}$  [see Fig. 110.35(d)] with the medium ring tool ( $10\text{-}$  to  $20\text{-}\mu\text{m}$  grit size).

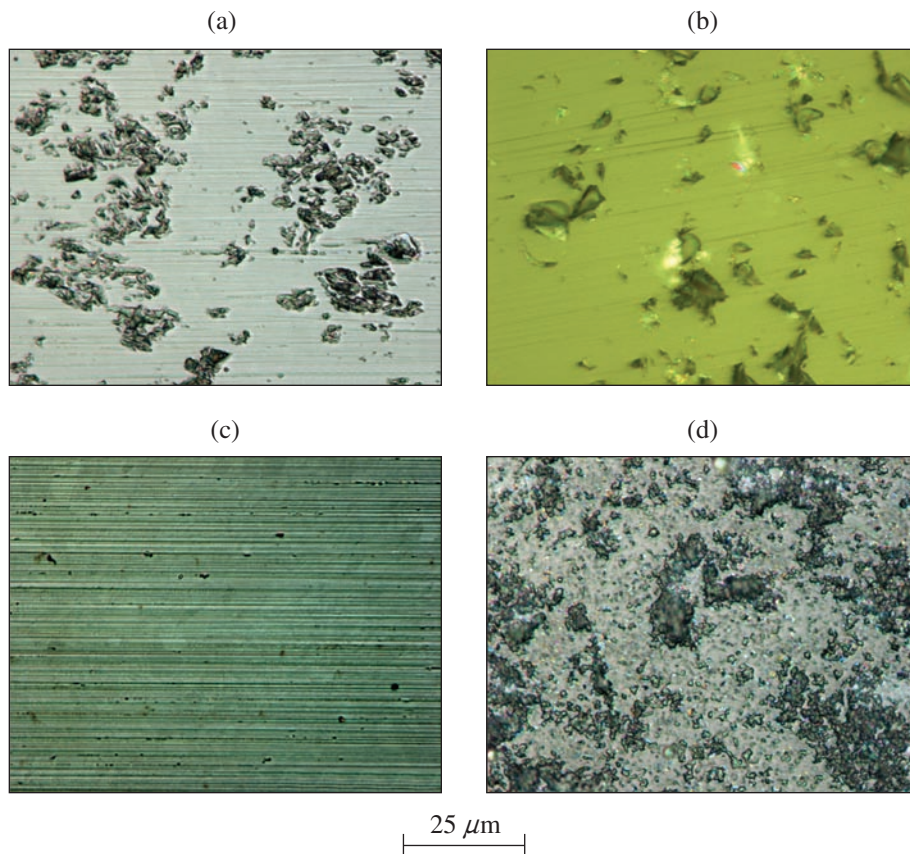


Figure 110.35

Light microscope images of ground surfaces: (a) rough-ground CVD SiC (5- to  $10\text{-}\mu\text{m}$  grain size,  $40\text{-}\mu\text{m}$  tool grit size with contour configuration,  $\sim 4\text{-}\mu\text{m}$  p-v); (b) fine-ground ALON ( $150\text{-}$  to  $300\text{-}\mu\text{m}$  grain size,  $2\text{-}$  to  $4\text{-}\mu\text{m}$  tool grit size with contour configuration,  $\sim 4\text{-}\mu\text{m}$  p-v); (c) fine-ground CVD SiC ( $5\text{-}$  to  $10\text{-}\mu\text{m}$  grain size,  $2\text{-}$  to  $4\text{-}\mu\text{m}$  tool grit size with contour configuration,  $\sim 0.4\text{-}\mu\text{m}$  p-v); (d) medium-ground PCA (submicron grain size,  $10\text{-}$  to  $20\text{-}\mu\text{m}$  tool grit size with ring configuration,  $\sim 8.5\text{-}\mu\text{m}$  p-v).

G7652JRC

By using the SEM's high-magnification capabilities we examined the morphologies of the ground surfaces with greater detail. Figure 110.36(a) shows the morphology of the rough-ground ALON, where the material microstructures, i.e., grain boundaries, are not visible. By using high magnification, Fig. 110.36(b) shows that the removal mechanism involved fracture. Figure 110.36(c) shows that for CVD SiC, the rough-ground surface is pitted, with the surrounding surface relatively smooth. Using higher magnification, Fig. 110.36(d) shows that the pit lengths, approximately 5  $\mu\text{m}$  long, are comparable to the average grain size (5 to 10  $\mu\text{m}$ ) of this CVD SiC material.

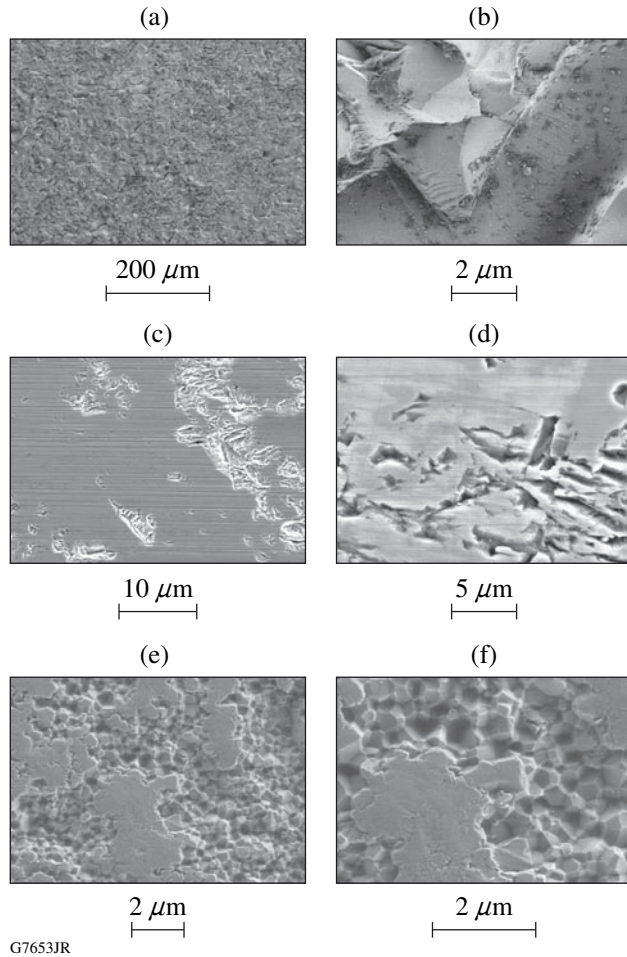


Figure 110.36 Morphology of the as-ground surfaces using SEM with different magnifications: (a),(b) ALON ground with contour configuration, 40- $\mu\text{m}$  tool grit size, and  $\sim 14.5\text{-}\mu\text{m}$  p-v, low and high magnification, respectively, taken using low beam voltage (1 kV), at a 5-mm working distance; (c),(d) CVD SiC ground with contour configuration, 40- $\mu\text{m}$  tool grit size,  $\sim 4\text{-}\mu\text{m}$  p-v, low and high magnification, respectively, taken using nominal beam voltage (10 kV), at a 10-mm working distance; and (e),(f) PCA ground with ring configuration, 10- to 20- $\mu\text{m}$  tool grit size,  $\sim 8.5\text{-}\mu\text{m}$  p-v, low and high magnification, respectively, taken using low beam voltage (1.5 kV), at a 3-mm working distance.

Examination of the PCA surface in Fig. 110.36(e) shows that the deformed layer induced by grinding covers/masks the grains and any SSD, for PCA. Using higher magnification, Fig. 110.36(f) shows the exposed PCA subsurface where it appears that single grains pulled out, leaving craters of the order of 0.2 to 0.4  $\mu\text{m}$  wide.

## 2. Surface Evaluation from the Spotting Experiments

MRF spots of increasing time duration were taken on all ground surfaces. Figure 110.37(a) shows a typical 3-D map generated with a profilometer for an 8-min MRF polishing spot taken on a rough-ground CVD SiC surface. After using the software to remove form figure errors (e.g., tilt and curvature), we calculated the physical properties such as volume and maximum amount of material removed by the MRF spot (i.e., spot depth). The volumetric removal rates for ALON, CVD SiC, and PCA using the MRF operating conditions described previously were found to be 0.020, 0.006, and 0.002  $\text{mm}^3/\text{min}$ , respectively, from averaging the results of four spots.

The area enclosed by the white ellipse in Fig. 110.37(a) constitutes the region of maximum removal within the spot, where the depth of deepest penetration (ddp) into the subsurface

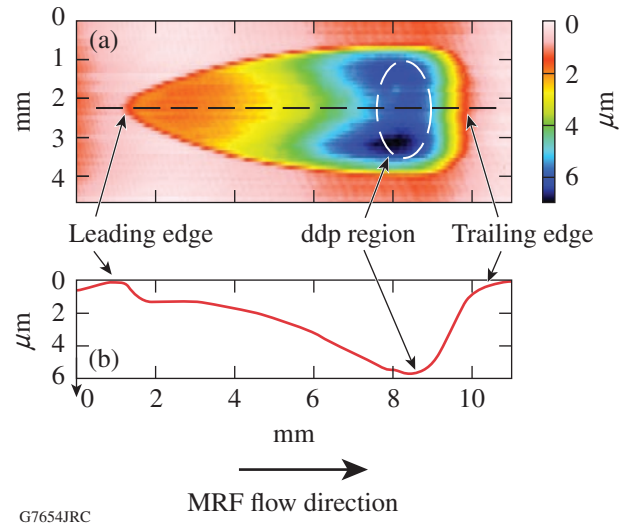


Figure 110.37 (a) 3-D image of an MRF spot taken with a contact stylus profilometer on rough-ground CVD SiC for 8 min. Arrows indicate the spot's leading edge (where an MRF ribbon first contacts the material), the spot's ddp region, identified by an ellipse (deepest point of part penetration into the MRF fluid ribbon), and the spot's trailing edge. The fluid flow direction is from left to right. (b) Spot profile extracted from a line scan through the center of the 3-D map (indicated by a dashed line). The distance between the trailing edge and the ddp region is  $\sim 2$  mm in the horizontal direction. The spot depth reaches  $\sim 6$   $\mu\text{m}$  in the region sampled with the line scan.

occurs. The ddp in Fig. 110.37(a) has some asymmetry with respect to the spot center profile line [shown in Fig. 110.37(b)], in this case exhibiting a variation of  $\pm 0.6 \mu\text{m}$ . This feature is typically encountered for many of the longer-time-duration spots examined in this work. It could be due, in part, to subtle misalignments of the plane of a part surface with respect to the MRF ribbon. Figure 110.37(b) illustrates how we extract the spot center profile from the 3-D map to establish the location of the ddp region relative to the trailing edge for roughness measurements.

Figure 110.38(a) shows a 3-D map of a different spot taken on a rough-ground CVD SiC surface transverse to the MRF flow direction (as indicated by an arrow in the figure), with the

white-light interferometer in stitching mode. Figures 110.38(b) and 110.38(c) give 3-D maps ( $0.3 \times 0.3 \text{ mm}^2$ ) of the rough-ground surface and within the ddp, extracted from the map of Fig. 110.38(a), respectively. Figures 110.38(d) and 110.38(e) show line scans, or 2-D profiles, extracted from Figs. 110.38(b) and 110.38(c) (as indicated by the arrows), respectively. These line scans show the significant roughness reduction from  $\sim 1.4\text{-}\mu\text{m}$  p-v [ $\sim 100\text{-nm}$  rms; Fig. 110.38(d)] for the ground surface to  $\sim 95\text{-nm}$  p-v [ $\sim 18\text{-nm}$  rms; Fig. 110.38(e)] achieved inside the MRF spot, in agreement with the areal micro-roughness values, which vary from  $\sim 3.2\text{-}\mu\text{m}$  p-v [ $\sim 99\text{-nm}$  rms; Fig. 110.38(b)] on the ground surface and  $\sim 170\text{-nm}$  p-v [ $\sim 19\text{-nm}$  rms; Fig. 110.38(c)] within the spot ddp. Note that the discrepancy between the line scans and the areal data

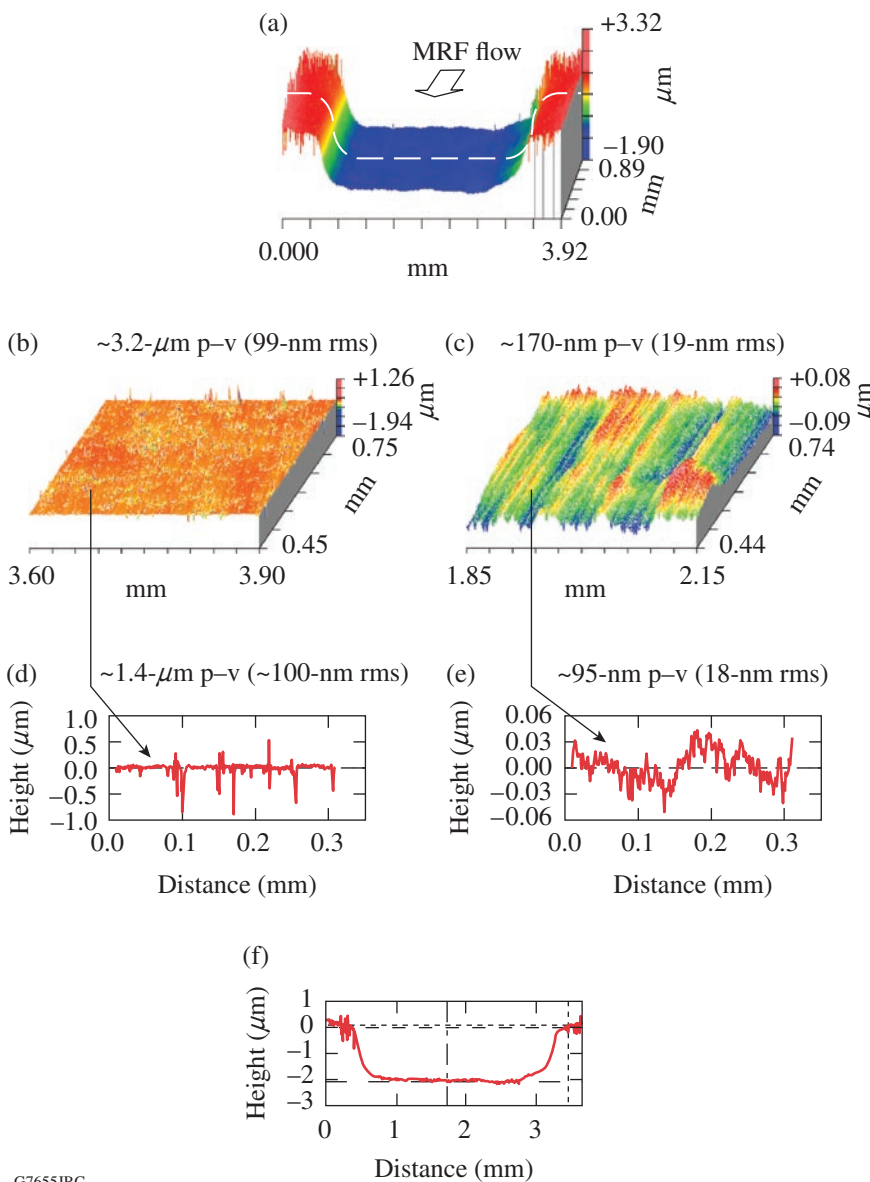


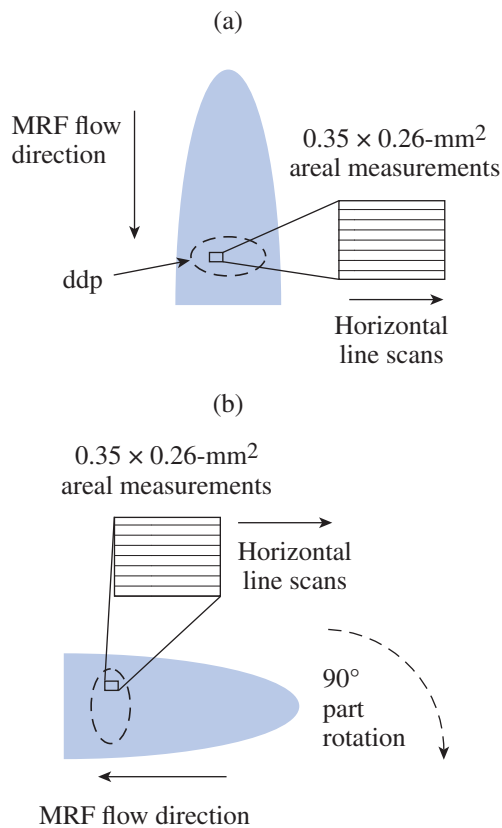
Figure 110.38

Scans taken on rough-ground CVD SiC, spotted for 3 min: (a) 3-D map done with the white-light interferometer in stitching mode, transverse to the MRF flow (see arrow indicating the MRF flow direction); (b),(c) areal maps ( $0.3 \times 0.3 \text{ mm}^2$ ) of microroughness on the ground surface and within the spot ddp, respectively; (d) line scan of the ground surface, taken from the center of (b); (e) line scans within the ddp region transverse to the MRF flow direction, taken from the center of (c) (as indicated by the arrows); and (f) line scan of the spot-width profile (indicated by a dashed white line in the 3-D map) in (a).

G7655JRC

comes from the larger areas sampled with the latter method. Another discrepancy between the 3-D map and line scans in Fig. 110.38 is associated with the spot depth. The vertical scale in Fig. 110.38(a) indicates the overall areal p-v roughness variations of  $\sim 5.2 \mu\text{m}$ , which artificially indicates a spot depth of that scale because it includes the highest peaks on the rough surface. However, when we examine single line scans of the spot width profile [represented by a dashed line in Fig. 110.38(a)], the spot depth is shown to be  $\sim 2 \mu\text{m}$  [see Fig. 110.38(f)].

After the location of a given spot's ddp was identified [as described in Fig. 110.37(b)], areal surface microroughness measurements were taken using the white-light interferometer at five random locations within the ddp region over areas of  $0.35 \times 0.26 \text{ mm}^2$  as seen schematically in Fig. 110.39(a). In



G7656JRC

Figure 110.39

Schematic diagram of the procedure used for surface microroughness measurements within MRF spots. The dashed ellipse represents the ddp region. The rectangle within the ddp represents one of five random sites over which surface roughness was measured. (a) First orientation of the spot for generating line scans perpendicular ( $\perp$ ) to the MR fluid flow direction, and (b) after rotating the part  $90^\circ$  to generate line scans parallel ( $\parallel$ ) to the MR fluid flow direction.

addition, horizontal line scans were taken perpendicular ( $\perp$ ) to the MRF flow direction. Then, the part was rotated by  $90^\circ$  and remeasured so that horizontal line scans parallel ( $\parallel$ ) to the MRF flow direction were also obtained, as seen in Fig. 110.39(b). This procedure is necessary because the interferometer analog camera creates images with a horizontal raster pattern.

Surface microroughness data taken on initial ground surfaces and in ddp areas for long-time-duration spots are listed in Tables 110.VI(a)–110.VI(c). The areal data represent averages of 5 random measurements, while the values for the line scans ( $\perp$  and  $\parallel$ ) represent averages of 50 line scans. The amount of material removed in each spot, or the spot maximum depth, is reported for measurements done using the contact profilometer, as described in the text that discusses Fig. 110.37(a).

Tables 110.VI(a)–110.VI(c) summarize the results of grinding and spotting experiments (the complete set of experimental data can be found elsewhere<sup>37</sup>). The evolution of microroughness with the amount of material removed by the MRF spot indicates that by removing an optimal amount of material from the as-ground surface, p-v surface microroughness was significantly reduced. This observation is valid for all initial surface conditions: rough, medium, and fine ground. For example, in the case of ALON, the initial surface microroughness values were  $\sim 14.5\text{-}\mu\text{m}$  p-v ( $\sim 1.5\text{-}\mu\text{m}$  rms), while after removing  $\sim 11 \mu\text{m}$  with the MRF process, surface microroughness decreased to  $\sim 1.2\text{-}\mu\text{m}$  p-v ( $\sim 0.09\text{-}\mu\text{m}$  rms). When an additional  $\sim 13 \mu\text{m}$  of material were removed, surface microroughness decreased to  $\sim 1.1 \mu\text{m}$  ( $\sim 0.07\text{-}\mu\text{m}$  rms). In addition, we found differences in microroughness values between areal and line scans, either in a direction perpendicular ( $\perp$ ) or parallel ( $\parallel$ ) to the MRF flow. For example, in the case of CVD SiC, the initial rough-ground surface microroughness values were  $\sim 3.7\text{-}\mu\text{m}$  p-v ( $\sim 0.11\text{-}\mu\text{m}$  rms), whereas using line scans, surface microroughness values were  $\sim 1.5\text{-}\mu\text{m}$  p-v ( $\sim 0.1\text{-}\mu\text{m}$  rms). [Note that there is no preferred directionality to the ground surface.] After removing  $\sim 1.7 \mu\text{m}$  with the MRF process, surface microroughness decreased to  $\sim 0.11\text{-}\mu\text{m}$  p-v ( $\sim 0.02\text{-}\mu\text{m}$  rms) in a direction perpendicular ( $\perp$ ) to the flow, compared to  $\sim 0.06\text{-}\mu\text{m}$  p-v ( $\sim 0.01\text{-}\mu\text{m}$  rms) measured parallel ( $\parallel$ ) to the flow direction. Similar observations can be made in the case of PCA.

## Discussion

In this work MRF spots were placed on previously ground hard optical ceramics, exposing the subsurface without introducing new damage. By removing several microns of material (proportional to the initial p-v microroughness in the as-ground state), surface roughness was significantly reduced. With the

removal of additional material (i.e., using longer MRF spotting time), we observed that roughness continued to decrease or to slightly increase.

These results suggest that, after examining the evolution of surface roughness within the spots as a function of the amount of material removed (see Fig. 110.40), two stages can be identified: a stage where removal of the initial grinding damage occurs, and a stage where removal shows the development of a texture relating to the interaction between MRF and the material surface. In the first stage, surface roughness resulting from deformation and fracture by grinding is removed, starting with the initial surface condition and ending when the surface

roughness reaches a low value after spotting with MRF. Here the improvement in surface condition is best characterized by the drop in areal p-v roughness, a measurement that captures all features over a reasonably large area.

As seen in Fig. 110.40, the areal p-v for the initially rough-ground ALON [Fig. 110.40(a)], rough-ground CVD SiC [Fig. 110.40(b)], and medium-ground PCA [Fig. 110.40(c)] falls from ~14.5, ~3.7, and ~9 μm to ~1.2, ~0.20, and ~0.25 μm, with ~11, ~1.7, and ~9 μm removed in the first stage, respectively. Beyond this point, differences become apparent in the second stage, depending on how the surface roughness is examined.

Table 110.VI(a): Selected summary of results for grinding and spotting experiments. Surface microroughness measurements were taken at five random locations within a spot ddp with the white-light interferometer. The amount of material removed by MRF (spot maximum depth) was extracted from the 3-D profilometer scans.

Material	ALON Processed with Contour Tool			
	Rough ground			
MRF Material Removal (μm)		0 (as ground)	10.93±0.23	23.83±0.12
Areal (μm)	p-v	14.52±1.04	1.2±0.4	1.1±0.2
	rms	1.45±0.02	0.09±0.01	0.07±0.02
Perpendicular (⊥) (μm)	p-v	8.12±0.49	0.40±0.04	0.30±0.06
	rms	1.41±0.05	0.09±0.00	0.07±0.02
Parallel (∥) (μm)	p-v	8.12±0.49	0.39±0.05	0.23±0.10
	rms	1.41±0.05	0.07±0.02	0.06±0.03
	Medium Ground			
MRF Material Removal (μm)		0 (as ground)	9.12±0.11	21.57±0.51
Areal (μm)	p-v	11.72±0.00	0.56±0.16	0.65±0.17
	rms	0.72±0.02	0.09±0.02	0.12±0.03
Perpendicular (⊥) (μm)	p-v	4.84±0.42	0.39±0.09	0.47±0.11
	rms	0.70±0.03	0.09±0.02	0.12±0.03
Parallel (∥) (μm)	p-v	4.84±0.42	0.23±0.06	0.18±0.03
	rms	0.70±0.03	0.05±0.01	0.04±0.01
	Fine Ground			
MRF Material Removal (μm)		0 (as ground)	5.98±0.31	21.50±0.10
Areal (μm)	p-v	4.24±1.44	0.51±0.09	1.05±0.06
	rms	0.10±0.05	0.08±0.01	0.16±0.04
Perpendicular (⊥) (μm)	p-v	0.67±0.50	0.33±0.03	0.72±0.16
	rms	0.07±0.03	0.07±0.00	0.16±0.04
Parallel (∥) (μm)	p-v	0.67±0.50	0.22±0.04	0.19±0.09
	rms	0.07±0.03	0.05±0.01	0.05±0.03

Table 110.VI(b): Selected summary of results for grinding and spotting experiments. Surface microroughness measurements were taken at five random locations within a spot ddp with the white-light interferometer. The amount of material removed by MRF (spot maximum depth) was extracted from the 3-D profilometer scans.

Material	CVD SiC Processed with Contour Tool			
	Rough Ground			
MRF Material Removal ( $\mu\text{m}$ )		0 (as ground)	1.70 $\pm$ 0.060	9.41 $\pm$ 0.012
Areal ( $\mu\text{m}$ )	p-v	3.680 $\pm$ 0.228	0.193 $\pm$ 0.042	0.126 $\pm$ 0.013
	rms	0.108 $\pm$ 0.006	0.021 $\pm$ 0.004	0.018 $\pm$ 0.004
Perpendicular ( $\perp$ ) ( $\mu\text{m}$ )	p-v	1.453 $\pm$ 0.200	0.107 $\pm$ 0.014	0.080 $\pm$ 0.016
	rms	0.10 $\pm$ 0.005	0.020 $\pm$ 0.004	0.017 $\pm$ 0.004
Parallel (  ) ( $\mu\text{m}$ )	p-v	1.453 $\pm$ 0.200	0.061 $\pm$ 0.008	0.056 $\pm$ 0.007
	rms	0.10 $\pm$ 0.005	0.013 $\pm$ 0.002	0.012 $\pm$ 0.001
Medium Ground				
MRF Material Removal ( $\mu\text{m}$ )		0 (as ground)	1.61 $\pm$ 0.020	8.64 $\pm$ 0.03
Areal ( $\mu\text{m}$ )	p-v	3.464 $\pm$ 0.177	0.169 $\pm$ 0.041	0.140 $\pm$ 0.025
	rms	0.077 $\pm$ 0.009	0.021 $\pm$ 0.007	0.020 $\pm$ 0.004
Perpendicular ( $\perp$ ) ( $\mu\text{m}$ )	p-v	1.184 $\pm$ 0.066	0.105 $\pm$ 0.031	0.080 $\pm$ 0.039
	rms	0.070 $\pm$ 0.004	0.020 $\pm$ 0.007	0.030 $\pm$ 0.021
Parallel (  ) ( $\mu\text{m}$ )	p-v	1.184 $\pm$ 0.066	0.054 $\pm$ 0.010	0.047 $\pm$ 0.007
	rms	0.070 $\pm$ 0.004	0.011 $\pm$ 0.002	0.010 $\pm$ 0.002
Fine Ground				
MRF Material Removal ( $\mu\text{m}$ )		0 (as ground)	1.86 $\pm$ 0.090	10.23 $\pm$ 0.120
Areal ( $\mu\text{m}$ )	p-v	0.424 $\pm$ 0.069	0.141 $\pm$ 0.054	0.136 $\pm$ 0.025
	rms	0.018 $\pm$ 0.002	0.013 $\pm$ 0.001	0.019 $\pm$ 0.003
Perpendicular ( $\perp$ ) ( $\mu\text{m}$ )	p-v	0.011 $\pm$ 0.005	0.073 $\pm$ 0.009	0.091 $\pm$ 0.012
	rms	0.018 $\pm$ 0.001	0.012 $\pm$ 0.001	0.019 $\pm$ 0.003
Parallel (  ) ( $\mu\text{m}$ )	p-v	0.011 $\pm$ 0.005	0.060 $\pm$ 0.006	0.043 $\pm$ 0.006
	rms	0.018 $\pm$ 0.001	0.012 $\pm$ 0.001	0.009 $\pm$ 0.002

Table 110.VI(c): Selected summary of results for grinding and spotting experiments. Surface microroughness measurements were taken at five random locations within a spot ddp with the white-light interferometer. The amount of material removed by MRF (spot maximum depth) was extracted from the 3-D profilometer scans.

Material	PCA Processed with Ring Tool			
	Medium Ground			
MRF Material Removal ( $\mu\text{m}$ )		0 (as ground)	8.84 $\pm$ 0.07	15.9 $\pm$ 0.06
Areal ( $\mu\text{m}$ )	p-v	8.942 $\pm$ 1.067	0.247 $\pm$ 0.031	0.276 $\pm$ 0.045
	rms	0.569 $\pm$ 0.076	0.033 $\pm$ 0.006	0.044 $\pm$ 0.008
Perpendicular ( $\perp$ ) ( $\mu\text{m}$ )	p-v	3.613 $\pm$ 0.401	0.177 $\pm$ 0.0028	0.220 $\pm$ 0.039
	rms	0.460 $\pm$ 0.082	0.033 $\pm$ 0.006	0.043 $\pm$ 0.008
Parallel (  ) ( $\mu\text{m}$ )	p-v	3.613 $\pm$ 0.401	0.128 $\pm$ 0.008	0.101 $\pm$ 0.008
	rms	0.460 $\pm$ 0.082	0.030 $\pm$ 0.002	0.022 $\pm$ 0.002

For orthogonal line scans, the initial ground p-v roughness is similar, as the ground surface shows no processing-related directional features {~8.1-, ~1.4-, ~3.6- $\mu\text{m}$  p-v, for ALON [see Fig. 110.40(a)], CVD SiC [see Fig. 110.40(b)], and PCA [see Fig. 110.40(c)], respectively}. In the case of ALON [Fig. 110.40(a)], for both line-scan orientations ( $\perp$  and  $\parallel$ ) with respect to the direction of MRF fluid flow over the surface, p-v surface roughness is seen to drop from ~400 nm to ~300 ( $\perp$ ) and ~230 nm ( $\parallel$ ), respectively, in the second stage as the diamonds in the MR fluid continue to polish the surface, removing a total of ~24  $\mu\text{m}$  of material. In the case of CVD SiC [Fig. 110.40(b)], p-v surface roughness ( $\perp$ ) is seen to drop from 107 to 80 nm, whereas p-v surface roughness ( $\parallel$ ) drops slightly from 61 to 56 nm, as the diamonds in the MR fluid continue to polish the surface, removing a total of ~9.4  $\mu\text{m}$  of material. In the case of PCA, p-v surface roughness ( $\parallel$ ) is seen to drop from ~0.13 to 0.1  $\mu\text{m}$ , as the diamonds in the MR fluid continue to polish the surface, removing a total of 16  $\mu\text{m}$  of material. Although not described here, it is possible to study the microstructure of the material with this sampling technique,

one example being decoration of grain boundaries.<sup>38</sup> However, as in the case of PCA [Fig. 110.40(c)], p-v roughness (areal and  $\perp$ ) is seen to increase with additional material removed beyond ~9  $\mu\text{m}$  in the second stage. This increase is real, and is due to a texture or grooving impressed on the polished, damage-free surface by the abrasives in the MR fluid. These grooves come from a lack of part rotation during long-duration spotting.

An interesting observation can be made for both ALON and CVD SiC: In the second stage, where the interaction between the MR fluid abrasives and the surface is strong, there is a gradual increase in p-v roughness as shown with all three measurement protocols ending with an abrupt drop in the p-v roughness; after this, the roughness either increases or slightly decreases. For both ALON and CVD SiC, this phenomenon takes place when the amount of material removed by the MRF reaches a depth comparable to the material grain size {~12 and 4  $\mu\text{m}$  for ALON [see Fig. 110.40(a)] and CVD SiC [see Fig. 110.40(b)], respectively}. This phenomenon is not present in the case of PCA [Fig. 110.40(c)], suggesting that, as grain

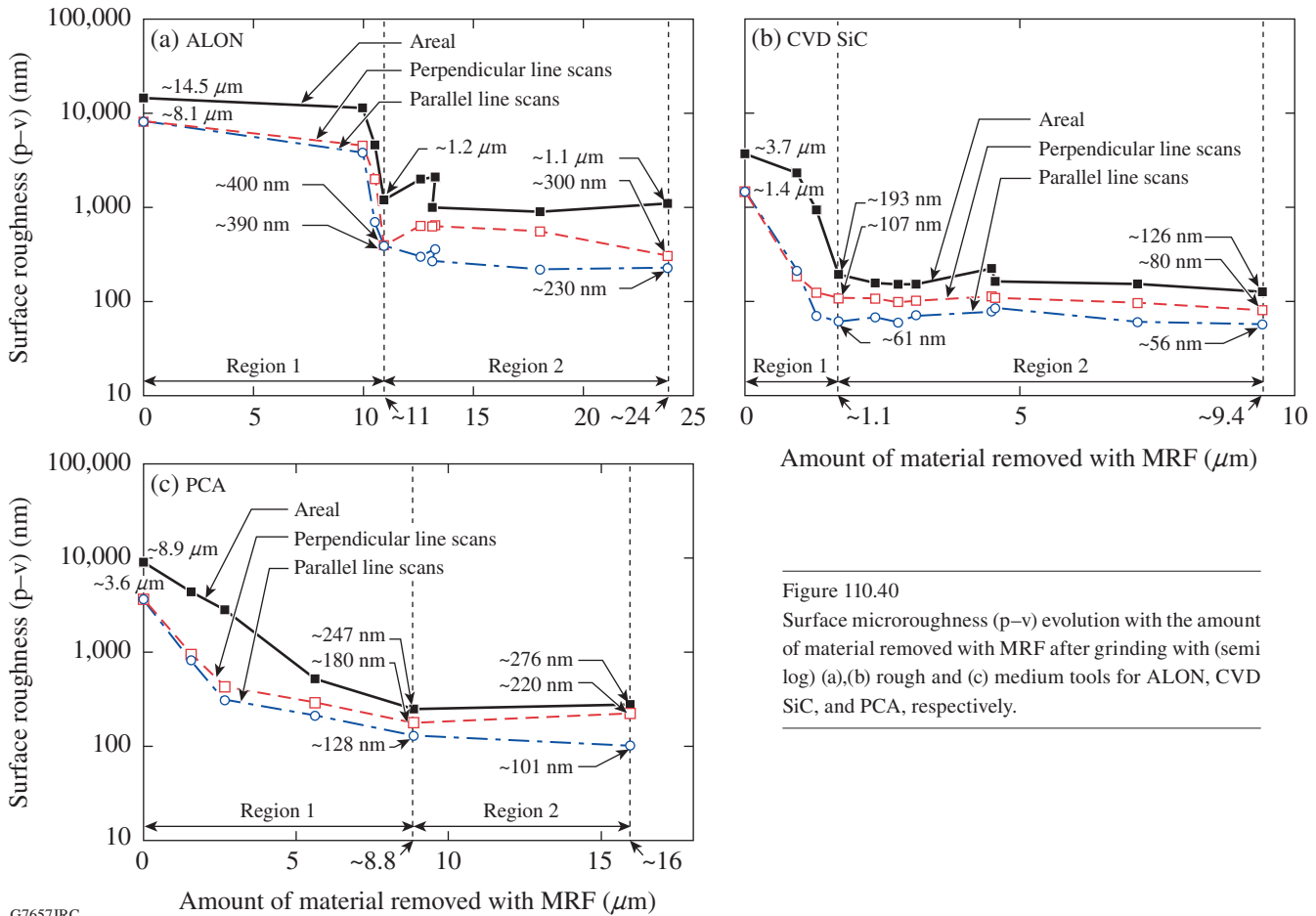


Figure 110.40  
Surface microroughness (p-v) evolution with the amount of material removed with MRF after grinding with (semi log) (a),(b) rough and (c) medium tools for ALON, CVD SiC, and PCA, respectively.

G7657JRC

size increases, the interaction between a material's grains and the polishing abrasives contributes to surface roughening, or "grain decoration."

SEM analysis within polishing spots confirms that MRF exposes and removes fractured material in both stages 1 and 2, without creating additional damage. Figure 110.41 shows the evolution of surface texture in spots taken on previously medium-ground PCA. Figures 110.41(a) and 110.41(b) represent spot depths of ~2 to 3 μm, where MRF processing exposed voids and pulverized powder regime beneath the deformed layer. Longer spotting times to remove up to a total of 16 μm of material [see Figs. 110.41(c)–110.41(e)] verify that MRF eliminated all pitting and hidden damage, with the subsequent development of a grooved texture.

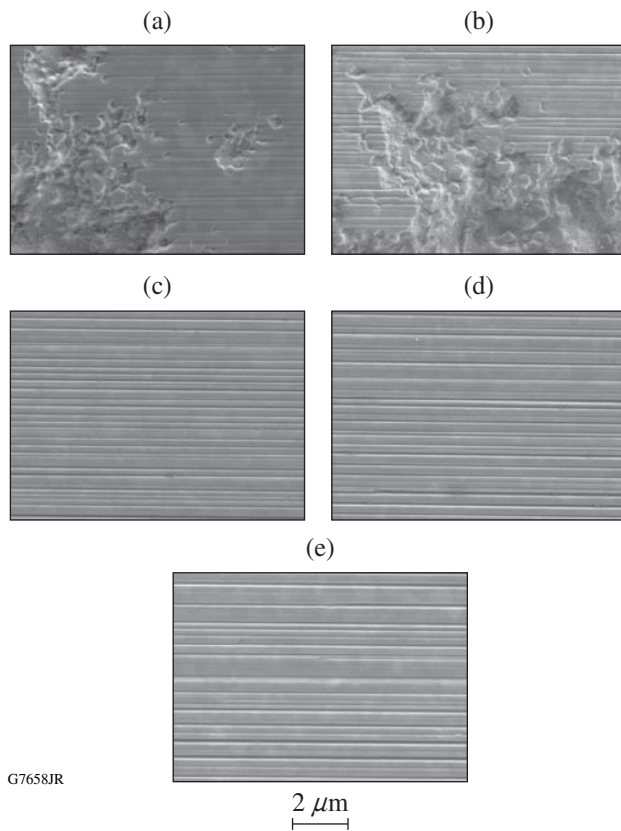


Figure 110.41 SEM images inside MRF spots taken on PCA that was previously medium ground (10- to 20-μm grit size) to an initial roughness of 3.6-μm p-v. (a)–(e) ~1.6-, 2.6-, 5.6-, 9-, and 16-μm spot depths (MRF material removed), respectively. The initial deformation layer as seen in Figs. 110.36(e) and 110.36(f) is completely removed. Long spot dwell times [(d), (e)] enhanced the intrinsic directionality of the MRF process.

### 1. Use of Power Spectrum to Quantify Surface Topography

In addition to the conventional p–v and rms values that define surface roughness, the interaction between the MR fluid and the material surface is discussed in terms of the power spectral density (PSD). This analysis results in a unique signature,<sup>39</sup> in which surface texture parallel (||) and perpendicular (⊥) to the MR fluid flow direction may be observed and studied to obtain information on the surface and its microstructure.

For a given surface profile  $z(x)$ , the rms roughness is defined as

$$\text{rms} = \sqrt{\frac{1}{N} \cdot \sum_{i=1}^N z_i^2} \quad (m) \quad (1)$$

and the 1-D PSD at spatial frequency  $f_j = j\Delta f$  is<sup>40</sup>

$$\text{PSD}_{1-D}(f_j) \approx \frac{\Delta x}{N} \left| \sum_{k=1}^N z_k \exp[(2\pi i)jk/N] \right|^2, \quad (2)$$

$$j = 1, 2, \dots, N/2,$$

where  $\Delta f = 1/(N\Delta x) = 1/L$ , with  $L$  being the scan length. PSD is a statistical function that allows a breakdown of the surface roughness over a range of spatial frequencies. Furthermore, the area under a 1-D PSD curve (between two spatial-frequency limits) is a measure of the rms surface roughness in this spatial range:<sup>41</sup>

$$\text{rms}_{1-D}^2 = \int_{f_{\min}}^{f_{\max}} \text{PSD}_{1-D}(f) df. \quad (3)$$

After removing the low-frequency terms (tilt, curvature, etc.) from the roughness data for part surfaces discussed in **Experimental Results** (p. 102), horizontal 1-D PSD plots were generated from areal measurements ( $0.35 \times 0.26 \text{ mm}^2$ ) taken with a white-light interferometer over spatial frequencies extending from  $2.0 \times 10^{-6} \text{ nm}^{-1}$  to  $2.0 \times 10^{-2} \text{ nm}^{-1}$  by using multiple line scans in a direction perpendicular (⊥) to the MRF flow, as seen in Fig. 110.39(a). Removing the low-frequency terms resulted in an improved PSD spectrum.<sup>42</sup>

Because the white-light interferometer has a lateral resolution limit of 1 μm, additional 1-D PSD plots were generated from AFM scans with a lateral resolution in the nanometer range. These scans were also done within spot ddp regions.

A consideration of PSD data generated from profiles perpendicular ( $\perp$ ) to the MRF flow direction allows us to study the residual grooving pattern of the MR fluid flow that represents the abrasive/surface interactions.

2. MRF Signature on Hard Materials

Figure 110.42 shows the PSD curves in ddp regions for two spots of increasing time duration taken on the surface of initially rough-ground ALON. The curves represent the evolution of surface texture with the amount of material removed by the MRF spot, from  $\sim 10.5 \mu\text{m}$  to  $\sim 24 \mu\text{m}$  (corresponding to 3- and 16-min spot dwell times, respectively). The interferometer PSD curves (i.e., at lower spatial frequencies) show an amplitude reduction from the short- to the long-dwell-time spots, due to surface smoothing of roughness contributions of the MRF process. The material's microstructure dominates the curve in

the spatial frequency range of  $7 \times 10^{-5}$  to  $3 \times 10^{-4} \text{ nm}^{-1}$ , corresponding to features of the order of  $\sim 50$  to  $100 \mu\text{m}$  (comparable to the ALON grain size).

AFM measurements were taken and evaluated to examine the PSD across the surface of a single grain in the spatial frequency range of  $1 \times 10^{-4}$  to  $1 \times 10^{-2} \text{ nm}^{-1}$  (corresponding to features of the order of 10 to  $0.1 \mu\text{m}$ ; see scale at top of Fig. 110.42). When compared to the interferometer results, the AFM measurements show a reversal. PSD values for the 16-min-duration spot have higher amplitudes across all relevant spatial frequencies due to the grooving effect of the MRF process on the surface of a single grain. The morphology of the grooving pattern represents the "MRF signature on hard materials." Figures 110.43(a) and 110.43(b) show the surface morphologies within these spots detected by the AFM. Profiles

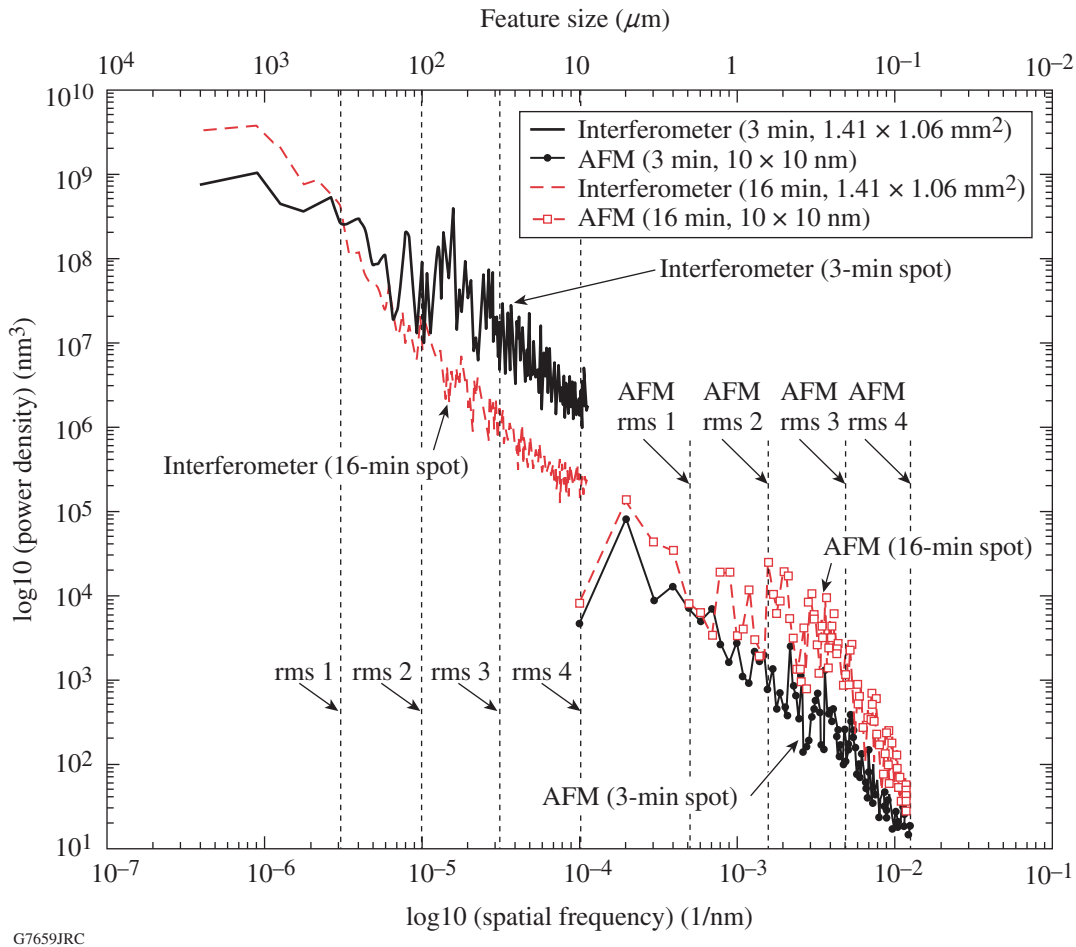


Figure 110.42 PSD (log-log) for MRF spotting done on initially rough-ground (40- $\mu\text{m}$  grit size) ALON. White-light interferometer measurements were taken using a 2.5 objective using a  $2\times$  magnification ( $1.41 \times 1.06 \text{ mm}^2$ ).

of these scans taken across the image diagonal represented by a white line are shown in Fig. 110.43(c) and 110.43(d). The images and accompanying profiles agree well with the PSD function. For example, when we calculate the number of features ( $\sim 40$ ) across the diagonal ( $\sim 15 \mu\text{m}$ ) of Fig. 110.43(b), formed by the long-dwell-time MRF spot, the number corresponds to a feature size of the order of  $0.5 \mu\text{m}$  at  $2 \times 10^{-3} \text{ nm}^{-1}$  spatial frequency, which corresponds to the peak in that frequency, as seen in Fig. 110.42. The markers in Fig. 110.43(c) extend over vertical heights in the range of  $\sim 11$  to  $14 \text{ nm}$ , for the short-dwell-time spot, whereas the markers in Fig. 110.43(d) for the long-dwell-time spot extend over vertical heights in the range of  $\sim 19$  to  $30 \text{ nm}$ .

The calculated rms values from the PSD curves of Fig. 110.42, designated as rms 1, rms 2, etc., on the figure, are plotted in Fig. 110.44. The left-hand side of Fig. 110.44 shows the calculated rms values for ALON, corresponding to the spatial frequency of the interferometer PSD curves in Fig. 110.42, and the calculated rms values from the PSD curves for CVD SiC and PCA where we used a  $20\times$  objective and a  $\sim 350\text{-}\mu\text{m}$  spatial scan length (511 data points) in the spatial-frequency range of  $0.2 \times 10^{-5}$  to  $0.9 \times 10^{-3} \text{ nm}^{-1}$  (corresponding to features of the order of  $\sim 100$  to  $1 \mu\text{m}$ ) on the interferometer. As seen in Fig. 110.42, we notice a decrease in rms surface roughness from the short- to the long-dwell-time spots for ALON (see arrow 1). [The roughness increase for the 16-min spot at

low frequencies is due to surface figure errors from grinding.] In the case of CVD SiC there is an increase in the PSD from the short to the long MRF spot dwell time (see arrow 2). This increase represents an increase in surface roughness on the part surface due to decoration of grain boundaries within the spatial-frequency range of  $10^{-4}$  to  $10^{-3} \text{ nm}^{-1}$ , representing features of the order of  $1$  to  $10 \mu\text{m}$ , comparable to the material grain size. [The increase in the curve amplitude for CVD SiC (16-min spot) in the low-frequency range is also attributed to surface figure error as mentioned above for ALON.] In the case of PCA, we see a large reduction in roughness values for the long- compared to the short-dwell-time spots (see arrow 3). This can be attributed to surface smoothing of roughness contributions in this interval, in the spatial-frequency range of  $3.2 \times 10^{-5}$  to  $10^{-4} \text{ nm}^{-1}$ . There is almost no change in the spatial-frequency range of  $3.2 \times 10^{-4}$  to  $10^{-3} \text{ nm}^{-1}$ , corresponding to a feature size of the order of  $3.3$  to  $1 \mu\text{m}$ . This represents features that are much larger than the nominal grain size, possibly due to grain clusters.

The right-hand side of Fig. 110.44 shows the calculated rms values for PSD curves done in the spatial-frequency range of  $0.0002$  to  $0.02 \text{ nm}^{-1}$  (corresponding to features of the order of  $1$  to  $0.05 \mu\text{m}$ ) using the AFM. These results are within the boundaries of a single grain for ALON, whereas for both CVD SiC ( $5\text{-}10\text{-}\mu\text{m}$  grain size) and PCA (submicron-range grain size), these results span at least one grain boundary. Notice

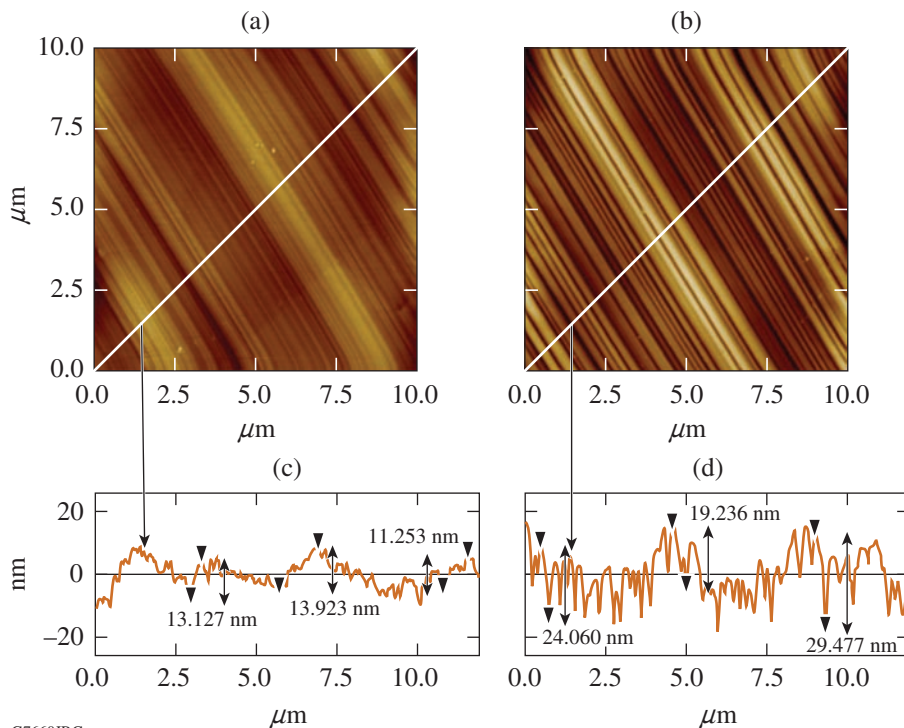


Figure 110.43  
AFM scans taken at spots' ddp of initially rough-ground ALON: (a) short- and (b) long-dwell-time spots (3 and 16 min, respectively); (c),(d) profiles taken across the diagonal of scans, represented by the white lines in (a) and (b), respectively. The markers in (c) and (d) represent vertical heights in a range of  $\sim 11$  to  $14 \text{ nm}$  and  $\sim 19$  to  $30 \text{ nm}$  for the short- and long-dwell-time spot, respectively. The grain size is  $50$  to  $100 \mu\text{m}$ .

G7660JRC

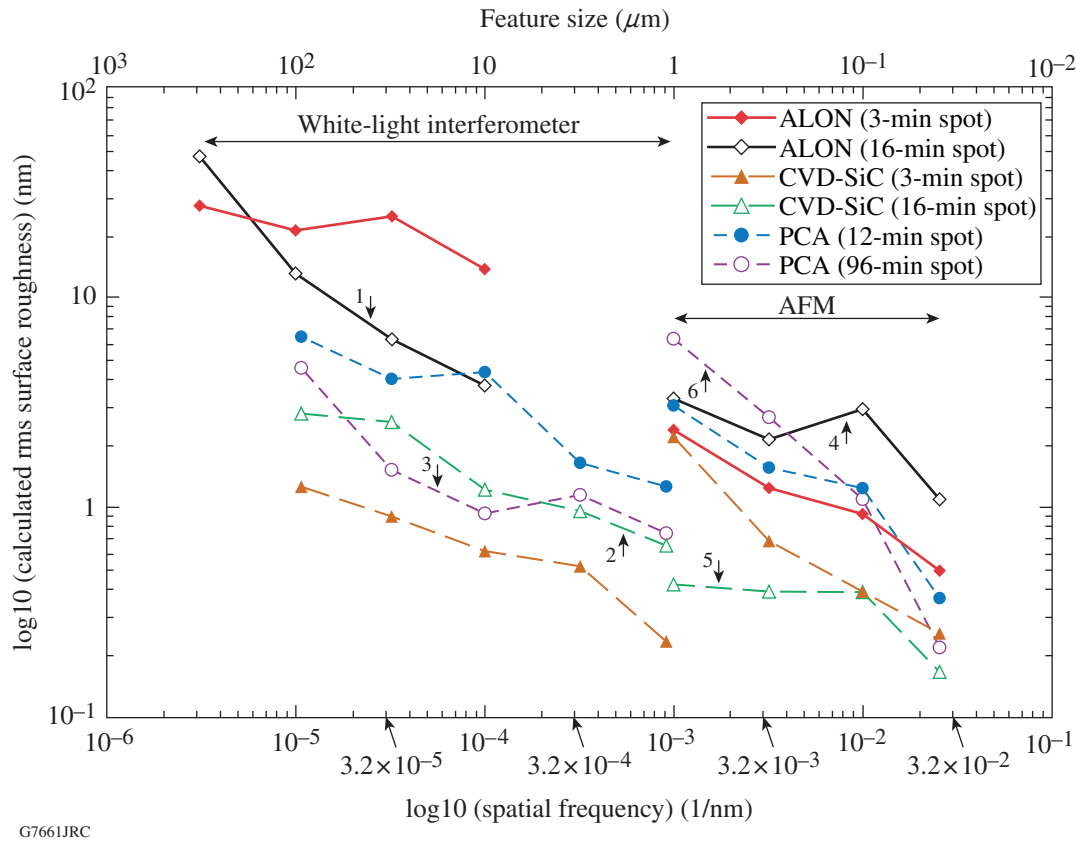


Figure 110.44

Calculated rms (nm) surface roughness from PSD plots generated from the interferometer and AFM measurements (log-log). Data points represent the averaged rms values for a specific spatial-frequency bandwidth, indicated as rms 1, rms 2, etc., in Fig. 110.42.

the increase in the roughness values for ALON at the spatial frequency  $10^{-2} \text{ nm}^{-1}$  (see arrow 4), indicating the presence of MRF signature, as discussed for Figs. 110.42 and 110.43. There is almost no change in surface roughness at the spatial frequency  $10^{-2} \text{ nm}^{-1}$  for both CVD SiC and PCA, corresponding to the MRF signature. Beyond this frequency we notice a reduction in roughness for all three materials: In the case of CVD SiC, there is a decrease in surface roughness from the short- to the long-dwell-time spot (see arrow 5). In the case of PCA, an increase in surface roughness from the short- to the long-dwell-time spot (see arrow 6) in a spatial-frequency range of  $10^{-3}$  to  $3.2 \times 10^{-3} \text{ nm}^{-1}$ , corresponding to features of the order of 1000 to 300 nm (comparable to the PCA grain size), is due to grain boundary highlighting by the MRF process, i.e., grain decoration.<sup>43</sup>

## Conclusions

The response of three hard optical ceramics to deterministic microgrinding has been studied. Grinding experiments showed that grinding-induced surface roughness decreased with a

decreasing size in the diamond abrasive used. Microgrinding with a rough tool involved fracture, leading to p-v surface roughness in the range of 14.5 to 4  $\mu\text{m}$  (1.4- to 0.1- $\mu\text{m}$  rms). Using high-magnification SEM images, we found that the deformed layer induced by grinding covered the actual damage depth/SSD.

We have demonstrated that an MRF spot can be placed on ground surfaces of hard ceramics without introducing additional damage, and that the spot can be used to estimate the induced SSD depth from microgrinding. For initially rough and medium surfaces, SSD depth is  $\sim 11 \mu\text{m}$  (ALON),  $\sim 1.7 \mu\text{m}$  (CVD SiC), and  $\sim 9 \mu\text{m}$  (PCA), corresponding to initial p-v surface roughness values of  $\sim 14.5 \mu\text{m}$ ,  $\sim 3.7 \mu\text{m}$ , and  $\sim 9 \mu\text{m}$ , respectively. The evolution of surface roughness with the amount of material removed by the MRF process, as measured within the spot's deepest point of penetration (least roughness), can be divided into two stages: In the first stage the induced damaged layer and associated SSD from microgrinding are removed, reaching a low surface-roughness value. In the

second stage we observe interaction between the MRF process and the material's microstructure as MRF exposed the subsurface without introducing new damage. We showed that SSD depth can be estimated by using an optical profilometer-based measurement of the areal p-v surface microroughness of the as-ground surface. This provides an upper bound to the SSD value. SEM images confirmed these observations.

We also showed the development of the "MRF signature" on hard ceramics by computing PSD curves within the resolution capabilities of the interferometer and the AFM. By considering PSD data generated from profiles perpendicular to the MRF flow direction, we studied the residual grooving pattern of the MR fluid flow that represents the abrasive/surface interactions. Additional work is still needed, however, to characterize MR fluid particles/surface (i.e., materials' microstructure) interactions parallel to the MR fluid flow direction.

The spotting technique is intended only as a diagnostic tool, by removing material from rough surfaces to expose the subsurface damage. It does not reflect on the true polishing capabilities with MRF technology for hard ceramics.

#### ACKNOWLEDGMENT

The authors thank A. Shorey (QED Technologies, Rochester, NY) for the use of the AFM and H. Romanosky (LLE) for MRF spot-taking. The authors acknowledge the Laboratory for Laser Energetics at the University of Rochester for its continuing support. One of the authors (S. N. Shafirir) is an LLE Horton Fellow. Research was sponsored by the U.S. Army Armament, Research, Development and Engineering Center (ARDED) and was accomplished under Cooperative Agreement No. W15QKN-06-R-0501 and the U.S. Department of Energy Office of Inertial Confinement Fusion under Cooperative Agreement No. DE-FC52-92SF19460, the University of Rochester, and the New York State Energy Research and Development Authority. The views and conclusions contained in this document are those of the authors and should not be interpreted as representing the official policies, either expressed or implied, of U.S. Army ARDEC or the U.S. Government. The support of DOE does not constitute an endorsement by DOE of the views expressed in this article. The U.S. Government is authorized to reproduce and distribute reprints for government purposes notwithstanding any copyright notation herein.

#### REFERENCES

1. L. Yin *et al.*, *Wear* **256**, 197 (2004).
2. S. Malkin and T. W. Hwang, *CIRP Ann.* **45**, 569 (1996).
3. B. Lin *et al.*, *Key Eng. Mater.* **202/203**, 121 (2001).
4. A. G. Evans and D. B. Marshall, in *Fundamentals of Friction and Wear of Materials*, edited by D. A. Rigney (American Society for Metals, Metals Park, OH, 1981), pp. 439–452.

5. J. A. Menapace *et al.*, in *Laser-Induced Damage in Optical Materials: 2005*, edited by G. J. Exarhos *et al.* (SPIE, Bellingham, WA, 2006), Vol. 5991, p. 599102.
6. J. C. Lambropoulos, S. D. Jacobs, and J. Ruckman, in *Finishing of Advanced Ceramics and Glasses*, edited by R. Sabia, V. A. Greenhut, and C. G. Pantano, *Ceramic Transactions*, Vol. 102 (The American Ceramic Society, Westerville, OH, 1999), pp. 113–128.
7. K. R. Fine *et al.*, in *Modeling, Simulation, and Verification of Space-Based Systems II*, edited by P. Motaghedi (SPIE, Bellingham, WA, 2005), Vol. 5799, pp. 105–110.
8. J. Wang and R. L. Maier, *Appl. Opt.* **45**, 5621 (2006).
9. P. E. Miller *et al.*, in *Laser-Induced Damage Optical Materials: 2005*, edited by G. J. Exarhos *et al.* (SPIE, Bellingham, WA, 2006), Vol. 5991, p. 599101.
10. W. Kanematsu, *J. Am. Ceram. Soc.* **89**, 2564 (2006).
11. B. Zhang and T. Howes, *CIRP Ann.* **43**, 305 (1994).
12. B. Zhang and T. D. Howes, *CIRP Ann.* **44**, 263 (1995).
13. J. A. Randi, J. C. Lambropoulos, and S. D. Jacobs, *Appl. Opt.* **44**, 2241 (2005).
14. H. H. K. Xu, S. Jahanmir, and Y. Wang, *J. Am. Ceram. Soc.* **78**, 881 (1995).
15. J. A. Menapace *et al.*, in *Laser-Induced Damage in Optical Materials: 2005*, edited by G. J. Exarhos *et al.* (SPIE, Bellingham, WA, 2006), Vol. 5991, p. 599103.
16. F. W. Preston, *Trans. Opt. Soc.* **XXIII**, 141 (1921–22).
17. F. K. Aleinikov, *Sov. Phys.-Tech. Phys.* **2**, 505 (1957).
18. P. P. Hed and D. F. Edwards, *Appl. Opt.* **26**, 4677 (1987).
19. J. C. Lambropoulos, Y. Li, P. D. Funkenbusch, and J. L. Ruckman, in *Optical Manufacturing and Testing III*, edited by H. P. Stahl (SPIE, Bellingham, WA, 1999), Vol. 3782, pp. 41–50.
20. S. N. Shafirir, J. Lambropoulos, and S. D. Jacobs, *Precision Engineering* **31**, 83 (2007).
21. S. N. Shafirir, J. C. Lambropoulos, and S. D. Jacobs, "Technical Note: Toward Magnetorheological Finishing of Magnetic Materials," to be published in the *Journal of Manufacturing Science and Engineering*.
22. J. C. Lambropoulos, in *Optical Fabrication and Testing*, Vol. 42, 2000 OSA Technical Digest Series (Optical Society of America, Washington, DC, 2000), pp. 17–18.
23. A. G. Evans, in *Fracture Mechanics Applied to Brittle Materials*, edited by S. W. Freiman (American Society for Testing and Materials, Philadelphia, 1979), Vol. ASTM STP 678, Part 2, pp. 112–135.
24. D. Halliday, R. Resnick, and J. Walker, *Fundamentals of Physics*, 5th ed. (Wiley, New York, 1997).
25. SX 50 CNC deterministic microgrinding machine, OptiPro Systems, Ontario, NY 14519.

26. SX 150 CNC deterministic microgrinding machine, OptiPro Systems, Ontario, NY 14519.
27. Opticut GPM 5% in water, pH 9-10, Lighthouse Lubricant Solutions, LLC, Overland Park, KS 66282.
28. S. D. Jacobs, H. M. Pollicove, W. I. Kordonski, and D. Golini, in *International Conference on Precision Engineering, ICPE '97 (ICPE, Taipei, Taiwan, 1997)*, pp. 685–690.
29. A. B. Shorey, S. D. Jacobs, W. I. Kordonski, and R. F. Gans, *Appl. Opt.* **40**, 20 (2001).
30. Q22-Y, QED Technologies, LLC, Rochester, NY 14607.
31. D10 MR fluid, QED Technologies, LLC, Rochester, NY 14607.
32. TalySurf 2 PGI profilometer, Taylor Hobson, Inc., Rolling Meadows, IL 60008-4231.
33. NewView™ 5000 noncontact profilometer, Zygo Corporation, Middlefield, CT 06455.
34. LEO 982 FE SEM, Nano Technology Systems Division, Carl Zeiss NTS GmbH, A Carl Zeiss SMT AG Company, 73447 Oberkochen, Germany.
35. Dimension 3100S-1 AFM, Digital Instruments/Veeco Metrology Dimension 3100S-1 Atomic Force Microscope, Veeco Instruments, Inc., Woodbury, NY 11797-2902.
36. Light Microscope, Leica Microsystems Inc., Bannockburn, IL 60015.
37. S. N. Shafir, "Surface Finish and Subsurface Damage in Polycrystalline Optical Materials," Ph.D. thesis, University of Rochester, 2007.
38. S. R. Arrasmith, I. A. Kozhina, L. L. Gregg, A. B. Shorey, H. J. Romanofsky, S. D. Jacobs, D. Golini, W. I. Kordonski, S. J. Hogan, and P. Dumas, in *Optical Manufacturing and Testing III*, edited by H. P. Stahl (SPIE, Bellingham, WA, 1999), Vol. 3782, pp. 92–100.
39. J. E. DeGroote, A. E. Marino, K. E. Spencer, and S. D. Jacobs, in *Optifab 2005* (SPIE, Bellingham, WA, 2005), Vol. TD03, pp. 134–138.
40. E. Marx *et al.*, *J. Vac. Sci. Technol. B* **20**, 31 (2002).
41. A. Duparré *et al.*, *Appl. Opt.* **41**, 154 (2002).
42. C. J. Walsh, A. J. Leistner, and B. F. Oreb, *Appl. Opt.* **38**, 4790 (1999).
43. L. L. Gregg, A. E. Marino, J. C. Hayes, and S. D. Jacobs, in *Optical Manufacturing and Testing V*, edited by H. P. Stahl (SPIE, Bellingham, WA, 2004), Vol. 5180, pp. 47–54.

---

# Spectral Filtering in a Diode-Pumped Nd:YLF Regenerative Amplifier Using a Volume Bragg Grating

## Introduction

Holographic volume Bragg gratings (VBG's) represent a new class of robust, highly efficient, and spectrally selective optical elements that are recorded in photo-thermo-refractive glass.<sup>1</sup> VBG's have extremely high spectral and angular dispersions that are higher than any dispersive elements previously used. VBG's are stable at elevated temperatures, have a high optical-damage threshold similar to that of bulk glass materials, and have high diffraction efficiency and low losses, allowing their use in laser resonators.

VBG's are widely used in laser devices for spectrum and beam profile control. Employing VBG's in an external resonator of laser diodes makes it possible to produce high-brightness, near-diffraction-limited beams and coherently combine them.<sup>2</sup> A high-brightness spectral-beam combination of two vertical-external-cavity, surface-emitting lasers has been demonstrated with the aid of a VBG.<sup>3</sup> VBG's have also been used as spectrally selective elements for laser wavelength tuning<sup>4</sup> as well as line narrowing in lasers<sup>5,6</sup> and optical parametric oscillators.<sup>7</sup> Chirped VBG's have been employed for ultrashort-pulse stretching and compression.<sup>8</sup>

Generating high-energy optical pulses in laser amplifiers requires high gain that inherently produces amplified spontaneous emission (ASE) with bandwidths of the order of the amplification bandwidth of the laser system, which can be detrimental to the temporal quality, energy extraction, and stability of laser amplifiers.<sup>9</sup> Amplification of optical pulses usually requires low ASE levels. For example, the temporal contrast of high-energy, short optical pulses amplified by the optical parametric chirped-pulse-amplification (OPCPA) system can be degraded by ASE-induced noise on the pump pulse.<sup>10</sup>

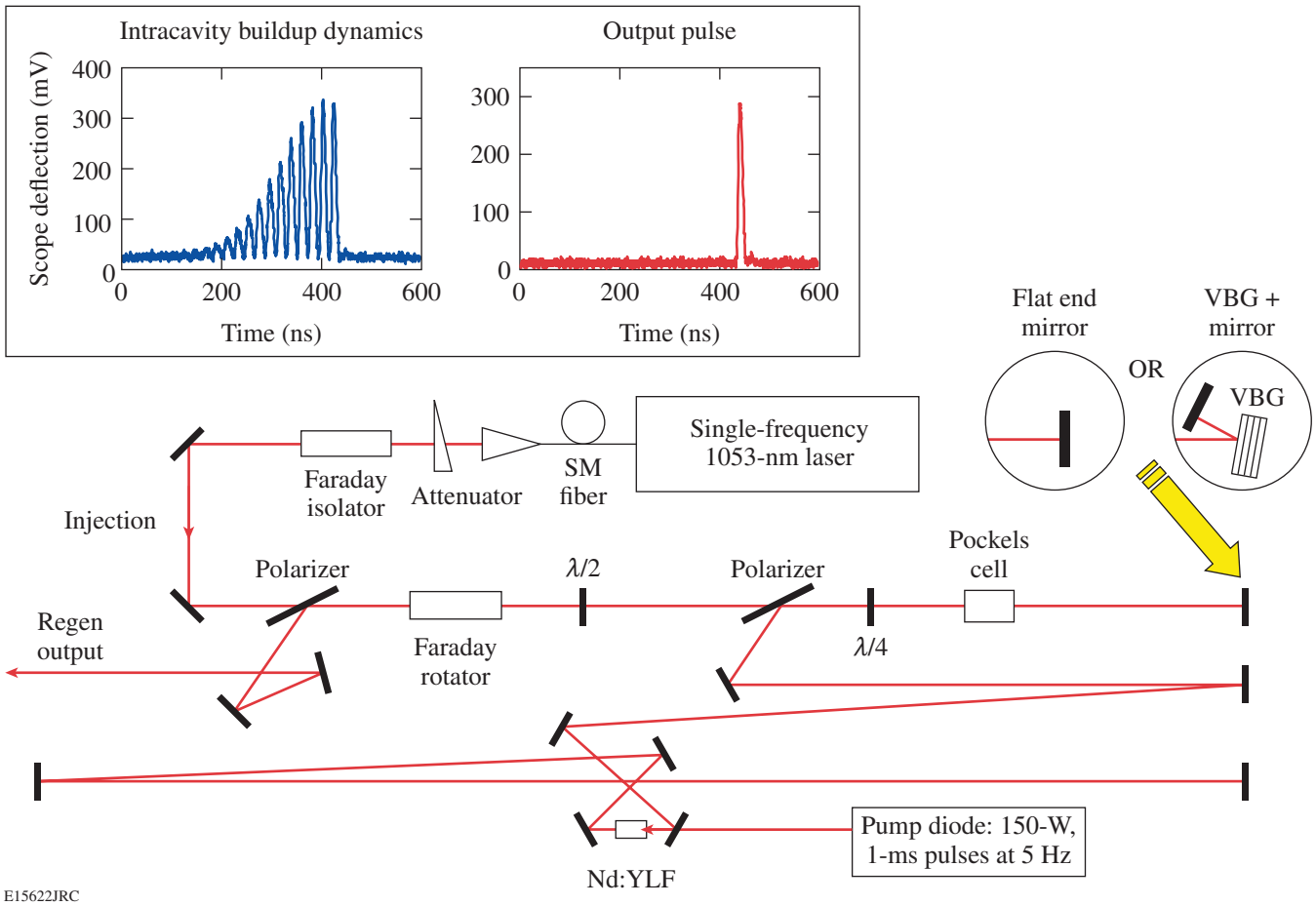
In this article we demonstrate for the first time that employing a VBG as a spectrally selective reflective element in a regenerative amplifier resonator significantly improves the spectral quality of the regenerative amplifier output by suppressing out-of-band amplified spontaneous emission. This spectrally filtered regenerative amplifier should be very

beneficial for applications where high spectral quality of pulsed radiation is required, such as pump lasers for high-contrast OPCPA systems.<sup>11</sup>

## Experimental Setup

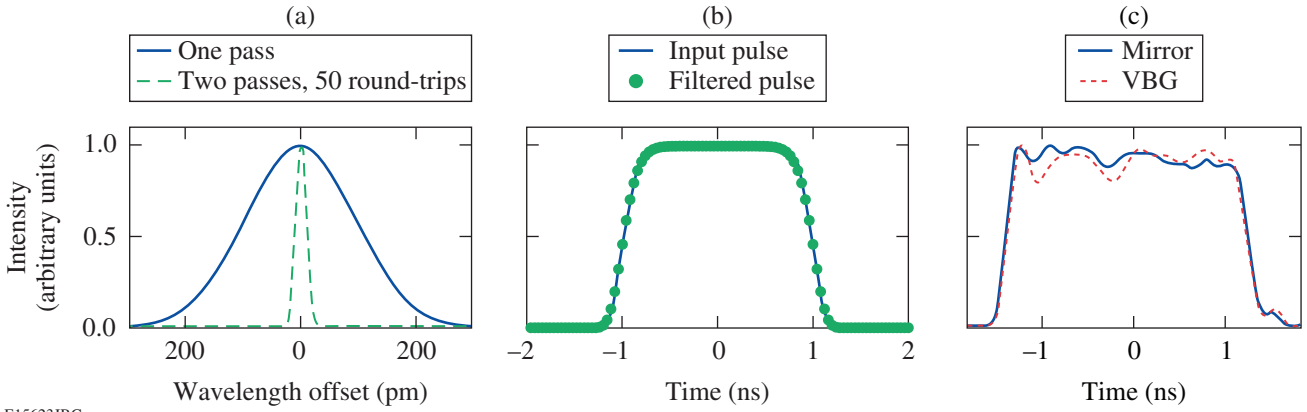
The Nd:YLF diode-pumped regenerative amplifier (DPRA) shown in Fig. 110.45 is identical to the one described in Ref. 12, the only difference being that it has a longer cavity length. It has a folded linear cavity with a round-trip time of 21 ns that allows amplification of pulses as long as 13-ns FWHM in duration. The Nd:YLF active element is oriented for a 1053-nm operational wavelength and is pumped by a 150-W, fiber-coupled laser diode (Apollo Instruments, Irvine, CA), which is operated in a pulsed mode producing a 1-ms pump pulse at 805 nm with a 5-Hz repetition rate. The DPRA intracavity Pockels cell driven by fast electrical circuitry allows the injection and cavity dumping of the amplified pulse. The injected pulse is mode matched to the DPRA resonator and, after a certain number of round-trips, reaches its maximum energy and is dumped from the DPRA cavity (inset in Fig. 110.45). Two DPRA resonator configurations have been compared: (1) with a flat end mirror having 99.9% reflectivity and (2) with a combination of AR-coated VBG (OptiGrate, Orlando, FL) having 99.4% diffraction efficiency and the same flat end mirror. The VBG has a bandwidth of 230 pm (FWHM) centered at ~1053 nm with an ~7° angle of incidence.

Spectral filtering in a regenerative amplifier cavity benefits from the large number of passes on the filtering element. Assuming a single-pass filtering spectral transmission  $T(\omega)$ , the spectral filter after  $N$  round-trips in the cavity is  $T(\omega)^N$ , or  $T(\omega)^{2N}$  if the filter is seen twice per round-trip, which is the case in this implementation. Figure 110.46(a) displays the spectral reflection of a Gaussian filter with a 230-pm (FWHM) bandwidth centered at 1053 nm and the spectral reflection after 50 round-trips in a cavity with two passes on the filter per round-trip. The effective filtering function has a bandwidth of 23 pm (FWHM). Filtering of the ASE can be performed as long as the bandwidth reduction in the amplifier does not degrade the temporal pulse shape of the output pulse. Figure 110.46(b)



E15622JRC

Figure 110.45  
 A volume Bragg grating (VBG) is used in a folded-linear-cavity regenerative amplifier as one of the mirrors for spectral filtering. DPRA cavity dumping occurs when intracavity buildup reaches its maximum (inset).



E15623JRC

Figure 110.46  
 (a) VBG with a Gaussian filter function using a 230-pm FWHM, one-pass bandwidth (solid line) produces a filter function with an effective bandwidth of 23-pm FWHM after 50 round-trips in the DPRA with a VBG two-pass configuration (dashed line); (b) 2-ns-FWHM, super-Gaussian pulse before (solid line) and after (white circles) bandwidth narrowing using a 23-pm-FWHM filter (simulation); (c) measured 2.4-ns-FWHM pulse shape after the DPRA with further amplification and doubling for the DPRA with mirror (solid line) and VBG (dotted line).

shows a 2-ns (FWHM), 20th-order super-Gaussian pulse before and after filtering by a 23-pm (at  $-3$ -dB level) filtering function. The choice of the 2-ns-FWHM pulse duration corresponds to the typical pulse widths used to pump OPCPA systems.<sup>11</sup> In this simulation, no significant change in the temporal intensity is observed, showing that an even narrower filter could be used. While different round-trips in the cavity correspond to a different effective bandwidth of the filter, ASE is expected mostly from the source seeding the regenerative amplifier and the first few round-trips in the amplifier (when the pulse energy is low), which correspond to the narrowest effective filtering function. Figure 110.46(c) displays the pulse shape measured after amplification in the DPRA and a four-pass ring power amplifier and after second-harmonic generation, for use as the pump pulse in an OPCPA system. No significant change in the output square pulse, including the fast rising and falling edges, is observed when the mirror in the DPRA is replaced with the VBG + mirror combination.

In our experiment the DPRA is injected with a 13-ns-FWHM, Gaussian-like pulse that is sliced out of a 150-ns-FWHM pulse produced by a diode-pumped, single-frequency,  $Q$ -switched Nd:YLF laser.<sup>13</sup> The bandwidth of this pulse is obviously narrower than that of the 2-ns-FWHM, super-Gaussian pulse; therefore, no output-pulse distortion due to VBG spectral filtering is expected. The DPRA output energy, beam profile, and spectra have been recorded for both DPRA resonator configurations (with a mirror and a VBG + mirror combination).

### Experimental Results and Discussion

The beam profiles shown in Fig. 110.47 correspond to the  $TEM_{00}$  mode for both DPRA configurations (mirror and VBG). These beam profiles have been taken at a DPRA operational output-pulse energy of 4 mJ.

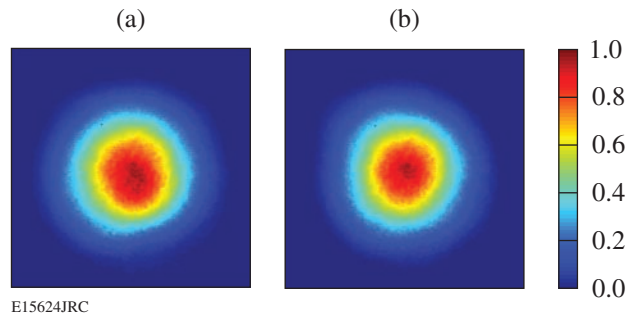


Figure 110.47 Output beam profile corresponds to  $TEM_{00}$  mode for both DPRA configurations with (a) a mirror and (b) VBG. DPRA output energy is 4 mJ.

The maximum energy produced by the DPRA with a mirror is 18 mJ. After introducing the VBG into the DPRA cavity, the maximum output energy drops to 14 mJ, which is consistent with introducing  $\sim 1.2\%$  of additional losses per round-trip by VBG with 99.4% diffraction efficiency. The output-beam profile corresponds to a  $TEM_{00}$  mode over the whole range of output energy when using the VBG.

We recorded an output spectra using an ANDO AQ6317B (Yokogawa Corp. of America, GA) optical spectrum analyzer (OSA) for an injected DPRA and a DPRA without injection with the same number of round-trips (21). In each case the pump diode current has been adjusted to achieve cavity dumping at the maximum of the intracavity pulse-buildup dynamics. An unseeded DPRA with a mirror produces the gain-narrowed ASE spectrum shown in Fig. 110.48 (solid line) with an ASE

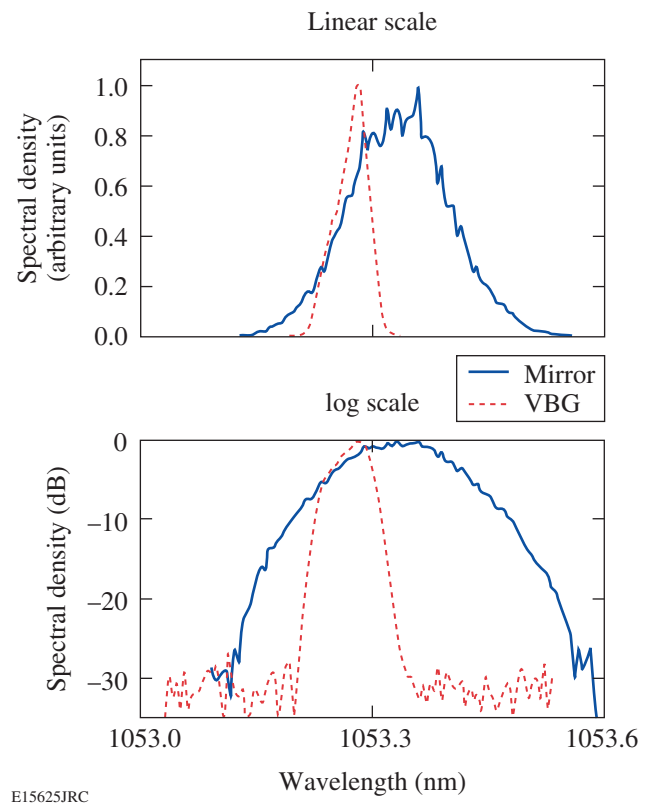


Figure 110.48 Output spectra for the DPRA without injection: the DPRA with a mirror produces a gain-narrowed ASE spectrum with 150-pm FWHM (solid line); the DPRA with the VBG spectrum is narrowed to 43-pm FWHM (dashed line). In the latter case, the spectrum width and shape are defined by the common action of the VBG reflection curve and Nd:YLF gain profile. In both cases DPRA performance has been optimized for cavity dumping after 21 cavity roundtrips.

bandwidth of 150 pm (FWHM). In contrast, the unseeded DPRA using the VBG shown in Fig. 110.48 (dashed line) provides a much narrower spectrum with a width (43-pm FWHM) and shape defined by the common action of the VBG reflection curve and Nd:YLF gain profile. The position of the output spectrum is defined by the VBG angular alignment. The VBG in the DPRA cavity is aligned using an injection laser in cw mode as an alignment beam, i.e., the VBG position provides the best DPRA cavity alignment (maximum VBG reflectivity) for the wavelength that is going to be injected. This injection wavelength is not exactly at the peak of the DPRA gain curve, leading to the asymmetric spectrum shape when using the VBG in a DPRA without injection.

Observing the VBG spectral-filtering effect is limited by an instrument spectral resolution and dynamic range of 20 pm and 40 dB, respectively. We have simulated the DPRA spectral behavior as it will be seen by the OSA to determine experimental conditions for reliable observation of the VBG spec-

tral-filtering effect. Our simulations show that DPRA injection energy must be about equal to ASE energy. The injected pulse energy in this case is  $\sim 0.0025$  pJ, which corresponds to a gross gain of greater than  $10^{12}$ . The simulated output spectrum of the DPRA with the mirror is shown in Fig. 110.49(a); the simulated output spectrum consists of an injected line on top of an ASE pedestal, which is reliably recorded by the OSA. The measured output spectra are shown in Fig. 110.49(b) and agree very well with the simulated results. The number of round-trips for both simulated and experimental results is 21. In the DPRA with the VBG + mirror combination (even at this very low injection level), the ASE in the output spectrum [shown in Fig. 110.49(b) (dashed line)] is suppressed to the instrument's 40-dB dynamic range. The OSA spectral resolution does not allow us to make the spectra comparison at higher levels of DPRA injection; however, it is obvious that spectral contrast will be even better when the injection level is increased due to domination of the injected pulse over ASE even on initial cavity round-trips.

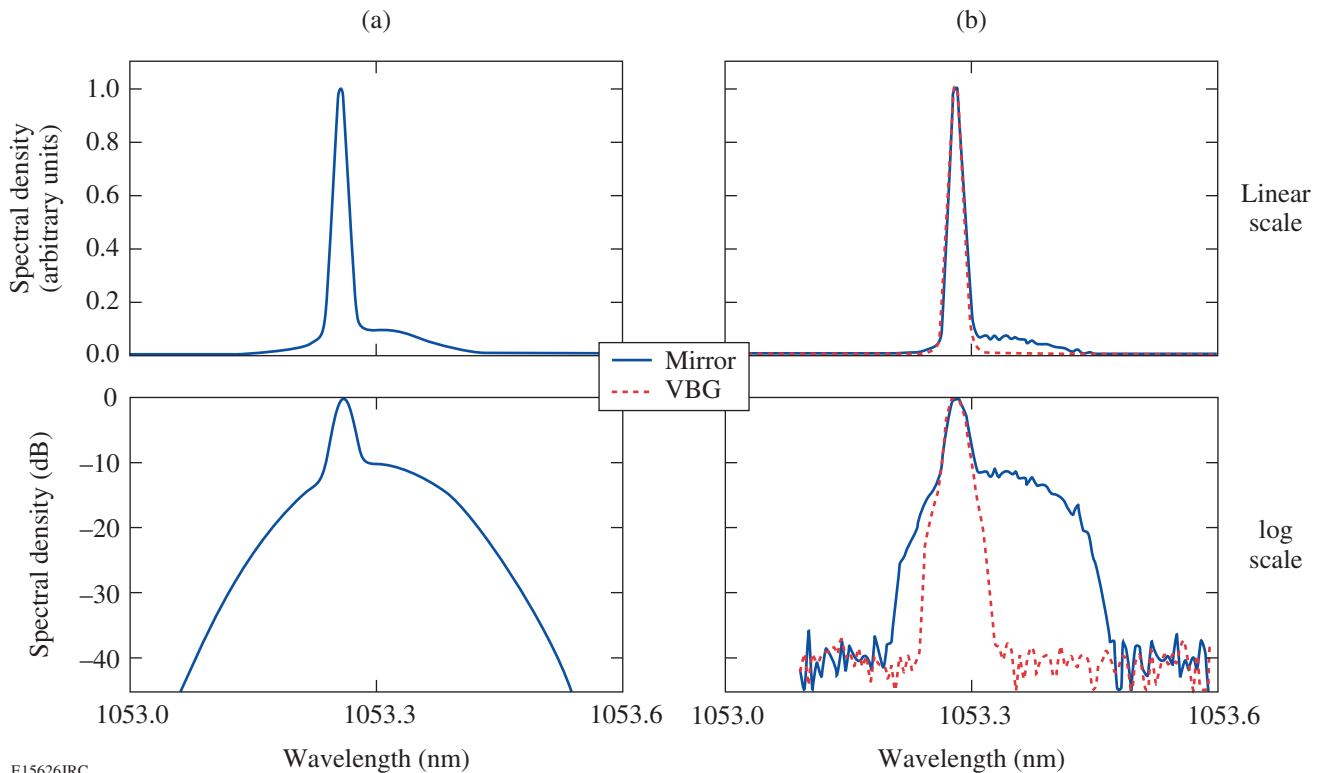


Figure 110.49

(a) Simulations show that for a reliable OSA recording of ASE filtering effect, the injected energy must be about equal to the DPRA ASE (in this case  $E_{\text{ASE}} = 0.7 E_{\text{in}}$ ). (b) Output spectra for the DPRA with injected pulse energy of 0.0025 pJ, comparable to DPRA ASE: with the mirror (solid line) a significant ASE pedestal is observed; with the VBG (dashed line), the spectrum does not show any presence of ASE. The number of round-trips (21) is the same for all cases.

## Conclusion

We have demonstrated a VBG spectrally filtered DPRA operation for the first time. Using VBG as the DPRA resonator spectrally selective element allows out-of-band ASE suppression even for a very low DPRA injection level. Using DPRA with VBG spectral filtering can be beneficial in high-energy laser amplifiers.

## ACKNOWLEDGMENT

This work was supported by the U.S. Department of Energy Office of Inertial Confinement Fusion under Cooperative Agreement No. DE-FC52-92SF19460, the University of Rochester, and the New York State Energy Research and Development Authority. The support of DOE does not constitute an endorsement by DOE of the views expressed in this article. Reflective Bragg gratings were developed at OptiGrate under DARPA Contract No. W31P4Q04CR157.

## REFERENCES

1. L. B. Glebov *et al.*, in *Laser Weapons Technology III*, edited by W. E. Thompson and P. H. Merritt (SPIE, Bellingham, WA, 2002), Vol. 4724, pp. 101–109.
2. G. B. Venus *et al.*, *Opt. Lett.* **31**, 1453 (2006).
3. Y. Kaneda *et al.*, *IEEE Photonics Technol. Lett.* **18**, 1795 (2006).
4. B. Jacobsson, V. Pasiskevicius, and F. Laurell, *Opt. Lett.* **31**, 1663 (2006).
5. A. Dergachev *et al.*, in *Conference on Lasers and Electro-Optics/ Photonic Applications, Systems and Technologies Conference (CLEO/ PhAST 2004)*, OSA Technical Digest (Optical Society of America, Washington, DC, 2004), p. CThZ3.
6. T. Chung *et al.*, *Opt. Lett.* **31**, 229 (2006).
7. B. Jacobsson *et al.*, *Opt. Lett.* **30**, 2281 (2005).
8. K.-H. Liao *et al.*, *Opt. Express* **15**, 4876 (2007).
9. W. Koechner, *Solid-State Laser Engineering*, 4th rev. ed., Springer Series in Optical Sciences, Vol. 1 (Springer, Berlin, 1996), p. 182.
10. N. Forget *et al.*, *Opt. Lett.* **30**, 2921 (2005).
11. V. Bagnoud, M. J. Guardalben, J. Puth, J. D. Zuegel, T. Mooney, and P. Dumas, *Appl. Opt.* **44**, 282 (2005).
12. A. V. Okishev and J. D. Zuegel, *Appl. Opt.* **43**, 6180 (2004).
13. A. V. Okishev, M. D. Skeldon, and W. Seka, in *Advanced Solid-State Lasers*, edited by M. M. Fejer, H. Injeyan, and U. Keller, OSA TOPS, Vol. 26 (Optical Society of America, Washington, DC, 1999), pp. 228–235.

---

# Impact of Transverse Spatial-Hole Burning on Beam Quality in Large-Mode-Area Yb-Doped Fibers

## Introduction

In recent years fiber lasers and amplifiers have been widely used in high-power applications such as material processing and industrial manufacturing. Their main advantages are heat-dissipation capability, broad gain bandwidth, compactness, robustness, and high efficiency. The primary limitation in their power scaling is the onset of nonlinear effects, including stimulated Brillouin scattering (SBS) and stimulated Raman scattering (SRS).<sup>1</sup> This limitation can be significantly mitigated by the adoption of large-mode-area (LMA) fibers due to the resulting reduction in intensity. The damage threshold is also increased for LMA fibers. However, increasing the mode area in traditional step-index fibers will introduce higher-order transverse modes and therefore degrade the beam quality. The optimization of the beam quality in LMA fibers has been a subject of intense research.<sup>2-9</sup>

Many designs of LMA fibers for high-power applications have been developed for beam-quality control. Design aspects have included internal structure designs such as photonic crystal fibers and helical-core fibers;<sup>2-4</sup> external structure designs such as coiled multimode fibers;<sup>5</sup> refractive-index designs such as low-numerical-aperture (NA), single-mode fibers and ring-shaped index fibers;<sup>6,7</sup> and gain dopant designs in multimode fibers.<sup>8,9</sup>

The impact, however, of transverse spatial-hole burning (TSHB) on beam quality has often been ignored. When a multimode optical beam with nonuniform transverse intensity is propagating in the fiber, the gain becomes more saturated where the intensity is highest. As the gain seen by each transverse mode changes, the net beam profile, and thus the beam quality, changes. At high powers, this effect becomes pronounced due to heavily saturated population inversion. To our knowledge, TSHB in LMA fibers has not yet been modeled.

In this article, the beam-quality factor is measured for an amplified spontaneous emission (ASE) source based on an ytterbium-doped LMA multimode fiber as a function of pump power. A localized multimode model is presented with

spatially resolved gain and a modal decomposition of the optical field. Numerical simulations are performed with this localized multimode model as well as a simplified model and compared to experimental results. The comparison validates the localized model and demonstrates the impact of TSHB on beam quality.

In the following sections, (1) the experimental setup and measured results are presented; (2) a localized multimode model is introduced and the equations to calculate beam-quality factor are presented; (3) the results of numerical simulations based on this model are compared to experimental results and extrapolated to higher power; (4) the validity of a simplified model that does not include TSHB is discussed; and (5) the theoretical models are further applied to fiber amplifiers. The main conclusions are presented in the last section.

## Experiment Configuration and Results

The experimental arrangement used for this work is shown schematically in Fig. 110.50. A fiber-coupled diode laser provided a maximum continuous-wave (cw) pump power of 9 W at 915 nm. The ytterbium-doped, dual-clad (YDDC) fiber was 7 m long with a core diameter of 30  $\mu\text{m}$ , an inner cladding diameter of 300  $\mu\text{m}$ , a core NA of 0.06, and an absorption rate of approximately 4 dB/m at 915 nm. While the back end of the fiber was angle cleaved to prevent reflection of the forward ASE, a dichroic mirror was set between two aspheric lenses to extract the backward ASE output light. A beam splitter in the output beam made it possible for the output power and the beam-quality factor ( $M^2$  parameter) to be measured simultaneously. The ASE output power was measured by a power meter, and the beam widths (defined as the second moment) were measured by a charge-coupled-device (CCD) camera placed at different distances.<sup>10</sup> Using a least-squares-fitting method,<sup>11</sup> the beam-quality factor in the  $x$  or  $y$  direction was calculated by fitting the beam widths and distances to a polynomial:<sup>10</sup>

$$W^2(z) = W_0^2 + M^4 \left( \frac{\lambda}{\pi W_0} \right)^2 (z - z_0)^2, \quad (1)$$

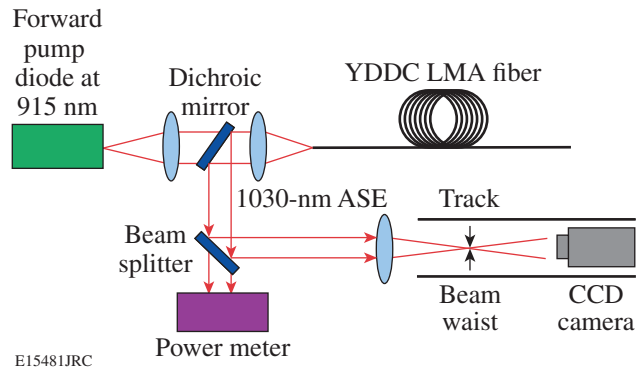


Figure 110.50  
Experimental configuration of the multimode-fiber ASE source.

where  $W(z)$  is the beam width at distances  $z$ ,  $W_0$  and  $z_0$  are the respective beam width and distance at the beam waist where the beam width has a minimum, and  $\lambda$  is wavelength.

The ASE output power is plotted as a function of pump power in Fig. 110.51. The figure shows that output power increases exponentially and quasi-linearly when the pump power is below and above  $\sim 7$  W, respectively, which means the saturation effect becomes apparent at 7-W pump power. We define this “soft” threshold as the pump threshold for saturation.

The beam-quality factor is plotted as a function of pump power in Fig. 110.52. It is instructive to note that the beam-quality factors are identical within experimental error in the  $x$  and  $y$  directions, as expected from symmetrical circular geometry. Compared with Fig. 110.51, Fig. 110.52 shows that the beam quality improves with pump power below the pump

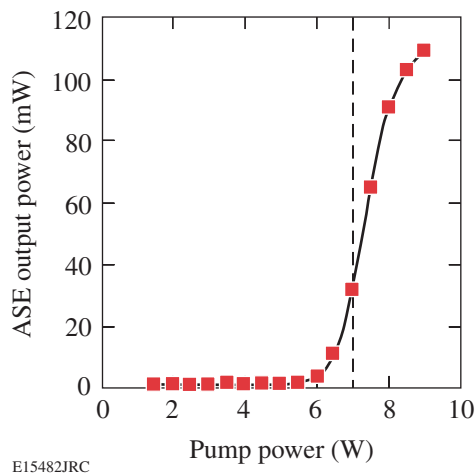


Figure 110.51  
Output power versus pump power from the ASE source. The dashed vertical line is the pump threshold for saturation.

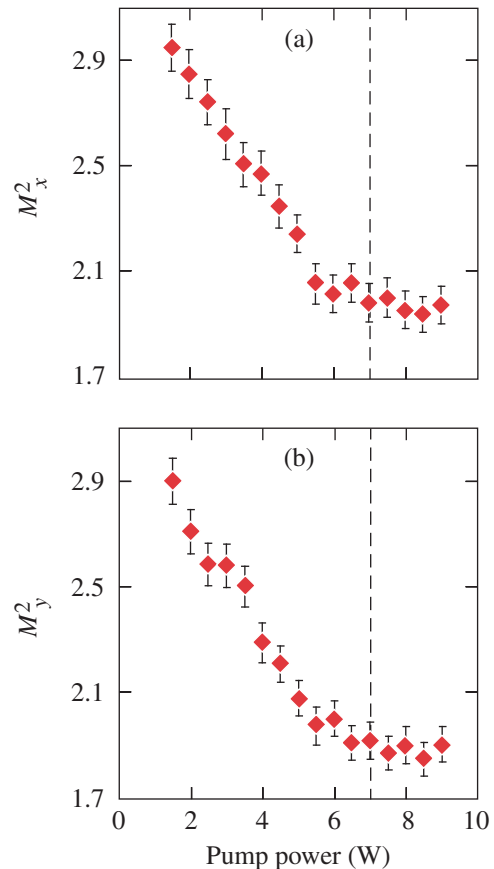


Figure 110.52  
The beam-quality factor of ASE source versus pump power in the (a)  $x$  direction and (b)  $y$  direction. The dashed vertical lines are the pump thresholds for saturation.

threshold for saturation and is nearly steady as the gain medium saturates. To fully understand the physics behind this beam-quality behavior, numerical simulations based on theoretical modeling have been developed.

### Localized Model and Beam-Quality Factor Calculation Method

Since the beam quality is related to the modal properties of the output beam, a model that can treat multiple transverse modes is required. A multimode model has been developed for dealing with multiple spectral modes in single-spatial-mode, rare-earth-doped fibers.<sup>12</sup> In this work, the model is extended to multi-transverse-spatial modes in multimode fibers for the first time.

The optical power is quantized into the transverse modes of the fiber, while the population inversion retains spatial dependence. In this way, TSHB can be accounted for while retaining

the simplicity and transparency of a mode-based picture. A similar treatment has also been developed for modeling vertical-cavity, surface-emitting lasers.<sup>13</sup>

The two-level rate equations are given by

$$\begin{aligned} \frac{dn_2(r, \phi, z)}{dt} = & \sum_k \frac{P_k(z) i_k(r, \phi) \sigma_{ak}}{h\nu_k} n_1(r, \phi, z) \\ & - \sum_k \frac{P_k(z) i_k(r, \phi) \sigma_{ek}}{h\nu_k} n_2(r, \phi, z) \\ & - \frac{n_2(r, \phi, z)}{\tau}, \end{aligned} \quad (2)$$

$$n_t(r, \phi, z) = n_1(r, \phi, z) + n_2(r, \phi, z), \quad (3)$$

where the mode order  $k$  denotes any combination of beam propagation direction (+, -), wavelength ( $\lambda$ ), transverse-mode order ( $\nu m$ ), and orientation (even, odd);  $n_1$ ,  $n_2$ , and  $n_t$  are ground-level, upper-level, and total ytterbium ion density, respectively, as a function of time and spatial coordinates;  $\sigma_a$  and  $\sigma_e$  are the absorption and emission cross sections of ytterbium ions, respectively; and  $\tau$  is the upper-state lifetime.

$P_k(z)$ , the power of the  $k^{\text{th}}$  mode at position  $z$  in the fiber, is the integration of the light-intensity distribution  $I_k(r, \phi, z)$  over the radial and azimuthal coordinates:

$$P_k(z) = \int_0^{2\pi} \int_0^{\infty} I_k(r, \phi, z) r dr d\phi. \quad (4)$$

The normalized modal-intensity distribution  $i_k(r, \phi)$  is defined as

$$i_k(r, \phi) = I_k(r, \phi, z) / P_k(z) \quad (5)$$

and is determined by the spatial shape of the mode and therefore independent of  $z$ .

The terms on the right side of Eq. (2) describe the effects of absorption, stimulated emission, and spontaneous emission, respectively. Note that the interference terms are neglected in this model. This assumption is correct for transverse modes of

ASE because they do not interfere with each other due to their lack of coherence. For a coherent multimode beam, this model could be modified by adding the interference terms. Mode coupling and scattering in the fiber are not considered.

In the steady-state case, the time derivative in Eq. (2) is set to zero and the inversion is solved as

$$n_2(r, \phi, z) = n_t \frac{\sum_k \frac{P_k(z) i_k(r, \phi) \sigma_{ak}}{h\nu_k}}{\frac{1}{\tau} + \sum_k \frac{P_k(z) i_k(r, \phi) (\sigma_{ak} + \sigma_{ek})}{h\nu_k}}. \quad (6)$$

The numerator accounts for small signal gain and the summation in the denominator accounts for TSHB.

The propagation equations are given by

$$\begin{aligned} \frac{dP_k(z)}{dz} = & u_k \sigma_{ek} \left[ P_k(z) + m h \frac{c^2}{\lambda_k^3} \Delta\lambda_k \right] \\ & \times \int_0^{2\pi} \int_0^a i_k(r, \phi) n_2(r, \phi, z) r dr d\phi \\ & - u_k \sigma_{ak} P_k(z) \int_0^{2\pi} \int_0^a i_k(r, \phi) n_1(r, \phi, z) \\ & \times r dr d\phi - u_k \alpha P_k(z). \end{aligned} \quad (7)$$

where  $u_k = 1$  for the modes traveling in the forward direction or  $u_k = -1$  in the backward direction,  $m$  is the number of polarizations of each mode,  $\Delta\lambda_k$  is the bandwidth, and  $\alpha$  is the fiber-loss term. The terms on the right side of Eq. (7) describe the effects of stimulated emission, spontaneous emission, absorption, and scattering loss, respectively.

The ASE and pump have different optical properties. The modes of ASE propagate in the fiber in both directions, but the pump propagates only in the forward direction. The bandwidth of ASE is relatively narrow, so the ASE is simplified as a single spectral mode. The pump light is considered to be a single spectral mode with  $\Delta\lambda_k = 0$  (no spontaneous emission at the pump wavelength).

Under the weakly guided approximation, the transverse modes of ASE can be represented by linearly polarized (LP) modes.<sup>14</sup> For the LP<sub>*νm*</sub> mode, the normalized optical intensity  $i_{\nu m}(r, \phi)$  and the normalized electrical field distribution  $E_{\nu m}(r, \phi)$  can be written as

$$i_{\nu m}(r, \phi) = E_{\nu m}^2(r, \phi), \quad (8)$$

$$E_{\nu m}(r, \phi) = \begin{cases} bJ_{\nu}(\kappa_{\nu m}r)f_{\nu}(\phi) & r < a_{\text{core}} \\ \frac{J_{\nu}(\kappa_{\nu m}a_{\text{core}})K_{\nu}(\gamma_{\nu m}r)f_{\nu}(\phi)}{bK_{\nu}(\gamma_{\nu m}a_{\text{core}})} & r \geq a_{\text{core}} \end{cases}, \quad (9)$$

where  $\nu$  and  $m$  are the azimuthal and radial mode numbers, respectively;  $J_{\nu}$  and  $K_{\nu}$  are the Bessel function of the first kind and modified Bessel function of the second kind, respectively;  $a_{\text{core}}$  is the radius of the core; and  $b$  is the normalization coefficient of the electrical field.

The transverse attenuation coefficient of the mode in the inner cladding  $\gamma_{\nu m}$  and the transverse wave vector  $\kappa_{\nu m}$  are solutions of the following system of equations:<sup>15</sup>

$$\kappa_{\nu m} \frac{J_{\nu-1}(\kappa_{\nu m}a_{\text{core}})}{J_{\nu}(\kappa_{\nu m}a_{\text{core}})} = -\gamma_{\nu m} \frac{K_{\nu-1}(\gamma_{\nu m}a_{\text{core}})}{K_{\nu}(\gamma_{\nu m}a_{\text{core}})}, \quad (10)$$

$$\kappa_{\nu m}^2 + \gamma_{\nu m}^2 = V^2/a_{\text{core}}^2. \quad (11)$$

The  $V$  number and NA are defined as

$$V = \frac{2\pi}{\lambda} a_{\text{core}} \text{NA}, \quad (12)$$

$$\text{NA} = \sqrt{n_{\text{core}}^2 - n_{\text{clad}}^2}, \quad (13)$$

where  $\lambda$  is the wavelength and  $n_{\text{core}}$  and  $n_{\text{clad}}$  are the refractive indexes in the core and cladding, respectively.

The azimuthal component  $f_{\nu}(\phi)$  is equal to 1 for those transverse modes with zero azimuthal mode number and is given by

$$f_{\nu}(\phi) = \begin{cases} \cos(\nu\phi) & \text{even} \\ \sin(\nu\phi) & \text{odd} \end{cases} \quad (14)$$

for the other transverse modes with even or odd orientation.

Since the area of the inner cladding is much larger than the core, the highly multimode pump light can be simplified as one transverse mode effectively being uniformly distributed across the inner cladding and the core, which means the intensity distribution of pump  $I_{\text{pump}}$  and normalized intensity distribution of pump  $i_{\text{pump}}$  can be considered independent of radial and azimuthal coordinates. The normalized intensity distribution of the pump in inner cladding and core is then obtained from Eqs. (4) and (5) by

$$i_{\text{pump}} = \frac{1}{\pi a_{\text{clad}}^2}, \quad (15)$$

where  $a_{\text{clad}}$  is the radius of inner cladding.

The output power is the sum of the backward output power contained in each mode and is given by

$$P_{\text{output}} = \sum_{\nu, m} P_{\nu m}^{-}(0). \quad (16)$$

The output-fraction factor  $\alpha_{\nu m}$  of LP<sub>*νm*</sub> mode is defined as

$$\alpha_{\nu m} = P_{\nu m}^{-}/P_{\text{output}}. \quad (17)$$

The transverse modes with the same mode numbers but different orientations will have the same fraction factor for ASE due to symmetry.

The beam-quality factor of an optical beam can be calculated given the electrical field distribution.<sup>16</sup> Since the electrical field of ASE is real and symmetric at the output end and without inference, many terms in the equations to calculate the beam-quality factors vanish. The equations can then be simplified as

$$M_x^2 = 2 \left[ \left( \iint \sum_{\nu, m} \alpha_{\nu m} \left| \frac{\partial E_{\nu m}(r, \phi)}{\partial x} \right|^2 r dr d\phi \right) \times \left( \iint x^2 \sum_{\nu, m} \alpha_{\nu m} |E_{\nu m}(r, \phi)|^2 r dr d\phi \right) \right]^{1/2}, \quad (18)$$

$$M_y^2 = 2 \left( \iint \sum_{v,m} \alpha_{vm} \left| \frac{\partial E_{vm}(r, \phi)}{\partial y} \right|^2 r dr d\phi \right) \times \left( \iint y^2 \sum_{v,m} \alpha_{vm} |E_{vm}(r, \phi)|^2 r dr d\phi \right)^{1/2}. \quad (19)$$

### Numerical Simulations and Discussions

Initial boundary conditions are needed to solve the propagation Eq. (7) and are specified at  $z = 0$  and  $z = L$  as

$$\begin{aligned} P_{\text{pump}}^+(0) &= P_0, \\ P_{\text{pump}}^-(L) &= 0, \\ P_{vm}^+(0) &= 0, \\ P_{vm}^-(L) &= 0, \end{aligned} \quad (20)$$

where  $P_0$  is the forward pump power injected into the fiber and  $L$  is the length of the fiber. For ASE sources, the input signal is zero.

The parameters used in numerical simulation are listed in Table 110.VII. The emission and absorption cross sections for the fiber used in the experiment are unknown and therefore cited from another fiber with similar parameters.<sup>17</sup> Although the value of the bandwidth of ASE  $\Delta\lambda_{\text{ASE}}$  does not affect the simulation result significantly, it is set to make the output power from simulation match that from experiment.

Given the initial boundary conditions, the propagation Eq. (7) is resolved by standard numerical integration techniques. The ASE output power and the output-fraction factors are obtained by Eqs. (16) and (17), and then the beam-quality factor is calculated by Eqs. (18) and (19). The ASE output power, the output-fraction factors, and the beam-quality factor as functions of pump power up to 25 W are calculated and plotted in Figs. 110.53, 110.54, and 110.55, respectively.

Compared with Fig. 110.51, Fig. 110.53 shows that the calculated output power has the same behavior as that from the experiment with a slightly larger value, which may result from the discrepancy between the cross sections used in simulation and experiment or over-estimation of pump power since coupling efficiency is not included in the model. The

pump threshold for saturation is about 7.5 W, close to experimental results.

Figure 110.54 shows that all of the transverse modes have nearly the same output-fraction factors at very low pump power. The output-fraction factors of lower-order modes (LP<sub>01</sub> and LP<sub>11</sub> in this case) increase with pump power while those of higher-order modes (LP<sub>01</sub>, LP<sub>11</sub>, and LP<sub>31</sub> in this case)

Table 110.VII: Parameters used in simulations.

Parameter	Value
$n_t$	$1.45 \times 10^{26} \text{ m}^{-3}$
$\lambda_{\text{ASE}}$	1030 nm
$\lambda_{\text{pump}}$	915 nm
$\sigma_a \text{ ASE}$	$4.88 \times 10^{-26} \text{ m}^2$
$\sigma_e \text{ ASE}$	$6.24 \times 10^{-25} \text{ m}^2$
$\sigma_a \text{ pump}$	$8.21 \times 10^{-25} \text{ m}^2$
$\sigma_e \text{ pump}$	$3.04 \times 10^{-26} \text{ m}^2$
$\tau$	0.84 ms
$\Delta\lambda_{\text{ASE}}$	5 nm
$m$	2
$L$	7 m
$a_{\text{core}}$	15 $\mu\text{m}$
$a_{\text{clad}}$	150 $\mu\text{m}$
NA	0.06
$\alpha$	$0.003 \text{ m}^{-1}$

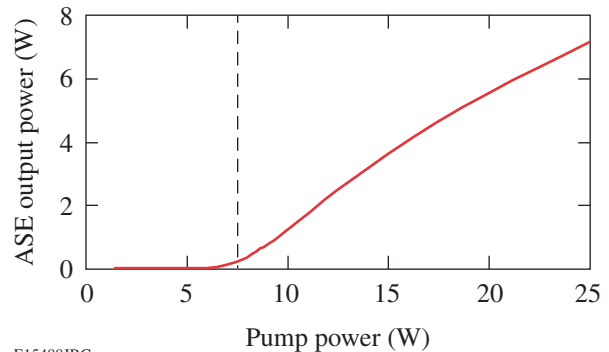


Figure 110.53

ASE output power versus pump power from the localized model. The dashed vertical line is the pump threshold for saturation.

decrease. Most importantly, the lower-order modes maximize near the pump threshold for saturation, while the higher-order modes minimize.

From Eqs. (18) and (19), it is obvious that the output-fraction factors determine the beam-quality factor since the beam-quality factor of each LP transverse mode is fixed. Generally speaking, lower-order modes have a smaller beam-quality factor, while the higher-order modes have a larger beam-quality factor.<sup>16</sup> So the beam-quality factor decreases, minimizes, and increases when the output fractions of lower-order modes increase, maximize, and decrease, respectively.

This behavior is manifest in Fig. 110.55, which shows that the beam-quality factor decreases with increasing pump power below pump threshold for saturation as shown experimentally in Fig. 110.52. The calculation further shows that the nearly

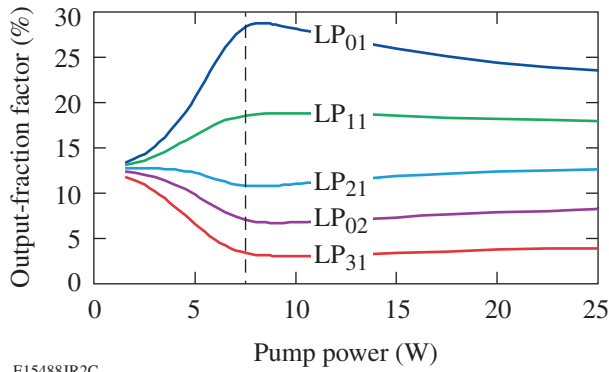


Figure 110.54 Output-fraction factors of LP fiber modes versus pump power from the localized model. The dashed vertical line is the pump threshold for saturation.

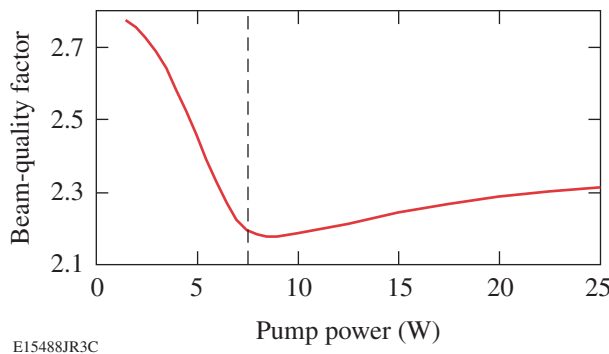


Figure 110.55 Beam-quality factor versus pump power from the localized model. The dashed vertical line is the pump threshold for saturation.

steady part near pump threshold for saturation in Fig. 110.52 is a minimum. The behavior of the beam-quality factor follows directly from the behavior of output-fraction factors as shown in Fig. 110.55. The output-fraction factors, and thus the beam-quality factor, are determined by how much gain is experienced by each transverse mode, which depends on the overlap of mode field distribution and population inversion distribution.

The upper-level dopant distribution across the injection fiber end for various pump powers is plotted in Fig. 110.56. When 5-W pump power is below the pump threshold for saturation, the population inversion is nearly uniform across the core, so the modal gain is nearly proportional to the fraction of the mode in the core. Since the fields of lower-order modes are more confined in the core, the lower-order modes have larger gain than the higher-order modes, as shown in Table 110.VIII. In this small-signal regime, the power in the modes with larger gain increases faster than in the modes with smaller gain. Therefore, the output-fraction factors of lower-order modes increase and the beam quality improves.

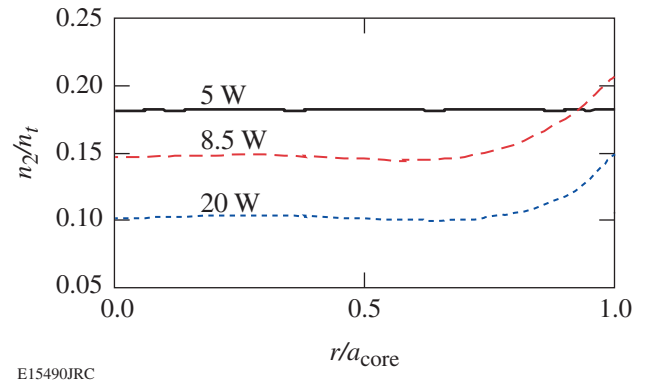


Figure 110.56 Upper-level dopant distributions with various pump powers across the injection fiber end.

Table 110.VIII: The ratio of the gain seen by other transverse modes to the gain seen by the fundamental mode with 5-W pump power.

Mode	$g_{LP_{vm}}/g_{LP_{01}}$
LP <sub>11</sub>	95.6%
LP <sub>21</sub>	89.8%
LP <sub>02</sub>	85.4%
LP <sub>31</sub>	78.0%

Above the pump threshold for saturation, TSHB is shown in the upper-level dopant distribution with 8.5- and 20-W pump power in Fig. 110.56, where the gain profile is much more saturated in the center of the core than on the edge. Since lower-order modes are more concentrated in the center of the core, the gain of lower-order modes decreases relative to the gain of higher-order modes. In the saturation region, the faster the gain in the modes decreases, the slower the power in the modes increases. So under the impact of TSHB the output-fraction factors of lower-order modes decrease and the beam quality degrades.

### The Validity of a Simplified Model

The rate and propagation equations are often simplified by replacing transverse space integrals with overlap integrals, especially in single-mode fibers.<sup>18</sup> The validity of such simplification in multimode fibers is discussed below.

The rate equations of such a simplified model are given by

$$\frac{dn_2(z)}{dt} = \sum_k \frac{P_k(z)\Gamma_k\sigma_{ak}}{h\nu_k A} n_1(z) - \sum_k \frac{P_k(z)\Gamma_k\sigma_{ek}}{h\nu_k A} n_2(z) - \frac{n_2(z)}{\tau}, \quad (21)$$

$$n_t(z) = n_1(z) + n_2(z), \quad (22)$$

where  $n_1$  and  $n_2$  represent average ground-level and upper-level ytterbium ion density across the fiber cross section, respectively,  $A$  is the area of the core cross section, and  $\Gamma_k$  is the overlap integral between the mode and dopants.

The overlap integral of ASE modes is given by

$$\Gamma_{vm} = \frac{\int_0^{2\pi} \int_0^{\infty} i_{vm}(r, \phi) n_t(r, \phi, z) r dr d\phi}{\int_0^{2\pi} \int_0^{\infty} n_t(r, \phi, z) r dr d\phi}. \quad (23)$$

If the dopant is distributing uniformly in the fiber core,  $\Gamma_{vm}$  depends only on the mode field and can be simplified as

$$\Gamma_{vm} = \int_0^{2\pi} \int_0^{a_{core}} i_{vm}(r, \phi) r dr d\phi. \quad (24)$$

The overlap integral of pump is given by

$$\Gamma_{pump} = a_{core}^2 / a_{clad}^2. \quad (25)$$

In the steady-state case,  $n_2$  is solved as

$$n_2(z) = n_t \frac{\sum_k \frac{P_k(z)\Gamma_k\sigma_{ak}}{h\nu_k A}}{\frac{1}{\tau} + \sum_k \frac{P_k(z)\Gamma_k(\sigma_{ak} + \sigma_{ek})}{h\nu_k A}}. \quad (26)$$

Since the upper-level dopant distribution depends only on the longitudinal coordinate  $z$  and is independent of radial and azimuthal coordinates, TSHB is not included in the simplified model. The saturation effect is included as an averaged level across the core.

The simplified propagation equation is given by

$$\frac{dP_k(z)}{dz} = u_k \sigma_{ek} \left[ P_k(z) + mh \frac{c^2}{\lambda_k^3} \Delta\lambda_k \right] \Gamma_k n_2(z) - u_k \sigma_{ak} P_k(z) \Gamma_k n_1(z) - u_k \alpha P_k(z). \quad (27)$$

Given the same initial boundary conditions as Eq. (20), the propagation equation (27) is resolved. The output power as a function of pump power is the same in the simplified model as the localized model; however, the modal properties are significantly different. The output-fraction factors and beam-quality factor as functions of pump power up to 25 W in the simplified model compared to the localized model are shown in Figs. 110.57 and 110.58.

Figure 110.57 shows that the output-fraction factors in the simplified model are the same as those in the localized model when the pump power is below the pump threshold for saturation. However, the output-fraction factors of lower-order modes in the simplified model keep increasing beyond the pump threshold for saturation, becoming constant after 15 W. Similarly, Fig. 110.58 shows that the beam-quality factor in the

simplified model is the same as that in the localized model at pump power below pump threshold for saturation. Above the pump threshold for saturation, however, the beam-quality factor in the simplified model keeps decreasing until 15 W and then becomes constant.

The behaviors of output-fraction factors and beam-quality factor are consistent and can be explained as follows: In the simplified model, the gain seen by each transverse mode is always proportional to the fraction of the mode in the core, so the simplified model gives the same simulation results as the localized model below the pump threshold of saturation. Above the pump threshold for saturation, the gain of each mode decreases at the same rate, so the power in each mode increases

at the same rate. Therefore, the output-fraction factor of each mode becomes constant, as does the beam-quality factor.

The beam-quality factors from simulation results of both models and the experimental results near pump threshold for saturation are compared in Fig. 110.59. Figure 110.59 shows that the beam-quality factor of the simplified model does not plateau like the experiment data, but the localized model predicts this behavior. The failure to show the minimum of beam-quality factor near pump threshold for saturation proves that the simplified model is not valid and TSHB is required to model LMA multimode fibers when dealing with beam quality.

**Fiber Amplifiers**

Fiber amplifiers are more important than ASE sources in high-power applications of LMA fibers. As mentioned in **Localized Model and Beam-Quality Factor Calculation Method** (p. 121), the localized model assumes no interference, which is true for an optical beam from incoherent sources like ASE, but not for coherent sources like fiber amplifiers. While the equations could be easily modified to include the interference terms, the relative phases between modes create a large additional parameter space that would require exploration. The calculations that follow neglect these interference terms since the additional complication does not aid in underscoring the importance of TSHB.

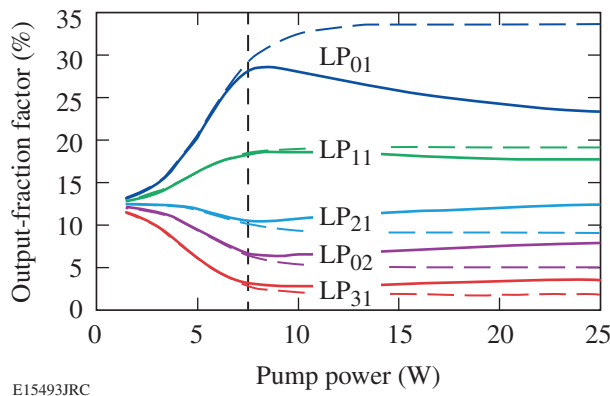


Figure 110.57 Output-fraction factors of LP fiber modes versus pump power from localized (solid) and simplified (dashed) models. The dashed vertical line is the pump threshold for saturation.

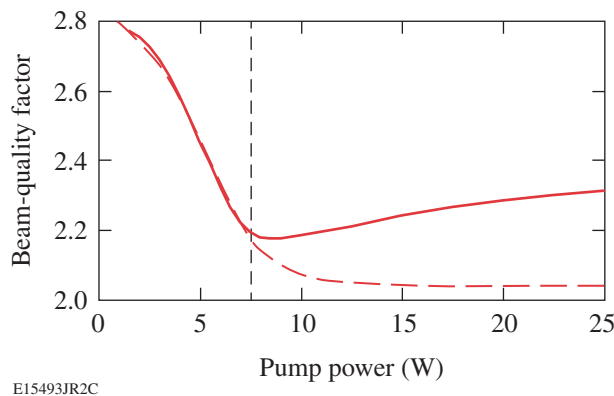


Figure 110.58 Beam-quality factor versus pump power from localized (solid) and simplified (dashed) models. The dashed vertical line is the pump threshold for saturation.

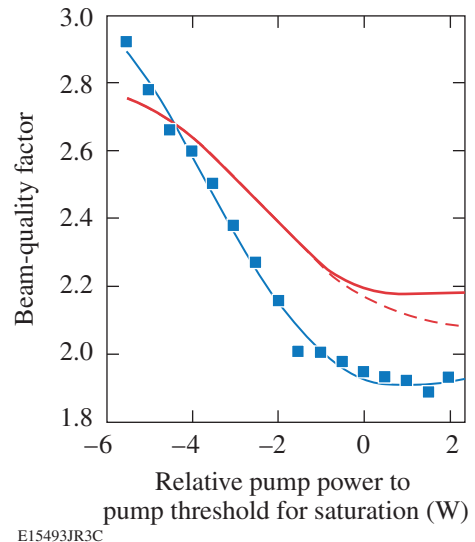


Figure 110.59 Beam-quality factor versus relative pump power to pump threshold for saturation from localized (solid) and simplified (dashed) models as well as experimental measurements (squares with solid-line fit).

For the purpose of simplicity, only the LP<sub>01</sub> and LP<sub>11</sub> modes are assumed to be coupled into the fiber amplifier. The power contained in the LP<sub>11</sub> mode is assumed to be evenly distributed in two orientations.

The initial boundary conditions are changed to

$$\begin{aligned}
 P_{\text{pump}}^+(0) &= P_0, \\
 P_{\text{pump}}^-(L) &= 0, \\
 P_{01}^+(0) &= P_s \chi, \\
 P_{11}^+(0) &= P_s(1 - \chi), \\
 P_{vm}^+(0) &= 0, \text{ otherwise} \\
 P_{vm}^-(L) &= 0,
 \end{aligned} \tag{28}$$

where  $P_s$  is the total signal power and  $\chi$  is the input-fraction factor of the LP<sub>01</sub> mode.

The normalized electrical field distribution of the output beam can be written as

$$E(r, \phi) = \sum_{v,m} \sqrt{\alpha_{vm}} E_{vm}(r, \phi) e^{-i\beta_{vm}L}, \tag{29}$$

where the propagation coefficient  $\beta_{vm}$  is given by<sup>15</sup>

$$\beta_{vm}^2 = \left(\frac{2\pi}{\lambda}\right)^2 n_{\text{core}}^2 - \kappa_{vm}^2. \tag{30}$$

In this form, modal dispersion is included. No initial phase difference is considered between the modes since the two modes are assumed to be excited by a single-mode input beam (for example, by misalignment).

Since the output beam is real and symmetrical, the equations to calculate the beam-quality factors in Ref. 16 can be simplified as

$$M_x^2 = 2 \sqrt{\left[ \iint \left| \frac{\partial E(r, \phi)}{\partial x} \right|^2 \right] \left[ \iint x^2 |E(r, \phi)|^2 r dr d\phi \right]}, \tag{31}$$

$$M_y^2 = 2 \sqrt{\left[ \iint \left| \frac{\partial E(r, \phi)}{\partial y} \right|^2 \right] \left[ \iint y^2 |E(r, \phi)|^2 r dr d\phi \right]}. \tag{32}$$

The new parameters used in the simulation and those that differ from Table 110.VII are listed in Table 110.IX:  $\lambda_s$  is the wavelength of the signal,  $\Delta\lambda_{\text{ASE}}$  is set to be the same as the bandwidth of the signal, and  $P_0$  is set far above the pump threshold for saturation, which is true in most high-power applications.

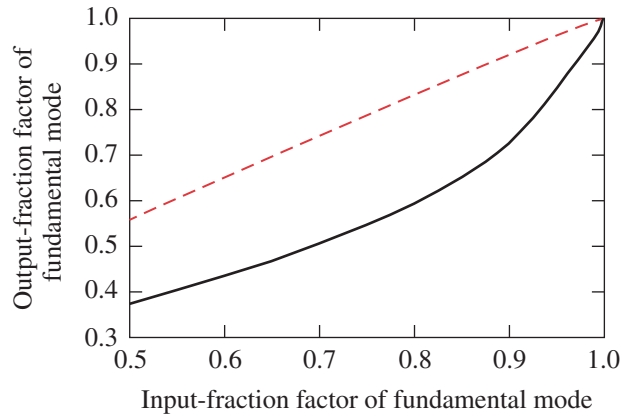
Table 110.IX: New and changed parameters used in simulations.

Parameter	Value
$\lambda_s$	1030 nm
$P_s$	10 W
$n_{\text{core}}$	1.5
$\Delta\lambda_{\text{ASE}}$	0.1 nm
$P_0$	1.5 kW

The calculations show that the output power is nearly the same in both models and does not change as the input-fraction factor. For both models, the output-fraction factor of the fundamental mode and the beam-quality factor are calculated as a function of the input-fraction factor of the LP<sub>01</sub> mode from 0.5 to 1 (shown in Figs. 110.60 and 110.61).

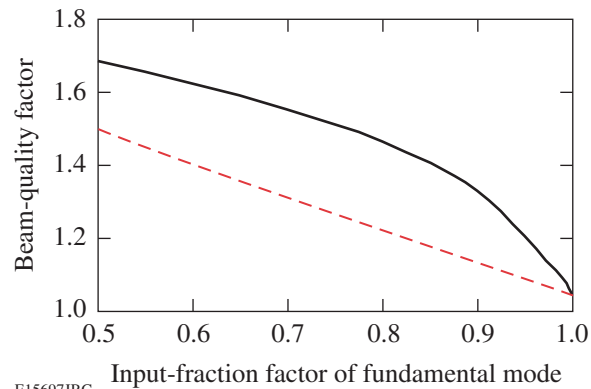
Figure 110.60 shows that the output-fraction factor of the fundamental mode in the localized model is smaller than the corresponding input-fraction factor, while the output-fraction factor of the fundamental mode in the simplified model is larger. These behaviors can be explained as follows: The pump power used in the simulations is well above pump threshold for saturation. In the localized model, the gain of fundamental mode is less than that of the LP<sub>11</sub> mode due to the effect of TSHB. Therefore, the fundamental mode is amplified less than the LP<sub>11</sub> mode, leading to a smaller output-fraction factor of the fundamental mode. In the simplified model, however, TSHB is ignored and the gain of fundamental mode is always larger than that of the LP<sub>11</sub> mode. In this case, the fundamental mode is always amplified more than the LP<sub>11</sub> mode, leading to a larger output-fraction factor of the fundamental mode.

Figure 110.61 shows that the beam-quality factor in the simplified model is underestimated by as much as 15% compared to the localized model due to underestimation of the output-fraction factor of the fundamental mode. This significant difference underscores the importance of TSHB on beam quality in LMA fiber amplifiers for high-power applications.



E15696JRC

Figure 110.60  
Output-fraction factors of the fundamental mode versus input-fraction factors of the fundamental mode from localized (solid) and simplified (dashed) models.



E15697JRC

Figure 110.61  
Beam-quality factors versus pump power from localized (solid) and simplified (dashed) models.

## Conclusions

In conclusion, the importance of TSHB on the beam quality of LMA multimode fibers was revealed through measurements and simulations. The measured beam-quality factor decreases until the gain becomes saturated in an ASE source based on an ytterbium-doped, large-mode-area, multimode fiber. Numerical simulation trends based on a model using spatially resolved gain and transverse-mode decomposition of the optical field

agree with the experimental results. A simplified model without TSHB is shown not fit to predict the observed behavior of beam quality in LMA fibers, especially at high powers. A comparison of both models shows that TSHB is also critical for properly modeling beam quality in LMA fiber amplifiers.

## ACKNOWLEDGMENT

This work was supported by the U.S. Department of Energy Office of Inertial Confinement Fusion under Cooperative Agreement No. DE-FC52-92SF19460, the University of Rochester, and the New York State Energy Research and Development Authority. The support of DOE does not constitute an endorsement by DOE of the views expressed in this article.

## REFERENCES

1. G. P. Agrawal, *Nonlinear Fiber Optics* (Academic Press, Boston, 1989).
2. T. A. Birks, J. C. Knight, and P. St. J. Russell, *Opt. Lett.* **22**, 961 (1997).
3. P. Wang *et al.*, *Opt. Lett.* **31**, 226 (2006).
4. Z. Jiang and J. R. Marciante, *J. Opt. Soc. Am. B* **23**, 2051 (2006).
5. P. Kopolow, D. A. V. Kliner, and L. Goldberg, *Opt. Lett.* **25**, 442 (2000).
6. D. Taverner *et al.*, *Opt. Lett.* **22**, 378 (1997).
7. H. L. Offerhaus *et al.*, *Opt. Lett.* **23**, 1683 (1998).
8. J. M. Sousa and O. G. Okhotnikov, *Appl. Phys. Lett.* **74**, 1528 (1999).
9. J. R. Marciante, presented at ASSP 2007, Vancouver, Canada, 28–31 January 2007.
10. A. E. Siegman, in *Diode Pumped Solid State Lasers: Applications and Issues*, edited by M. W. Dowley, OSA TOPS, Vol. 17 (Optical Society of America, Washington, DC, 1998), pp. 184–199.
11. P. R. Bevington, *Data Reduction and Error Analysis for the Physical Sciences* (McGraw-Hill, New York, 1969), pp. 135–155.
12. C. R. Giles and E. Desurvire, *J. Lightwave Technol.* **9**, 271 (1991).
13. J. Y. Law, *IEEE Photonics Technol. Lett.* **9**, 437 (1997).
14. D. Gloge, *Appl. Opt.* **10**, 2252 (1971).
15. C. R. Pollock, *Fundamentals of Optoelectronics* (Irwin, Chicago, 1995).
16. H. Yoda *et al.*, *J. Lightwave Technol.* **24**, 1350 (2006).
17. J. R. Marciante and J. D. Zuegel, *Appl. Opt.* **45**, 6798 (2006).
18. Hardy, *J. Lightwave Technol.* **16**, 1865 (1998).

---

## Time-Dependent Nuclear Measurements of Mix in Inertial Confinement Fusion

Ignition and high gain in inertial confinement fusion (ICF)<sup>1,2</sup> are critically dependent on mitigation of the Rayleigh–Taylor (RT) instability. ICF capsules typically consist of a spherical shell filled with a gaseous fuel and are imploded using lasers (direct drive) or x rays (indirect drive) to rapidly deposit energy and ablate the capsule surface. The RT instability, which is the growth of nonuniformities at a density interface when a low-density material accelerates a high-density material, occurs during two distinct intervals in ICF implosions. During the acceleration phase, the low-density ablating plasma accelerates the solid shell inward, and perturbations seeded by energy deposition nonuniformities or initial capsule surface roughness feed through to the inner fuel–shell surface. During the deceleration phase, shortly before the time of maximum capsule compression, growth of the RT instability at the fuel–shell interface quickly saturates, resulting in small-scale, turbulent eddies that lead to atomic-scale mixing of the fuel and shell.<sup>3</sup> RT growth and the resulting mixing processes disrupt the formation of a hot spot in the fuel, lowering its temperature and reducing its volume, which may prevent the capsule from igniting. Understanding the nature and timing of RT growth and mix under different conditions is an important step toward mitigating their adverse effects.

Substantial and sustained efforts to understand RT instability and mix have been ongoing for many decades.<sup>4</sup> This article presents the first time-dependent nuclear burn measurements of the mix region in ICF implosions. Although it has been previously demonstrated that there is no mix in the burn region at shock bang time,<sup>5,6</sup> it was unknown how long after shock collapse it takes for atomic mixing to occur. Other relevant work on the mix region in ICF implosions includes time-integrated nuclear yield measurements in both direct-drive<sup>6–10</sup> and indirect-drive<sup>11</sup> configurations, as well as time-dependent x-ray measurements of capsules doped with tracer elements.<sup>12</sup> In addition, time-dependent nuclear measurements obtained from implosions of CD-shell capsules filled with nearly pure tritium have recently been reported.<sup>13</sup>

This article reports results from direct-drive experiments conducted with the OMEGA Laser System,<sup>14</sup> with 60 fully smoothed,<sup>15</sup> UV ( $\lambda = 351$  nm) beams in a 1-ns flat-top pulse and a total energy of 23 kJ. The on-target illumination uniformity was typically  $\leq 2\%$  rms. The spherical plastic target capsules had diameters between 860 and 880  $\mu\text{m}$ , a total shell thickness of 20  $\mu\text{m}$ , and a 0.1- $\mu\text{m}$ -rms outer surface roughness. “CH” capsules had plastic (CH) shells and a gaseous fill of deuterium and helium-3 ( $\text{D}_2$  and  ${}^3\text{He}$ , equimolar by atom). “CD” capsules had gaseous fills of pure  ${}^3\text{He}$  and a shell made mostly of CH, except for a 1- $\mu\text{m}$  layer of deuterated plastic (CD) on the inner surface (Fig. 110.62). The fill pressures of the  $\text{D}^3\text{He}$  and the pure  ${}^3\text{He}$  mixtures in CH and CD capsules were chosen to give equal initial fill mass densities  $\rho_0$  at values of 0.5 or 2.5 mg/cm<sup>3</sup>. Because fully ionized D and  ${}^3\text{He}$  have the same value of  $(1+Z)/A$ , mixtures with the same mass density have the same total particle density when fully ionized and can be considered hydrodynamically equivalent.<sup>16</sup>

Implosions of CH and CD capsules were observed using simultaneous measurements of products from two distinct primary nuclear reactions to study the nature and timing of mix. The  $\text{D}-{}^3\text{He}$  reaction,  $\text{D} + {}^3\text{He} \rightarrow {}^4\text{He} + p$ , and the  $\text{DD}-n$  reaction,  $\text{D} + \text{D} \rightarrow {}^3\text{He} + n$ , have dramatically different composition and temperature sensitivities,<sup>16</sup> which are used herein to constrain possible mix scenarios. The  $\text{D}-{}^3\text{He}$  reaction depends much more strongly on temperature due to the doubly charged  ${}^3\text{He}$  reactant, and when the reactant species are initially separated, such as in CD capsules, they must be mixed before nuclear production will occur.<sup>17</sup>

Possible scenarios of atomic mix are constrained using spectral measurements of nascent 14.7-MeV  $\text{D}^3\text{He}$  protons.  $\text{D}^3\text{He}$  protons experience energy loss from their birth energy as they pass through the compressed shell plasma on their way out of the capsule. The proton-emission, path-averaged capsule areal density  $\rho L$  is inferred using the mean-energy downshift of measured proton spectra.<sup>18</sup> For implosions with the same

mean radial areal density  $\rho R$ , the value of  $\rho L$  depends on the spatial distribution of the proton source and shell mass.<sup>18</sup> A larger correction factor is needed as the mean source radius approaches the mean shell radius, as protons traverse longer paths through the shell. For example, a quasi-one-dimensional scenario of atomic mix that consists of a spherical mixing layer just inside a compressed spherical shell will require a much larger correction factor than a three-dimensional scenario involving turbulent mix induced at the tips of RT spikes driven into the hot core.

The dynamics of RT growth are of essential importance for any mix scenario. These dynamics are studied using temporal measurements of the emission of  $D^3He$  protons, obtained using the proton temporal diagnostic (PTD).<sup>19,20</sup> The PTD primarily consists of a 1-mm-thick BC-422 scintillator, an optical transport system, and a fast streak camera. Optical fiducial pulses simultaneously recorded by the streak camera give an absolute timing accuracy of  $\sim 25$  ps. The time history of the proton arrival at the scintillator is obtained by deconvolution of the detector response from the streak camera image.  $D^3He$  proton spectral measurements<sup>18</sup> are then used to infer the  $D^3He$  reaction rate history from the proton current at the scintillator. Additional details on PTD instrumentation and data processing can be found in Frenje *et al.*<sup>19</sup>

Temporal measurements of 2.45-MeV neutrons from the  $DD-n$  nuclear reaction were obtained using the neutron temporal diagnostic (NTD),<sup>21</sup> which works on the same principle as the PTD, but is optimized for neutron detection. Although the  $D-D$  reaction rate in CD capsule implosions is below the noise floor of the NTD, integrated  $D-D$  yields were readily obtained using time-of-flight neutron detectors.<sup>22</sup>

Implosions of CH capsules with  $D^3He$  fuel characteristically emit  $D^3He$  protons at two distinct times (Fig. 110.62). The shock burn is induced by the collapse of an ingoing spherical shock and occurs before the imploding shell starts to decelerate. About 250 ps later, during the deceleration phase, the compression burn occurs as the imploding capsule compresses and reheats the fuel. In contrast to the two stages of proton emission observed in CH capsule implosions with  $D^3He$  fills, CD capsules emit protons only during the later phase (Fig. 110.62), confirming the hypothesis that there is no mix at the time of shock collapse,<sup>23</sup> first presented by Petrasso *et al.*<sup>5</sup>

Measurements of time-integrated nuclear yields demonstrate that capsules with lower  $\rho_0$  have an increased susceptibility to mix.<sup>6,9</sup> Yields increased with lower  $\rho_0$  for CD capsule implosions, even though low  $\rho_0$  is less favorable for nuclear production in the capsule core, as seen through the decrease

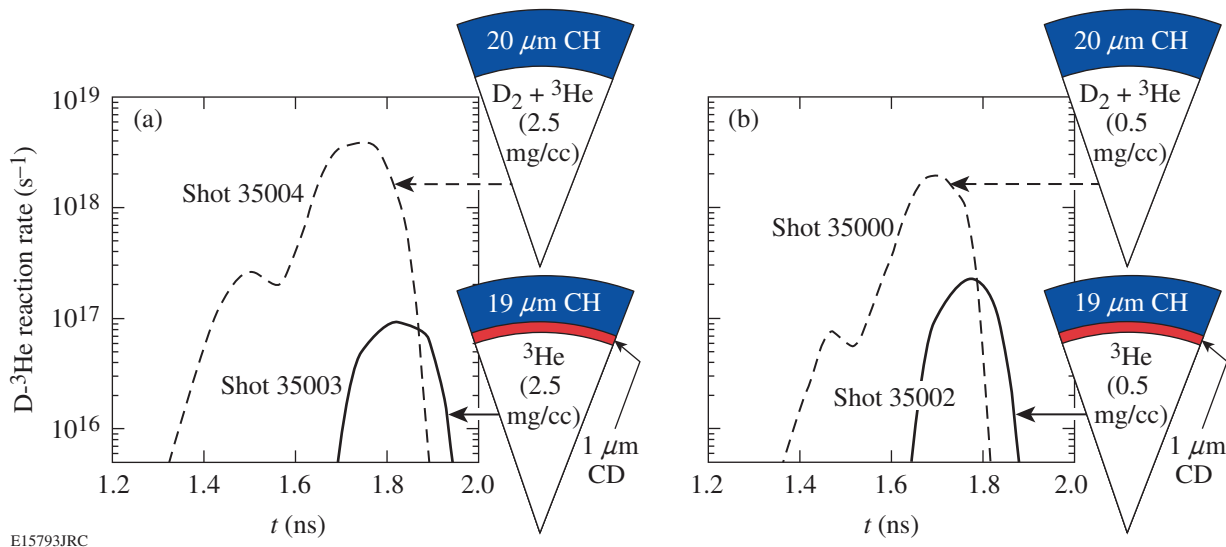


Figure 110.62

Measurements of the  $D^3He$  nuclear reaction history from implosions of spherical plastic (CH) shells filled with an equimolar  $D_2^3He$  mixture, and of equivalent CD-layer capsules filled with pure  $^3He$ . The gaseous fuel was filled to initial densities of (a)  $2.5 \text{ mg/cm}^3$  and (b)  $0.5 \text{ mg/cm}^3$ . The CH capsule histories show distinct times of  $D^3He$  nuclear production corresponding to the shock (at  $\sim 1.5$  ns) and compression ( $\sim 1.75$  ns) burns. CD capsule implosions require mixing of the fuel and shell on the atomic scale for  $D^3He$  production, and the histories show that no such mix has occurred at shock-bang time. The time necessary for hydro-instabilities to induce fuel-shell mix results in a typical  $75 \pm 30$ -ps delay in the peak  $D^3He$  reaction rate in CD capsules compared to equivalent CH capsules. In addition, nuclear production in CD implosions continues even after the compression burn ends in CH capsules, staying well above the typical noise level of  $3 \times 10^{15}/s$  for an additional 50 ps.

in yields for CH capsules (see Fig. 110.62 and Table 110.X). The increase in yields for lower  $\rho_0$  cannot be attributed to a difference in the temperature profile because both DD- $n$  and D- $^3\text{He}$  yields increased by about the same factor of 1.8, despite markedly different composition and temperature dependence. Additional mix of  $^3\text{He}$  with the CD shell in low- $\rho_0$  implosions must be invoked to explain the yield trends.<sup>24</sup>

The time necessary for RT growth to induce turbulent, atomic-scale mixing of the fuel and shell results in a delay in the bang time (defined as the time of peak D- $^3\text{He}$  reaction rate) of CD capsules compared to equivalent CH capsules of  $83 \pm 37$  ps and  $69 \pm 21$  ps for high and low  $\rho_0$  (Fig. 110.63 and Table 110.X), respectively; this is equal to about half the typical 150-ps burn duration (defined as the full temporal width above half peak reaction rate). The delay is calculated as the difference between the ensemble averages of CD and CH capsule bang times, and the error is calculated as the quadrature sum of the standard errors of the mean for each ensemble average.

Measurements of DD- $n$  bang time in CH capsules closely match the observed D- $^3\text{He}$  bang time (Fig. 110.63); however, the D-D reaction rate in CD capsules was too low for robust timing measurements.

The observed bang-time delay is not an artifact of limitations of the diagnostics or experimental setup. The timing jitter of the PTD is the same for CH and CD implosions and is less than 20 ps, while bang-time errors of only 10 ps are introduced in the deconvolution process by proton energy spectrum uncertainties. A small systematic difference in shell thickness between CH and CD capsules was corrected using a 13-ps adjustment to the bang-time delay,<sup>25</sup> and it has been demonstrated that bang time does not depend on potential differences in implosion dynamics between capsules with pure  $^3\text{He}$  fuel and capsules with D $_2$ - $^3\text{He}$  mixtures.<sup>16</sup>

The observed delay of the peak reaction rate for CD capsules is likely due to the difference in how mix affects nuclear production in CH and CD capsules. Whereas mix tends to quench nuclear production in CH capsules through dilution and cooling of the hot fuel, in CD capsules mix enhances nuclear production by the addition and heating of the D reactant from the shell. Nuclear production in CD capsules does not occur until later in the deceleration phase, when the growth of the RT instability has had time to induce turbulent mixing. Enhancement of reactant densities in CD capsules by continued mix in the later stages of compression, combined with the larger total

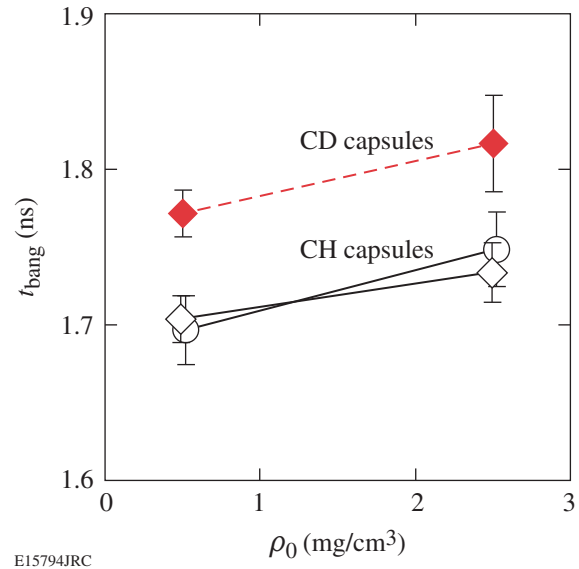


Figure 110.63

Mean and standard error of D $^3\text{He}$  (diamonds) and DD- $n$  (circles) compression-bang times from CH (open markers) and CD (solid markers) capsule implosions as a function of initial fill density. In CD capsules, D $^3\text{He}$  bang time consistently occurs  $\sim 75$  ps later than in CH capsules.

Table 110.X: The number of shots in different ensembles of implosions of D $^3\text{He}$ -filled CH capsules and  $^3\text{He}$ -filled CD capsules with two values of initial fill density  $\rho_0$  is shown, along with ensemble averages and standard errors of the mean for several experimental observables: bang time and burn duration for DD- $n$  and D- $^3\text{He}$  nuclear reaction histories, time-integrated DD- $n$  and D- $^3\text{He}$  yields ( $Y_n$  and  $Y_p$ ), and areal density  $\rho L$ . Standard errors are quoted in the same units as the averages, except for the yields, which are expressed as a percent. Only the compression component is included for  $Y_p$  and  $\rho L$  in CH capsules.

Type	$\rho_0$ (mg/cm $^3$ )	$N$ shots	DD bang (ps)	DD burn (ps)	D $^3\text{He}$ bang (ps)	D $^3\text{He}$ burn (ps)	$Y_n$ ( $\times 10^8$ )	Err (%)	$Y_p$ ( $\times 10^7$ )	Err (%)	$\rho L$ (mg/cm $^2$ )
CH	2.5	8	1749 $\pm$ 24	157 $\pm$ 10	1734 $\pm$ 19	155 $\pm$ 11	129	6	61	10	54 $\pm$ 2
CH	0.5	8	1697 $\pm$ 22	148 $\pm$ 11	1704 $\pm$ 15	123 $\pm$ 12	29	9	30	16	61 $\pm$ 2
CD	2.5	7	—	—	1817 $\pm$ 31	154 $\pm$ 15	5.1	9	1.7	11	64 $\pm$ 4
CD	0.5	5	—	—	1772 $\pm$ 15	153 $\pm$ 13	9.4	7	3.0	13	66 $\pm$ 4

mass of fuel in such capsules, is enough to prolong nuclear production even after production would have been quenched in a CH implosion (Fig. 110.62).

Furthermore, systematically later nuclear production in CD capsule implosions leads to higher expected  $\rho L$ . The mean radial areal density  $\rho R$  increases throughout the deceleration phase as the shell continues to compress, so protons will selectively sample higher  $\rho R$  (and  $\rho L$ ) if they are emitted later in time. This effect is in addition to the potentially higher  $\rho L$  for CD capsules from geometric effects due to a noncentralized proton source profile, described above.

As seen in Fig. 110.64 and Table 110.X,  $\rho L$  is 9% and 18% higher for implosions of CD capsules than for equivalent CH capsules with low and high  $\rho_0$ , respectively.<sup>26</sup> These values are not much higher, suggesting that one or both of the effects described above might not be as significant as expected. On this basis we conjecture that the source of protons in CD capsules may be dominated by atomic mixing at the tips of RT

spikes from the shell that drive into the hot core, which would result in a more central proton emission profile and a smaller increase in  $\rho L$ .

In summary, temporal measurements of  $D^3He$  protons emitted from ICF implosions of CD-shell,  $^3He$ -filled capsules offer new and valuable insights into the dynamics of turbulent mixing induced by saturation of the Rayleigh–Taylor instability. The first such measurements have demonstrated that bang time is substantially delayed as RT growth saturates to produce mix. The  $83 \pm 37$ -ps bang-time delay of CD implosions compared to  $D^3He$ -filled, CH implosions for high initial fill densities ( $\rho_0$ ) is equal to half the burn duration. Reducing  $\rho_0$  by a factor of 5 increases the susceptibility of the implosion to mix and does not significantly affect the bang-time delay, observed to be  $69 \pm 21$  ps. Continued mixing of the fill gas and shell prolongs nuclear production in CD capsules even after it is quenched in equivalent CH capsules. Finally, the relatively small increase in areal density  $\rho L$  of CD compared to CH capsules, despite the later bang time, suggests that nuclear production is dominated by mixing induced at the tips of RT spikes driven into the hot core.

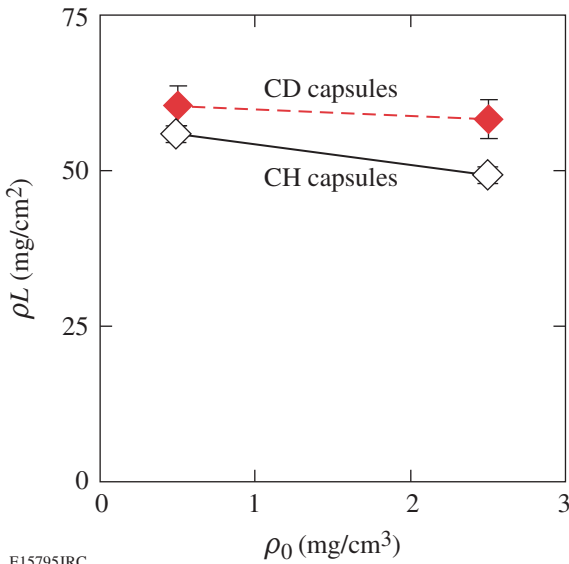


Figure 110.64 Mean and standard error of proton-emission-path-averaged areal densities ( $\rho L$ ) for CH (open markers) and CD (solid markers) implosions as a function of initial fill density.  $D^3He$  proton spectral measurements are used to infer this compression-burn averaged  $\rho L$ , where the shock component of CH implosion spectra has been excluded. For CH capsules, the radial areal density ( $\rho R$ ) can be obtained from  $\rho L$  using a small correction ( $\rho R \sim 0.93 \rho L$ ), which depends on the shell aspect ratio. The relation between  $\rho R$  and  $\rho L$  for CD capsules sensitively depends on the source profile as the mean source radius approaches the mean shell radius; that  $\rho L$  is not much higher than in CH capsules suggests that the source profile is still centrally peaked.

ACKNOWLEDGMENT

The authors express their gratitude to the OMEGA engineers and operations crew who supported these experiments. This work was supported in part by the U.S. Department of Energy Office of Inertial Confinement Fusion (Grant No. DE-FG03-03NA00058), by the Lawrence Livermore National Laboratory (Subcontract No. B543881), by the Fusion Science Center for Extreme States of Matter and Fast Ignition (Contract No. 412761-G), and by the Laboratory for Laser Energetics (Subcontract No. 412160-001G) under Cooperative Agreement DE-FC52-92SF19460, University of Rochester, and New York State Energy Research and Development Authority.

REFERENCES

1. J. Nuckolls *et al.*, *Nature* **239**, 139 (1972).
2. S. Atzeni and J. Meyer-ter-Vehn, *The Physics of Inertial Fusion: Beam Plasma Interaction, Hydrodynamics, Hot Dense Matter*, International Series of Monographs on Physics (Clarendon Press, Oxford, 2004).
3. P. E. Dimotakis, *Annu. Rev. Fluid Mech.* **37**, 329 (2005).
4. See, for example, Sec. 8.9 of Ref. 2 for a review of the literature.
5. R. D. Petrasso, J. A. Frenje, C. K. Li, F. H. Séguin, J. R. Rygg, B. E. Schwartz, S. Kurebayashi, P. B. Radha, C. Stoeckl, J. M. Soares, J. Delettrez, V. Yu. Glebov, D. D. Meyerhofer, and T. C. Sangster, *Phys. Rev. Lett.* **90**, 095002 (2003).
6. J. R. Rygg, J. A. Frenje, C. K. Li, F. H. Séguin, R. D. Petrasso, J. A. Delettrez, V. Yu. Glebov, V. N. Goncharov, D. D. Meyerhofer, P. B. Radha, S. P. Regan, and T. C. Sangster, *Phys. Plasmas* **14**, 056306 (2007).

7. D. D. Meyerhofer, J. A. Delettrez, R. Epstein, V. Yu. Glebov, V. N. Goncharov, R. L. Keck, R. L. McCrory, P. W. McKenty, F. J. Marshall, P. B. Radha, S. P. Regan, S. Roberts, W. Seka, S. Skupsky, V. A. Smalyuk, C. Sorce, C. Stoeckl, J. M. Soures, R. P. J. Town, B. Yaakobi, J. D. Zuegel, J. Frenje, C. K. Li, R. D. Petrasso, D. G. Hicks, F. H. Séguin, K. Fletcher, S. Padalino, C. Freeman, N. Izumi, R. Lerche, T. W. Phillips, and T. C. Sangster, *Phys. Plasmas* **8**, 2251 (2001).
8. P. B. Radha, J. Delettrez, R. Epstein, V. Yu. Glebov, R. Keck, R. L. McCrory, P. McKenty, D. D. Meyerhofer, F. Marshall, S. P. Regan, S. Roberts, T. C. Sangster, W. Seka, S. Skupsky, V. Smalyuk, C. Sorce, C. Stoeckl, J. Soures, R. P. J. Town, B. Yaakobi, J. Frenje, C. K. Li, R. Petrasso, F. Séguin, K. Fletcher, S. Padalino, C. Freeman, N. Izumi, R. Lerche, and T. W. Phillips, *Phys. Plasmas* **9**, 2208 (2002).
9. C. K. Li, F. H. Séguin, J. A. Frenje, S. Kurebayashi, R. D. Petrasso, D. D. Meyerhofer, J. M. Soures, J. A. Delettrez, V. Yu. Glebov, P. B. Radha, F. J. Marshall, S. P. Regan, S. Roberts, T. C. Sangster, and C. Stoeckl, *Phys. Rev. Lett.* **89**, 165002 (2002).
10. D. C. Wilson, C. W. Cranfill, C. Christensen, R. A. Forster, R. R. Peterson, H. M. Hoffman, G. D. Pollak, C. K. Li, F. H. Séguin, J. A. Frenje, R. D. Petrasso, P. W. McKenty, F. J. Marshall, V. Yu. Glebov, C. Stoeckl, G. J. Schmid, N. Izumi, and P. Amendt, *Phys. Plasmas* **11**, 2723 (2004).
11. R. E. Chrien *et al.*, *Phys. Plasmas* **5**, 768 (1998).
12. S. P. Regan, J. A. Delettrez, F. J. Marshall, J. M. Soures, V. A. Smalyuk, B. Yaakobi, V. Yu. Glebov, P. A. Jaanimagi, D. D. Meyerhofer, P. B. Radha, W. Seka, S. Skupsky, C. Stoeckl, R. P. J. Town, D. A. Haynes, Jr., I. E. Golovkin, C. F. Hooper, Jr., J. A. Frenje, C. K. Li, R. D. Petrasso, and F. H. Séguin, *Phys. Rev. Lett.* **89**, 085003 (2002).
13. D. C. Wilson, P. S. Ebey, A. Nobile, Jr., J. H. Cooley, T. C. Sangster, W. T. Shmayda, M. J. Bonino, D. Harding, V. Yu. Glebov, F. J. Marshall, and R. A. Lerche, *Bull. Am. Phys. Soc.* **51**, 295 (2006).
14. T. R. Boehly, D. L. Brown, R. S. Craxton, R. L. Keck, J. P. Knauer, J. H. Kelly, T. J. Kessler, S. A. Kumpan, S. J. Loucks, S. A. Letzring, F. J. Marshall, R. L. McCrory, S. F. B. Morse, W. Seka, J. M. Soures, and C. P. Verdon, *Opt. Commun.* **133**, 495 (1997).
15. S. Skupsky and R. S. Craxton, *Phys. Plasmas* **6**, 2157 (1999).
16. J. R. Rygg, J. A. Frenje, C. K. Li, F. H. Séguin, R. D. Petrasso, J. A. Delettrez, V. Yu. Glebov, V. N. Goncharov, D. D. Meyerhofer, S. P. Regan, T. C. Sangster, and C. Stoeckl, *Phys. Plasmas* **13**, 052702 (2006).
17. Non-atomic mix scenarios fail to produce significant yield since thermal  $^3\text{He}$  ions cannot penetrate far enough into the CD layer. For example, to give  $\text{D}^3\text{He}$  yields comparable to those observed, it can be shown that all  $^3\text{He}$  ions in the fuel ( $\sim 2 \times 10^{17}$ ) would have to be launched into the CD layer at energies of 50 keV, grossly higher than the typical fuel ion temperature of 4 keV.
18. F. H. Séguin, J. A. Frenje, C. K. Li, D. G. Hicks, S. Kurebayashi, J. R. Rygg, B.-E. Schwartz, R. D. Petrasso, S. Roberts, J. M. Soures, D. D. Meyerhofer, T. C. Sangster, J. P. Knauer, C. Sorce, V. Yu. Glebov, C. Stoeckl, T. W. Phillips, R. J. Leeper, K. Fletcher, and S. Padalino, *Rev. Sci. Instrum.* **74**, 975 (2003).
19. *LLE Review Quarterly Report* **96**, 230, Laboratory for Laser Energetics, University of Rochester, Rochester, NY, LLE Document No. DOE/SF/19460-509, NTIS Order No. PB2006-106668 (2003).
20. J. A. Frenje, C. K. Li, F. H. Séguin, J. Deciantis, S. Kurebayashi, J. R. Rygg, R. D. Petrasso, J. Delettrez, V. Yu. Glebov, C. Stoeckl, F. J. Marshall, D. D. Meyerhofer, T. C. Sangster, V. A. Smalyuk, and J. M. Soures, *Phys. Plasmas* **11**, 2798 (2003).
21. R. A. Lerche, D. W. Phillion, and G. L. Tietbohl, *Rev. Sci. Instrum.* **66**, 933 (1995).
22. R. A. Lerche and T. J. Murphy, *Rev. Sci. Instrum.* **63**, 4880 (1992).
23. Or that such mix, if present, has been insufficiently heated to give nuclear production.
24. For example, if it is assumed that the  $\text{DD-}n$  yield increase is due only to an increase in the temperature of the mix region, then the fraction of  $^3\text{He}$  fuel contained in the mix region must be three times greater for low  $\rho_0$  to produce the observed  $\text{D-}^3\text{He}$  yield increase.
25. The 13-ps reduction in the delay corrects for a  $1/3\text{-}\mu\text{m}$  systematic difference in the total thickness of the CH and CD shells, where the timing of each burn history was adjusted by  $(40 \text{ ps}) \times (20 \Delta)$ , where  $\Delta$  is the capsule thickness in  $\mu\text{m}$ . The 40-ps/ $\mu\text{m}$  correction factor was obtained by a linear fit of CH capsule bang times over a range of thicknesses from 15 to 27  $\mu\text{m}$ .
26. The slightly higher ( $<2\%$ ) initial shell mass in CD capsules due to the high density of the  $1\text{-}\mu\text{m}$ -thick CD layer and the systematic thickness difference has a minimal impact on  $\rho L$  ( $<1\%$ ).

---

## Publications and Conference Presentations

---

### Publications

---

- B. Ashe, K. L. Marshall, C. Giacomini, A. L. Rigatti, T. J. Kessler, A. W. Schmid, J. B. Oliver, J. Keck, and A. Kozlov, "Evaluation of Cleaning Methods for Multilayer Diffraction Gratings," in *Laser-Induced Damage in Optical Materials: 2006*, edited by G. J. Exarhos, A. H. Guenther, K. L. Lewis, D. Ristau, M. J. Soileau, and C. J. Stolz (SPIE, Bellingham, WA, 2007), Vol. 6403, pp. 64030O.
- C. Dorrer, "High-Speed Characterization for Optical Telecommunication Signals," in *Commercial and Biomedical Applications of Ultrafast Lasers VII*, edited by J. Neev, S. Nolte, A. Heisterkamp, and C. B. Schaffer (SPIE, Bellingham, WA, 2007), Vol. 6460, p. 64600L (invited).
- W. Guan and J. R. Marciante, "Dual-Frequency Operation in a Short-Cavity Ytterbium-Doped Laser," *IEEE Photonics Technol. Lett.* **19**, 261 (2007).
- M. Haurylau, S. P. Anderson, K. L. Marshall, and P. M. Fauchet, "Electrically Tunable Silicon 2-D Photonic Bandgap Structures," *IEEE J. Quantum Electron.* **12**, 1527 (2006).
- S. X. Hu, "Producing Ultracold and Trappable Antihydrogen Atoms," *Phys. Rev. Lett.* **75**, 010501(R) (2007).
- S. X. Hu, "Three-Body Recombination of Atomic Ions with Slow Electrons," *Phys. Rev. A* **98**, 133201 (2007).
- T. Z. Kosc, K. L. Marshall, A. Trajkovska-Petkoska, C. J. Coon, K. Hasman, G. V. Babcock, R. Howe, M. Leitch, and S. D. Jacobs, "Development of Polymer Cholesteric Liquid Crystal Flake Technology for Electro-Optic Devices and Particle Displays," in *Emerging Liquid Crystal Technologies II*, edited by L.-C. Chien (SPIE, Bellingham, WA, 2007), Vol. 6487, p. 64870L.
- B. E. Kruschwitz, J. H. Kelly, M. J. Shoup III, L. J. Waxer, E. C. Cost, E. T. Green, Z. M. Hoyt, J. Taniguchi, and T. W. Walker, "High-Contrast Plasma-Electrode Pockels Cell," *Appl. Opt.* **46**, 1326 (2007).
- S. G. Lukishova, A. W. Schmid, R. Knox, P. Freivald, L. J. Bissell, R. W. Boyd, C. R. Stroud, Jr., and K. L. Marshall, "Room Temperature Source of Single Photons of Definite Polarization," *J. Mod. Opt.* **54**, 417 (2007).
- J. A. Marozas, "Fourier Transform-Based Continuous Phase-Plate Design Technique: A High-Pass Phase-Plate Design as an Application for OMEGA and the National Ignition Facility," *J. Opt. Soc. Am. A* **24**, 74 (2007).
- J. E. Miller, T. R. Boehly, A. Melchior, D. D. Meyerhofer, P. M. Celliers, J. H. Eggert, D. H. Hicks, C. M. Sorce, J. A. Oertel, and P. M. Emmel, "A Streaked Optical Pyrometer System for Laser-Driven Shock-Wave Experiments on OMEGA," *Rev. Sci. Instrum.* **78**, 034903 (2007).
- J. Myatt, W. Theobald, J. A. Delettrez, C. Stoeckl, M. Storm, T. C. Sangster, A. V. Maximov, and R. W. Short, "High-Intensity Laser Interactions with Mass-Limited Solid Targets and Implications for Fast-Ignition Experiments on OMEGA EP," *Phys. Plasmas* **14**, 056301 (2007) (invited).
- S. Papernov and A. W. Schmid, "Using Gold Nanoparticles as Artificial Defects in Thin Films: What Have We Learned About Laser-Induced Damage Driven by Localized Absorbers?" in *Laser-Induced Damage in Optical Materials: 2006*, edited by G. J. Exarhos, A. H. Guenther, K. L. Lewis, D. Ristau, M. J. Soileau, and C. J. Stolz (SPIE, Bellingham, WA, 2007), Vol. 6403, pp. 64030D (invited).
- S. N. Shafrir, J. C. Lambropoulos, and S. D. Jacobs, "A Magnetorheological Polishing-Based Approach for Studying Precision Microground Surfaces of Tungsten Carbides," *Precision Engineering* **31**, 83 (2007).
- W. Słysz, M. Węgrzecki, J. Bar, P. Grabiec, M. Górska, V. Zwiller, C. Latta, P. Böhi, A. J. Pearlman, A. S. Cross, D. Pan, J. Kitaygorsky, I. Komissarov, A. Verevkin, I. Milostnaya, A. Korneev, O. Minayeva, G. Chulkova, K. Smirnov, B. Voronov, G. N. Gol'tsman, and R. Sobolewski,

“Fibre-Coupled, Single Photon Detector Based on NbN Superconducting Nanostructures for Quantum Communications,” *J. Mod. Opt.* **54**, 315 (2007).

V. A. Smalyuk, R. Betti, J. A. Delettrez, V. Yu. Glebov, V. N. Goncharov, D. Y. Li, D. D. Meyerhofer, S. P. Regan, S. Roberts, T. C. Sangster, C. Stoeckl, W. Seka, J. A. Frenje, C. K. Li, R. D. Petrasso, and F. H. Séguin, “Experimental Studies of Direct-Drive, Low-Intensity, Low-Adiabatic Spherical Implosions on OMEGA,” *Phys. Plasmas* **14**, 022702 (2007).

V. A. Smalyuk, V. N. Goncharov, K. S. Anderson, R. Betti, R. S. Craxton, J. A. Delettrez, D. D. Meyerhofer, S. P. Regan, and T. C. Sangster, “Measurements of the Effects of the Intensity Pickets on Laser Imprinting for Direct-Drive, Adiabatic-Shaping Designs on OMEGA,” *Phys. Plasmas* **14**, 032702 (2007).

S. Sublett, J. P. Knauer, I. V. Igumenshchev, A. Frank, and D. D. Meyerhofer, “Double-Pulse Laser-Driven Jets on OMEGA,” *Astrophys. Space Sci.* **307**, 47 (2007).

S. Wu, P. Geiser, J. Jun, J. Karpinski, D. Wang, and R. Sobolewski, “Time-Resolved Intervalley Transitions in GaN Single Crystals,” *J. Appl. Phys.* **101**, 043701 (2007).

L. Zheng, A. W. Schmid, and J. C. Lambropoulos, “Surface Effects on Young’s Modulus and Hardness of Fused Silica by Nanoindentation Study,” *J. Mater. Sci.* **42**, 191 (2007).

C. D. Zhou, W. Theobald, R. Betti, P. B. Radha, V. A. Smalyuk, D. Shvarts, V. Yu. Glebov, C. Stoeckl, K. S. Anderson, D. D. Meyerhofer, T. C. Sangster, C. K. Li, R. D. Petrasso, J. A. Frenje, and F. H. Séguin, “High- $\rho R$  Implosions for Fast-Ignition Fuel Assembly,” *Phys. Rev. Lett.* **98**, 025004 (2007).

---

### Forthcoming Publications

---

V. Bagnoud, J. D. Zuegel, N. Forget, and C. Le Blanc, “High-Dynamic-Range Temporal Measurements of Short Pulses Amplified by OPCPA,” to be published in *Optics Express*.

R. Betti, C. D. Zhou, K. S. Anderson, L. J. Perkins, W. Theobald, and A. A. Solodov, “Shock Ignition of Thermonuclear Fuel with High Areal Density,” to be published in *Physical Review Letters*.

P. Brijesh, T. J. Kessler, J. D. Zuegel, and D. D. Meyerhofer, “Demonstration of a Horseshoe-Shaped Longitudinal Focal Profile,” to be published in the *Journal of the Optical Society of America B*.

T. J. B. Collins, J. A. Marozas, R. Betti, D. R. Harding, P. W. McKenty, P. B. Radha, S. Skupsky, V. N. Goncharov, J. P. Knauer, and R. L. McCrory, “One-Megajoule, Wetted-Foam Target Design Performance for the NIF,” to be published in *Physics of Plasmas* (invited).

C. Dorrer and J. D. Zuegel, “Design and Analysis of Binary Shapers Using the Error-Diffusion Algorithm,” to be published in the *Journal of the Optical Society of America B*.

C. Dorrer and J. D. Zuegel, “Optical Testing Using the Transport-of-Intensity Equation,” to be published in *Optics Express*.

D. H. Edgell, R. S. Craxton, L. M. Elasky, D. R. Harding, S. J. Verbridge, M. D. Wittman, and W. Seka, “Three-Dimensional Characterization of Cryogenic Targets Using Systems Identification Techniques with Multiple Shadowgraph Views,” to be published in *Fusion Science and Technology*.

K. A. Fletcher, B. Apker, S. Hammond, J. Punaro, F. J. Marshall, J. Laine, and R. Forties, “Detection of Charged Particles with Charge Injection Devices,” to be published in *Review of Scientific Instruments*.

G. N. Gol’tsman, O. Minaeva, A. Korneev, M. Tarkhov, I. Rubstova, A. Divochiy, I. Milostnaya, G. Chulkova, N. Kaurova, B. Voronov, D. Pan, J. Kitaygorsky, A. Cross, A. Pearlman, I. Komissarov, W. Słysz, M. Węgrzecki, P. Grabiec, and R. Sobolewski, “Middle-Infrared to Visible-Light Ultrafast Superconducting Single-Photon Detectors,” to be published in *IEEE Transactions on Applied Superconductivity*.

V. N. Goncharov, “Ablative Richtmyer–Meshkov Instability: Theory and Experimental Results,” to be published in the *Proceedings of Scottish Summer School*.

V. N. Goncharov, “Direct-Drive Inertial Fusion: Basic Concepts and Ignition Target Designing,” to be published in the *Proceedings of Scottish Summer School*.

W. Guan and J. R. Marciante, "Single-Polarization, Single-Frequency, 2-cm Ytterbium-Doped Fiber Laser," to be published in *Electronics Letters*.

S. D. Jacobs, "Manipulating Mechanics and Chemistry in Precision Optics Finishing," to be published in *Science and Technology of Advanced Materials*.

M. Khafizov, X. Li, R. Sobolewski, Y. Cui, and X. X. Xi, "Mechanisms of Light Detection by Superconducting Current-Biased MgB<sub>2</sub> Microbridges," to be published in *IEEE Transactions on Applied Superconductivity*.

J. Kitaygorsky, I. Komissarov, A. Jukna, D. Pan, O. Minaeva, N. Kaurova, A. Divochiy, A. Korneev, M. Tarkhov, B. Voronov, I. Milostnaya, G. Gol'tsman, and R. Sobolewski, "Dark Counts in Nanostructured NbN Superconducting Single-Photon Detectors and Bridges," to be published in *IEEE Transactions on Applied Superconductivity*.

X. Li, M. Khafizov, Š. Chromik, M. Valerianova, V. Štrbík, P. Odier, and R. Sobolewski, "Ultrafast Photoresponse Dynamics of Current-Biased Hg-Ba-Ca-Cu-O Superconducting Microbridges," to be published in *IEEE Transactions on Applied Superconductivity*.

J. R. Marciante, W. R. Donaldson, and R. G. Roides, "Averaging of Replicated Pulses for Enhanced Dynamic Range, Single-Shot Measurement of Nanosecond Optical Pulses," to be published in *IEEE Photonics Technology Letters*.

R. L. McCrory, "Highlights of the History of the University of Rochester," to be published in *Inertial Confinement Nuclear Fusion: A Historical Approach by Its Pioneers*.

S. P. Regan, R. Epstein, V. N. Goncharov, I. V. Igumenshchev, D. Li, P. B. Radha, H. Sawada, T. R. Boehly, J. A. Delettrez, O. V. Gotchev, J. P. Knauer, J. A. Marozas, F. J. Marshall,

R. L. McCrory, P. W. McKenty, D. D. Meyerhofer, T. C. Sangster, S. Skupsky, V. A. Smalyuk, B. Yaakobi, and R. Mancini, "Laser-Energy Coupling, Mass Ablation Rate, and Shock Heating in Direct-Drive Inertial Confinement Fusion," to be published in *Physics of Plasmas* (invited).

T. C. Sangster, R. Betti, R. S. Craxton, J. A. Delettrez, D. H. Edgell, L. M. Elasky, V. Yu. Glebov, V. N. Goncharov, D. R. Harding, D. Jacobs-Perkins, R. Janezic, R. L. Keck, J. P. Knauer, S. J. Loucks, L. D. Lund, F. J. Marshall, R. L. McCrory, P. W. McKenty, D. D. Meyerhofer, P. B. Radha, S. P. Regan, W. Seka, W. T. Shmayda, S. Skupsky, V. A. Smalyuk, J. M. Soures, C. Stoeckl, B. Yaakobi, J. A. Frenje, C. K. Li, R. D. Petrasso, F. H. Séguin, J. D. Moody, J. A. Atherton, B. D. MacGowan, J. D. Kilkenny, T. P. Bernat, and D. S. Montgomery, "Cryogenic DT and D<sub>2</sub> Targets for Inertial Confinement Fusion," to be published in *Physics of Plasmas* (invited tutorial).

S. N. Shafirir, J. C. Lambropoulos, and S. D. Jacobs, "Subsurface Damage (SSD) in Estimation in Precision Microground Hard Ceramics," to be published in *Applied Optics*.

S. N. Shafirir, J. C. Lambropoulos, and S. D. Jacobs, "Technical Note: Toward Magnetorheological Finishing of Magnetic Materials," to be published in the *Journal of Manufacturing Science and Engineering*.

A. A. Solodov, R. Betti, J. A. Delettrez, and C. D. Zhou, "Gain Curves and Hydrodynamic Simulations of Ignition and Burn for Direct-Drive Fast-Ignition Fusion Targets," to be published in *Physics of Plasmas*.

T. Taneda, G. Pepe, L. Parlato, A. A. Golubov, and R. Sobolewski, "Time-Resolved Carrier Dynamics and Electron-Phonon Coupling Strength in Proximized Weak Ferromagnet/Superconductor Nanobilayers," to be published in *Physical Review B*.

---

## Conferences Presentations

---

The following presentations were made at SPIE Photonics West, San Jose, CA, 20–25 January 2007:

C. Dorrer, "High-Speed Characterization for Optical Telecommunication Signals" (invited).

T. Z. Kosc, K. L. Marshall, A. Trajkovska-Petkoska, C. J. Coon, K. Hasman, G. V. Babcock, R. Howe, M. Leitch, and S. D. Jacobs, "Development of Polymer Cholesteric Liquid Crystal Flake Technology for Electro-Optic Devices and Particle Displays" (invited).

The following presentations were made at ASSP 2007, Vancouver, Canada, 28–31 January 2007:

I. A. Begishev, V. Bagnoud, C. Dorrer, and J. D. Zuegel, “Suppression of Optical Parametric Generation in the High-Efficient OPCPA System.”

Z. Jiang and J. R. Marciante, “Impact of Spatial-Hole Burning on Beam Quality in Large-Mode-Area Fibers.”

J. R. Marciante, “Effectiveness of Radial Gain Tailoring in Large-Mode-Area Fiber Lasers and Amplifiers.”

A. V. Okishev and J. D. Zuegel, “Intracavity-Pumped Raman Laser Action in a Mid-IR CW MgO:PPLN Optical Parametric Oscillator.”

---

J. M. Soures and D. D. Meyerhofer, “High-Energy-Density Physics Research at NLUF with the OMEGA and OMEGA EP Lasers,” 2007 Stewardship Science Academic Alliance Program Symposium, Washington, DC, 5–7 February 2007.

---

R. L. McCrory, D. D. Meyerhofer, S. J. Loucks, S. Skupsky, K. S. Anderson, R. Betti, T. R. Boehly, M. J. Bonino, R. S. Craxton, T. J. B. Collins, J. A. Delettrez, D. H. Edgell, R. Epstein, V. Yu. Glebov, V. N. Goncharov, D. R. Harding, R. L. Keck, J. H. Kelly, T. J. Kessler, J. P. Knauer, L. D. Lund, D. Jacobs-Perkins, J. R. Marciante, J. A. Marozas, F. J. Marshall, A. V. Maximov, P. W. McKenty, S. F. B. Morse, J. Myatt, S. G. Noyes, P. B. Radha, T. C. Sangster, W. Seka, V. A. Smalyuk, J. M. Soures, C. Stoeckl, W. Theobald, K. A. Thorp, M. D. Wittman, B. Yaakobi, C. D. Zhou, J. D. Zuegel, C. K. Li, R. D. Petrasso, J. A. Frenje, and F. H. Séguin, “Inertial Confinement Fusion Research at the Laboratory for Laser Energetics,” 7th Symposium on Current Trends in International Fusion Research: A Review, Washington, DC, 5–9 March 2007.

---

J. R. Marciante, “Fiber Technologies for Terawatt Lasers,” Optical Fiber Communication Conference 2007, Anaheim, CA, 25–29 March 2007.

UNIVERSITY OF  
**ROCHESTER**